UW-Madison.
SSEC Publication No.92.09.S1.

Space Science and Engineering Center
University of Wisconsin–Madison

Madison, WI 53706

A REPORT OF THE SEVERE WEATHER PROGRAM FOR THE PERIOD 1 SEPTEMBER 1990 TO 29 FEBRUARY 1992

A REPORT from the

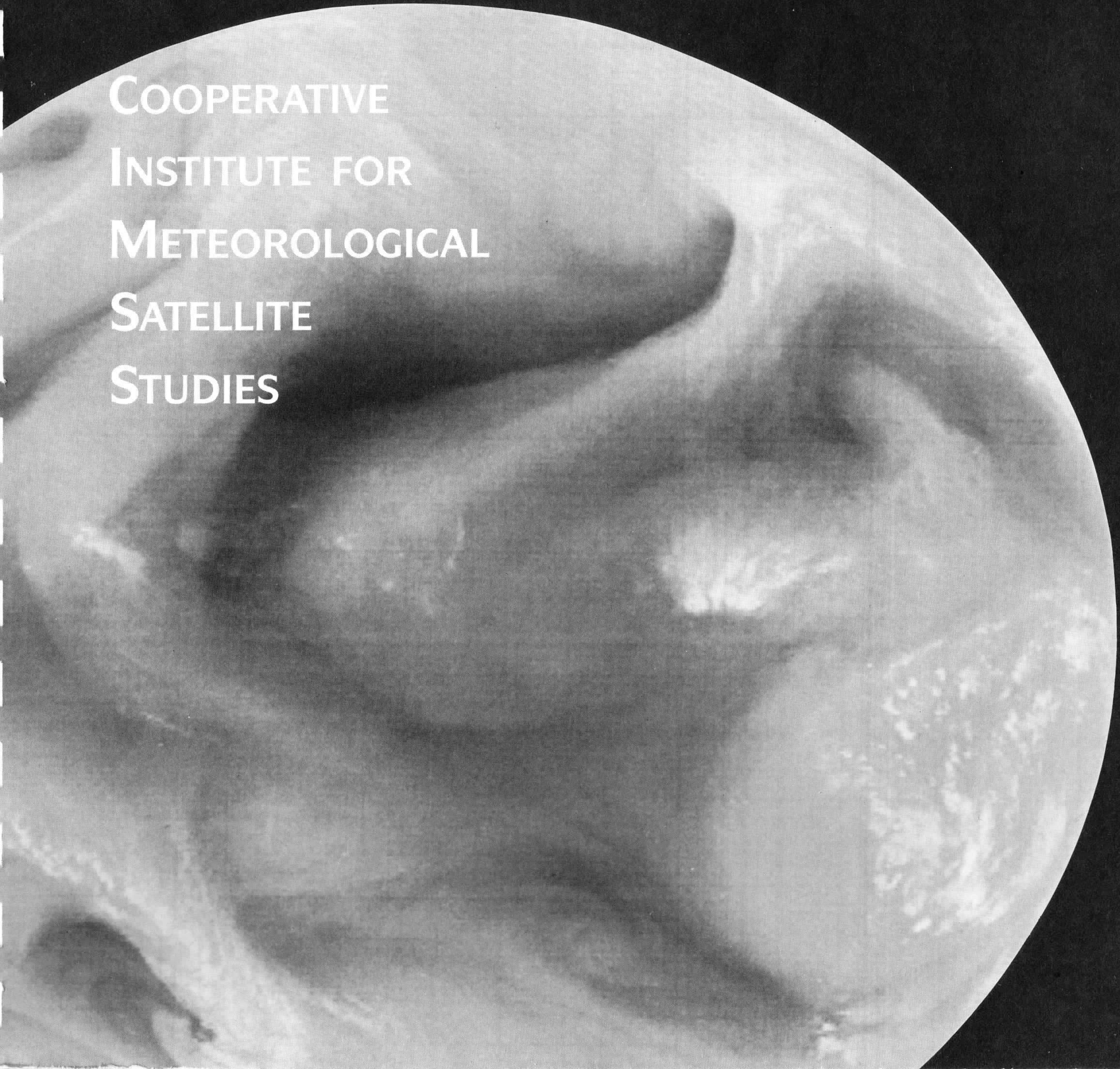

COOPERATIVE INSTITUTE FOR METEOROLOGICAL SATELLITE STUDIES

THE SCHWERDTFEGER LIBRARY
1225 W. Dayton Street
Madison, WI 53706

A REPORT
OF THE
SEVERE WEATHER PROGRAM
FOR THE PERIOD
1 SEPTEMBER 1990 TO 29 FEBRUARY 1992

Submitted by

Cooperative Institute for Meteorological Satellite Studies
Space Science and Engineering Center (SSEC)
at the University of Wisconsin-Madison
1225 West Dayton Street
Madison, Wisconsin 53706
(608)263-7435

William L. Smith
Director, CIMSS
Principal Investigator

Anthony T. Schreiner
Associate Researcher
Program Manager

Christopher M. Hayden
Chief, SDAB
Principal Scientist

A REPORT
OF THE
SEVERE WEATHER PROGRAM
FOR THE PERIOD
1 SEPTEMBER 1990 TO 29 FEBRUARY 1992

A REPORT
OF THE
SEVERE WEATHER PROGRAM
FOR THE PERIOD
1 SEPTEMBER 1990 TO 29 FEBRUARY 1992

I. INTRODUCTION

This report summarizes the work done during year two of a three year program funded by the National Environmental Satellite Data and Information Service (NESDIS). The period was initially to cover from 1 September 1990 through 31 August 1991, but was given a "no cost extension" to 29 February 1992 in order to finish several projects which were not completed within the original contract period. The purpose of this report is to describe in some detail the scientific results and accomplishments which were realized during this contract period. This report is divided into five major sections. Section II discusses the results of projects completed under this grant. Each topic is treated as an extended abstract outlining the major conclusions for each area of concentration, authored by the scientist(s) who was (were) mainly responsible for the work. Section III briefly summarizes the personnel funded by this project and equipment which was acquired. Section IV is a summary, which is followed by a reference section (V) which lists all the references included in the abstract plus articles resulting from the research work described. The main areas of research covered in this report are:

- The Gulf of Mexico Experiment (GUFMEX): Three areas of research have either been totally or partially funded under this contract.
- Data assimilation: The assimilation of satellite data in numerical forecast models has received a large emphasis through graduate student work, computer modeling, and hardware acquisition within the framework of this contract.
- Satellite-derived motion vectors: The work performed under this grant concentrated on computer software required to automate and improve the quality of satellite-derived motion vectors.
- Polar orbiting products: Generation of high resolution satellite motion vectors over the polar regions which utilize the NOAA Advanced Very High Resolution Radiometer (AVHRR) has been funded by this project.
- Research and testing of a ground based remote sensing system: During the winter STORM-FEST field experiment in February and early March of 1992 a ground based High resolution Interferometer Sounder (HIS) was operating continuously, generating high temporal resolution temperature and moisture soundings. Funding for this exercise was provided under this grant.

These major topics will be covered in detail in the following section.

II. RESULTS

A. Analysis of a western Gulf of Mexico cool season return flow. Contributed by Robert T. Merrill

Most studies of the synoptic meteorology of the southern Great Plains concern processes which establish the environment for severe convective storms. Foremost is the process of "differential advection", in which a westerly or southwesterly stream of continental air overlays a southerly stream of moist maritime air. The development of conditional instability depends upon the thermodynamic properties of the two streams, and hence their histories.

In the cool season, the moist stream often consists of "return flow," extensively modified polar air which flowed over the Gulf of Mexico behind the previous disturbance. If the southerly flow persists or the previous polar outbreak did not penetrate too far into the Gulf, tropical air from the Caribbean Sea may also be included in the moist stream. The thermodynamic properties of the return flow, from whatever source, may be the controlling factor for severe weather occurrence. Return flow events are also often accompanied by low clouds and fog, which pose a hazard to aviation.

The 10-12 March 1988 IOP from the Gulf of Mexico Experiment (GUFMEX, Lewis et. al., 1989) was analyzed to refine the conceptual model of the structure of a moist stream involving return flow and to gain understanding of the physical processes which determine its thermodynamic properties. The data used for this investigation included special 6 hourly rawinsonde, in situ aircraft observations and drop sondes, and ships of opportunity. These results are described in detail in Merrill (1991, 1992) and summarized here. Examples from the 10-12 March 1988 event are then used to illustrate features of the conceptual model.

The planetary boundary layer is believed to approach thermodynamic equilibrium within the duration of the typical cycle of offshore and onshore flow. Equilibrium conditions (mixing ratio w and potential temperature θ) are functions of the sea surface temperature (SST), the surface wind speed, the radiative cooling rate of the PBL, and the subsidence at the top of the PBL. The 10-12 March 1988 surface w analyses were interpreted qualitatively using equilibrium air-sea w and θ differences derived by Betts and Ridgway (1989) for tropical conditions. Based on these equilibrium conditions extended to the Gulf of Mexico in mid-March, "return flow" produced by modification over the Gulf should have a mixing ratio (w) of 8-12 g kg^{-1} (corresponding to a dew point of 10-16^{o} C). This air mass is called "maritime Mid latitude" (mM) to distinguish it from maritime Tropical (mT), which is at equilibrium over the Caribbean Sea or tropical eastern Pacific and has w of 15-18 g kg^{-1} (dew point of 20-22^{o} C).

Figs. 1 and 2 illustrate these air mass differences. Fig. 1 shows the sea level pressure (solid lines) and w (dashed lines) at 00 UT 11 March 1988. Within the post-frontal air are two regions, a large area of relatively dry (and probably still modifying) polar air with *w* of 6-9 g kg^{-1}, and a small area of southerly flow and near-equilibrium conditions (locally 12 g kg^{-1}) in the western Gulf (return flow). The original polar air stream had *w* of 3 g kg^{-1}. Pre-frontal mT air (15 g kg^{-1}) is confined to the Caribbean and tropical Pacific and is separated from the return flow region by a band of northerly winds. Twenty-four hours later (Fig. 2), *w* on the Texas coast within the return flow is essentially unchanged, while the mT air (15 g kg^{-1} *w* contour) has been advected into the western Gulf. In this particular case, mT air barely reached the coast (in Louisiana) before being cut off by the cold front advancing from the west.

In summary, the current conceptual model of the moist stream states that polar air modifies very quickly to *w* of 9-12 g kg^{-1} and appears on the coast as "return flow" immediately with the onset of southerly winds. Higher *w* values (mT air) cannot be generated over the Gulf itself, and must be advected from the Pacific or Caribbean, thus delaying their arrival on the coast for a day or more after the onset of southerly flow.

The vertical structure evident during the 10-12 March event also differs substantially from the severe weather inducing mT air and dry line (cT air) complex, which is often regarded as the mature stage of return flow. Fig. 3 shows a cross section along the northern Gulf coast at the same time as Fig. 2. This complicated structure shows mM air on the surface from Victoria, TX (VCT) to Boothville, LA (BVE); this surface moist layer is capped by an inversion. Above the inversion from Lake Charles, LA (LCH) east is relatively stable 'Superior' air, while to the west are regions of much less stable continental Tropical (cT) air, above the surface moisture at VCT and in contact with the surface at Del Rio, TX (DRT), west of the 'dry line.' (*w* decreases from 12 g kg^{-1} at VCT to 4 g kg^{-1} at DRT). Superior and cT air have completely different origins and properties; the former is produced by subsidence within ridges and is quite stable, while the latter is produced by large sensible heat fluxes and dry convection over elevated land areas and has a lapse rate near the dry adiabatic.

In this particular case, the progression was cut short by the arrival of the next cold front (just west of the section in Fig. 3). It is suggested that in severe weather events later in the season, a structure like that shown in Fig. 3 becomes destablized as the air masses above the inversion are displaced eastward, and comes to resemble the 'lid' model of Carlson and Ludlum (1968), with the severe weather threat on the western flank of the cT air. In Fig. 3. the western flank of the cT air is not even evident, and most of the region is capped by very stable Superior air.

List of Figures

Fig. 1. Surface analysis for 00 UT 11 March 1988. Solid lines are isobars (2 hPa intervals), and dashed lines are mixing ratio contours (g kg^{-1}). Horizontal shading indicates regions where

the mixing ratio is greater than the local equilibrium value, and vertical shading indicates regions where it is less. Winds and mixing ratios at selected stations are also plotted.

Fig. 2. Same as Fig. 1 except for 00 UT 12 March 1988.

Fig. 3. Cross section along the northern Gulf Coast from Del Rio, TX (DRT) to Apalachicola, FL (AQQ) at 00 UT 12 March 1988. Solid lines are isentropes, (C) and dashed lines are contours of mixing ratio (g kg^{-1}). Shading indicates mixing ratios of 8-10 g kg^{-1} and 10-12 g kg^{-1}. Heavy solid lines indicate air mass boundaries.

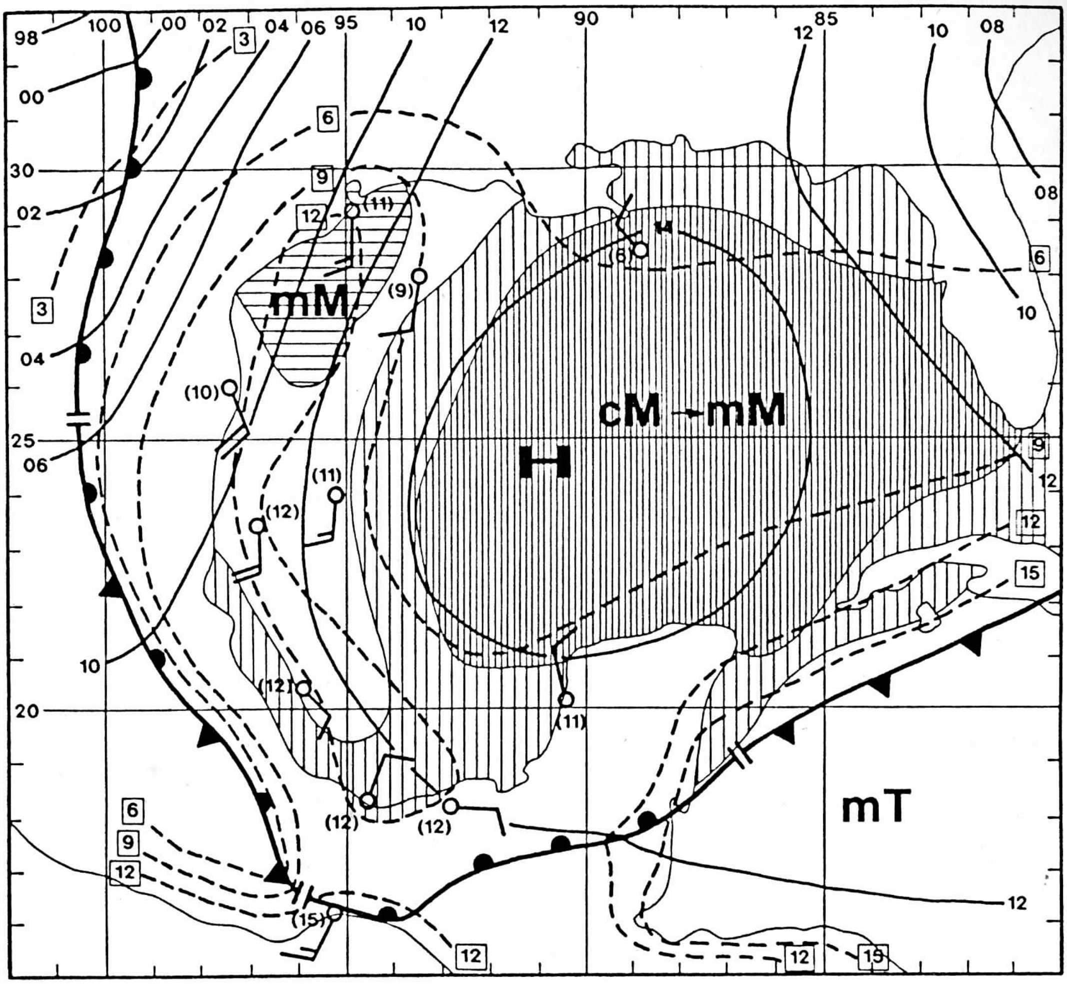

Figure 1

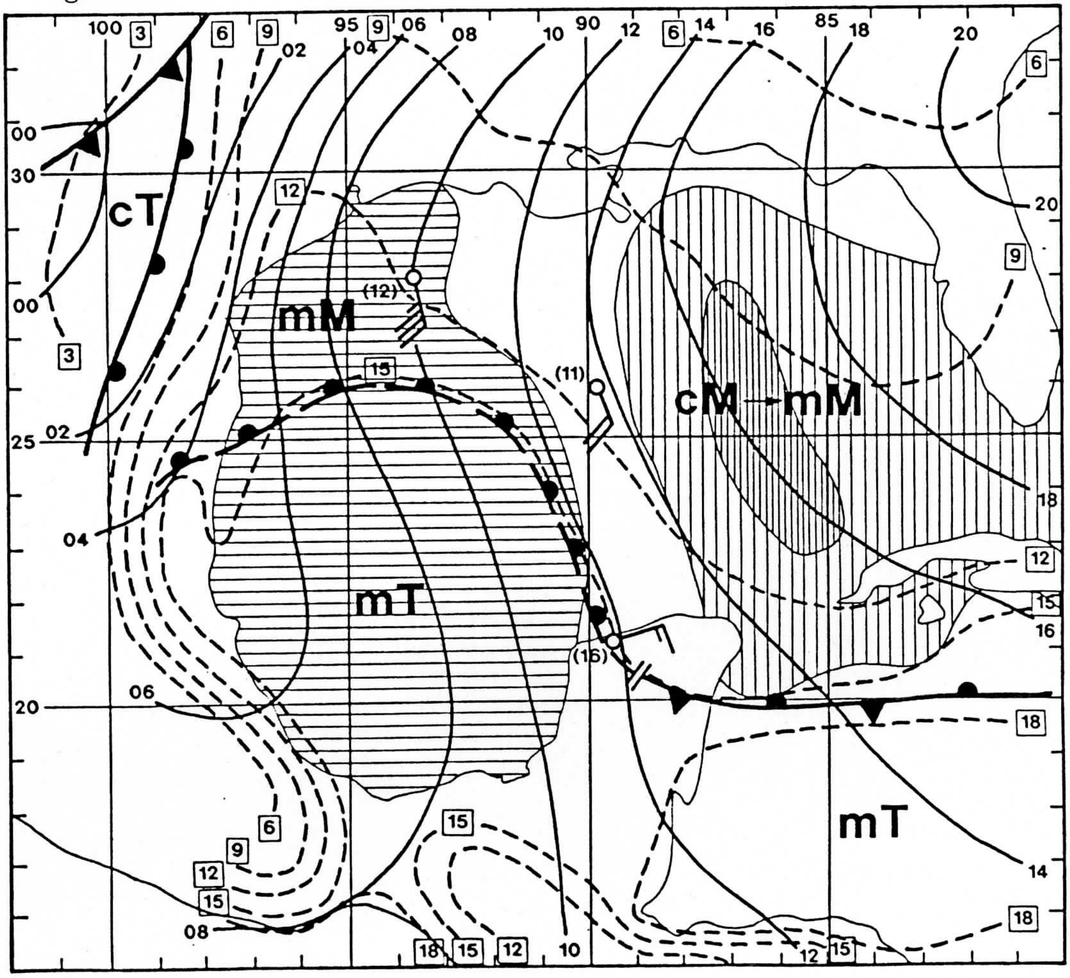

Figure 2

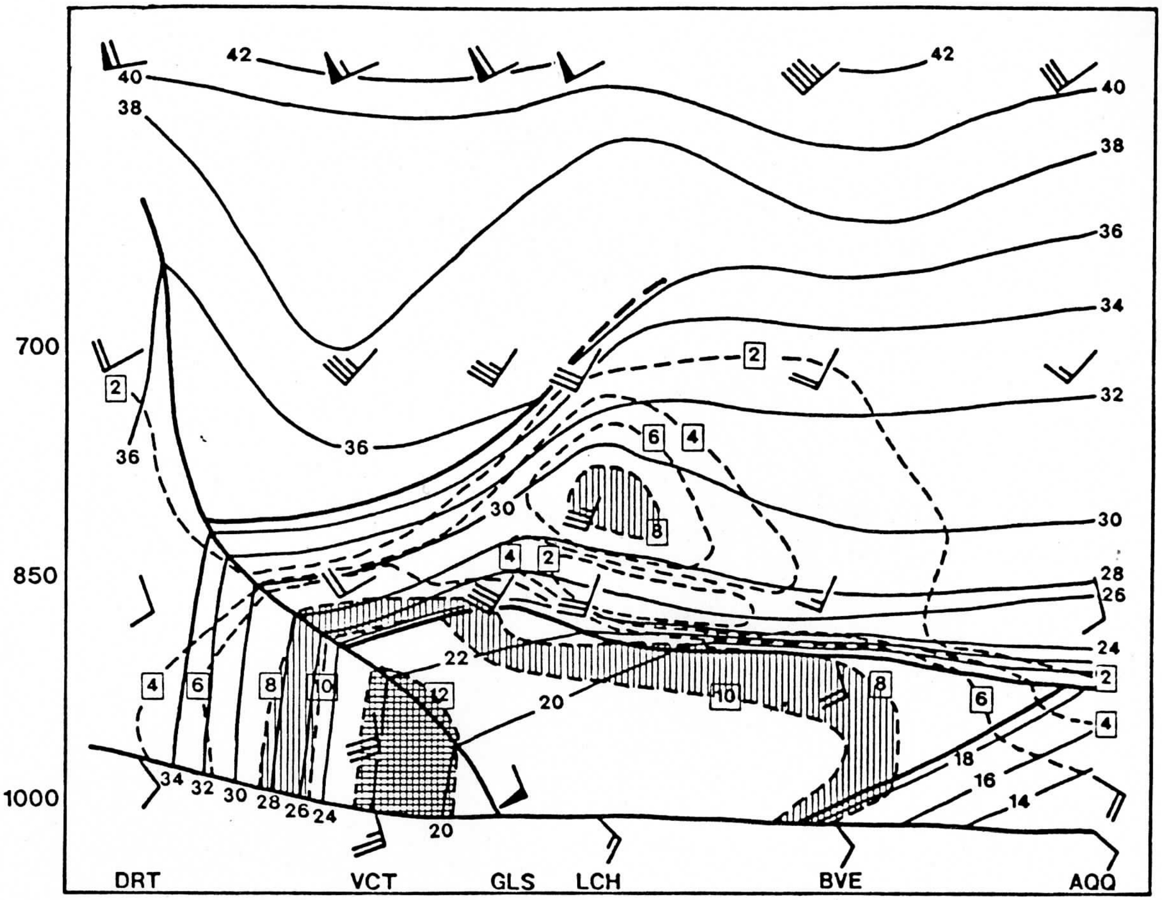
700
850
1000
DRT
VCT
GLS
LCH
BVE
AQQ
42
40
38
36
34
32
30
28
26
24
22
20
18
16
14
2
4
6
8
10
12

Figure 3

B. A comparison of VAS derived moisture retrievals with the RAFS 12 hour forecast over the Gulf of Mexico. Contributed by Anthony J. Schreiner

Introduction

The use of satellite-derived atmospheric parameters to augment regions void of conventional data has been operationally in practice for many years. Emphasis has been on the derivation of estimates of the temperature, wind, and precipitation (O'Lenic 1986; Menzel et al., 1983; Hayden et al., 1981; and Chesters et al., 1983). Recently, interest in the remote detection of water vapor has increased. In that vain, research work was performed which compared remotely sensed moisture profiles in the form of layers to the Regional Analysis and Forecast System (RAFS) 12 hour forecast and to the conventional rawinsondes surrounding the Gulf of Mexico. The moisture profiles are generated from the relatively high spatial resolution of the VISSR Atmospheric Sounder (VAS).

Methodology

The theory, methodology, and procedures are discussed in detail in Schreiner et al. (1992). In short, the retrieval algorithm used to generate the temperature-moisture profiles is a "tunable" version (Hayden, 1988) of the simultaneous method described in Smith et al. (1985). The dwell sounds are obtained in two pieces, 1248 UT (northern half) and 1318 UT (southern half), due to operational time restrictions. The area of coverage is from 17°-50°N. VAS radiances are processed at a nominal horizontal resolution of 80-100 km, which corresponds to an 11 X 11 array of small detector fields of view (fov). Filtering is performed to eliminate fov's which are cloud contaminated.

The 40 levels of mixing ratio generated by the retrieval algorithm are converted to layers of precipitable water in analyzed sigma layers. The layers are enclosed by the sigma values of 0.9, 0.7, and 0.3, which approximate the lowest 100, 300, and 700 MB of the atmosphere. These are examined over three geographical regimes; the full region (18°-45°N, 65°-110°W); the southeastern United States (32°-40°N, 74°-94°W); and the Gulf of Mexico region (18°-31°N, 70°-98°W). For all verifications, the rawinsonde serves as the standard. The layered precipitable water for the rawinsonde is calculated by vertically integrating the temperature-moisture profiles to 300 MB. The rawinsonde values are compared to a "RAFS-surface" analysis and a "VAS" moisture objective analysis on a point-by-point basis. The analyses are made using the three-dimensional recursive -filter analysis method (Hayden and Purser, 1988) using a horizontal latitude-longitude grid resolution of 1.5° and a vertical coordinate with ten sigma levels. The RAFS-surface analysis is comprised of the RAFS 12 hour forecast and includes analyzed, conventional surface data corresponding to the starting time of the dwell sound pair. It is effectively the first guess to the retrieval. The VAS analysis is derived from satellite data, using the RAFS-surface analysis as a background field to smooth over gaps in the remotely sensed moisture fields. From the comparisons of the rawinsonde standard to analyzed fields, values of average difference and variance are calculated.

Results

The statistical results which discussed, are derived from data spanning January 1989 through May 1990. Each month's sample contains 12-18 days when retrievals were processed, and each day offers about 60 rawinsonde comparisons. Some of the more salient observations are discussed below.

- The means for all three data sources track very closely, with the exception that the VAS-derived analyses are more moist at the higher values of total precipitable water in both an absolute and a relative sense [e.g., in the Gulf of Mexico (Fig. 1) during the summer months].
- The Gulf shows a variance global minimum during the summer for all data sources, indicating the benign subtropical air mass as seen in Fig. 2a. This minimum is not seen in the full region (Fig. 2b).
- The RAFS-surface analysis shows generally the lowest variance for all three regions.
- The VAS sounding information consistently gives a slightly higher RMSD than the RAFS-surface analyses at nearly all times of the year. Exceptions occur, such as during the fall of 1989 over the Gulf of Mexico (Fig. 3). Some of the increases can be attributed to the higher variance of the VAS data.

Of the results, the most significant is the VAS moist bias problem. This is more clearly defined in Fig. 4, which shows both the satellite-derived moisture analysis and the RAFS-surface analysis difference from the rawinsonde precipitable water vapor for the Gulf of Mexico region. The figure indicates a negative (moist) bias for the period May-September 1989 and shows indications of it repeating during the summer months of 1990. This moist bias is not observed in the RAFS-surface-derived analysis at any layer or region. Although bias corrections to atmospheric temperature-sensitive channels were routinely applied in the VAS processing, there was during this period no correction implemented for bands 7 and 8 (11.2 and 12. 7 micrometer, long wave window channels) or bands 9 and 10 (7.3 and 6.7 micrometer, water vapor channels) because of the difficulty in establishing a ground truth. It is highly probable that a bias in one or all of these bands is contributing to the observed bias in the precipitable water estimates.

The ability of the VAS-derived moisture analyses to delineate moisture in the Gulf of Mexico region vertically was also examined. The same statistical date set described earlier is used to compare the three layers (sfc.-0.90, 0.90-0.70, and 0.70-0.30 sigma layers). Some of the conclusions follow.

- The monthly means indicate that the middle, 0.90-0.70 sigma layer (Fig. 5) contributes substantially more of the precipitable water vapor than the surrounding layers during June through September.
- The top layer (0.70-0.30 sigma layer, Fig. 6) is the only layer where the VAS-derived analysis relative to the RAFS-surface analysis changes from relatively moist during the summer to relatively dry during the remainder of the year. This is probably a real signal as the VAS moisture channels are not likely to be affected by moisture above this layer (as they are at lower layers) and it is well sampled by bands 9 and 10.
- With the exception of the top layer, the rawinsonde data exhibits a higher variance throughout the period of this study. The RAFS-surface analysis shows generally the lowest variance (Fig. 7).
- RMSD of the three layers in the Gulf of Mexico region (Fig. 8) shows that the largest discrepancies between the satellite-derived moisture and the RAFS-surface analysis occur in the 0.90-0.70 sigma layer (Fig. 8c).

Summary

Satellite-derived moisture soundings in the form of layered values have been shown to give mixed results when compared to the RAFS 12 hour forecast using rawinsonde reports as the definition of the "truth." It is found that the VAS parallels the seasonal change in variance, observed in the conventional information, more closely than the RAFS 12 hour forecast. At the same time, the VAS-derived moisture seems to have a wet bias relative to both the RAFS and the rawinsonde. Despite the inherent smoothing of the remote soundings in the vertical, the VAS-derived moisture still displays a high variance in the horizontal.

Based on monthly statistics, the VAS appears to be slightly less accurate over land than the RAFS-surface analyses, with inconsistent results over the Gulf of Mexico. In terms of variance, the VAS analyses are more closely aligned to the rawinsonde over the Gulf of Mexico. Some of this may be related to air mass types that exist over the Gulf of Mexico. For example, a continental polar air mass moving over the Gulf would be expected to be well forecast as it progressed farther southward, due to an ample amount of rawinsonde information available. Conversely, air masses originating over Mexico or from the Caribbean Sea may not be represented well by the RAFS-surface analysis, given the lack of rawinsonde measurements in this region (Weiss, 1990). There is evidence that the VAS can make appropriate adjustments to three layers from the surface to 0.3 sigma, although adjustments at the extreme layers are minimal because of either the heavy influence of the first guess (sfc.-0.90 sigma layer) or the lack of reliable information for verification (0.70-0.30 sigma layer).

List of Figures

Figure 1. A monthly mean plot of precipitable water (mm) from January 1989 through May 1990 for the surface to 0.30 sigma layer, based on the Gulf of Mexico. The data points connected by the solid line represent the rawinsonde observation. Data points connected by the long dashed line are based on the RAFS-surface analysis, where the RAFS in this case is the 12 hour forecast valid at 1200 UT. VAS-derived moisture analyses are indicated by the data points connected by the short-dashed line. Total number of data points is 1923.

Figure 2. Same as Fig. 1, except monthly variance is plotted for (a) the Gulf of Mexico region and the total number of data points is 1923 and (b) the full region and the total number of data points is 9340.

Figure 3. Same as Fig. 1, except monthly root-mean-square-difference (RMSD) is plotted.

Figure 4. Same as Fig. 1, except the monthly bias is plotted for the VAS-derived moisture and the RAFS-surface analyses relative to the rawinsonde observations, where negative indicates a moist bias.

Figure 5. Same as Fig. 1, except the data is for the surface to 0.90 sigma layer.

Figure 6. Same as Fig. 1, except the data is for 0.70-0.30 sigma layer

Figure 7. Same as Fig. 1, except monthly variance is plotted for (a) the surface to 0.90 sigma layer, (b) the 0.90-0.70 sigma layer, and (c) the 0.70-0.30 sigma layer.

Figure 8. Same as Fig. 1, except monthly RMSD is plotted for (a) the surface to 0.90 sigma layer, (b). the 0.90-0.70 sigma layer, and (c) the 0.70-0.30 sigma layer

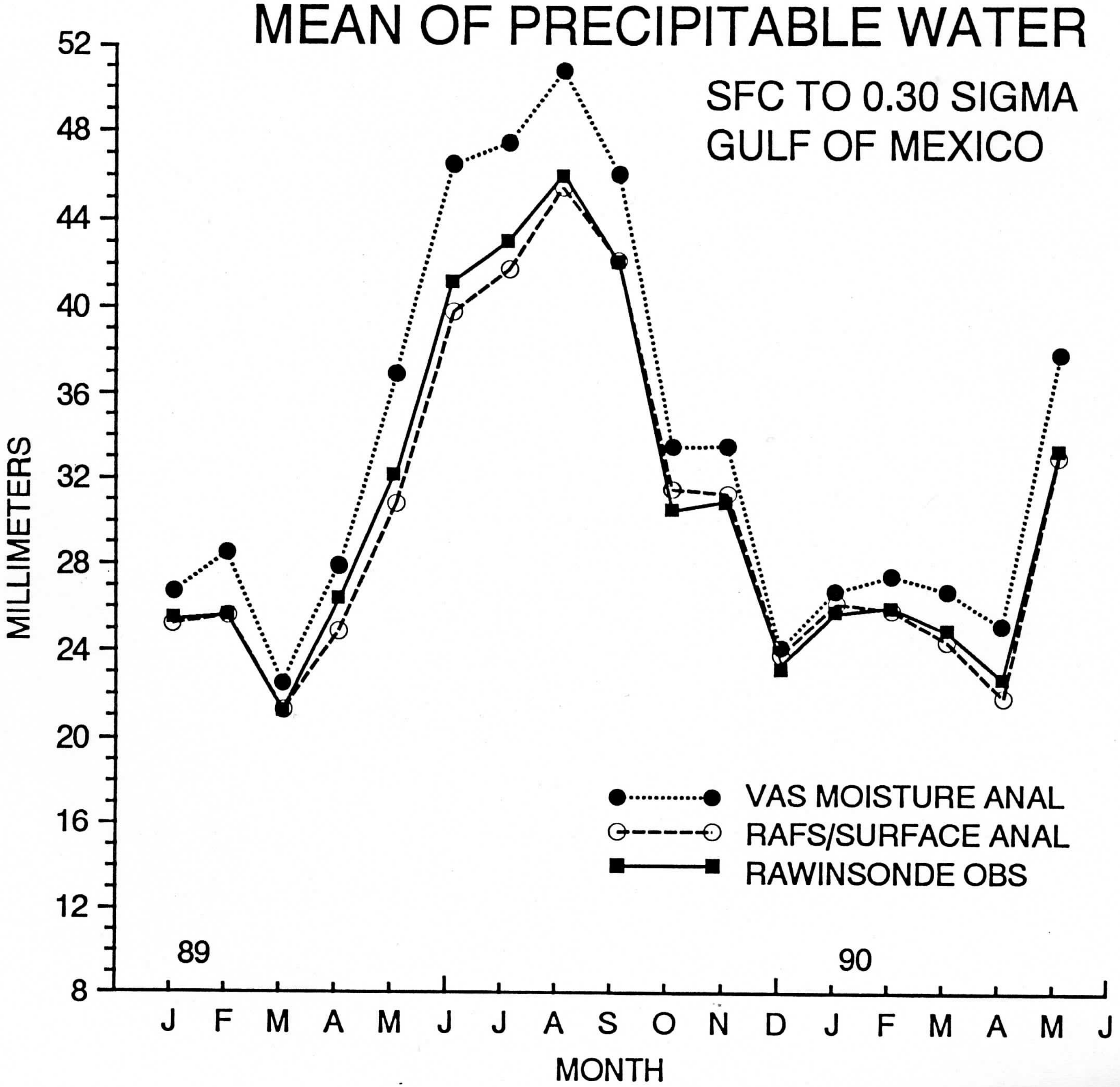
MEAN OF PRECIPITABLE WATER
SFC TO 0.30 SIGMA
GULF OF MEXICO
MILLIMETERS
52
48
44
40
36
32
28
24
20
16
12
8
89
90
J
F
M
A
M
J
J
A
S
O
N
D
J
F
M
A
M
J
MONTH
VAS MOISTURE ANAL
RAFS/SURFACE ANAL
RAWINSONDE OBS

Figure 1

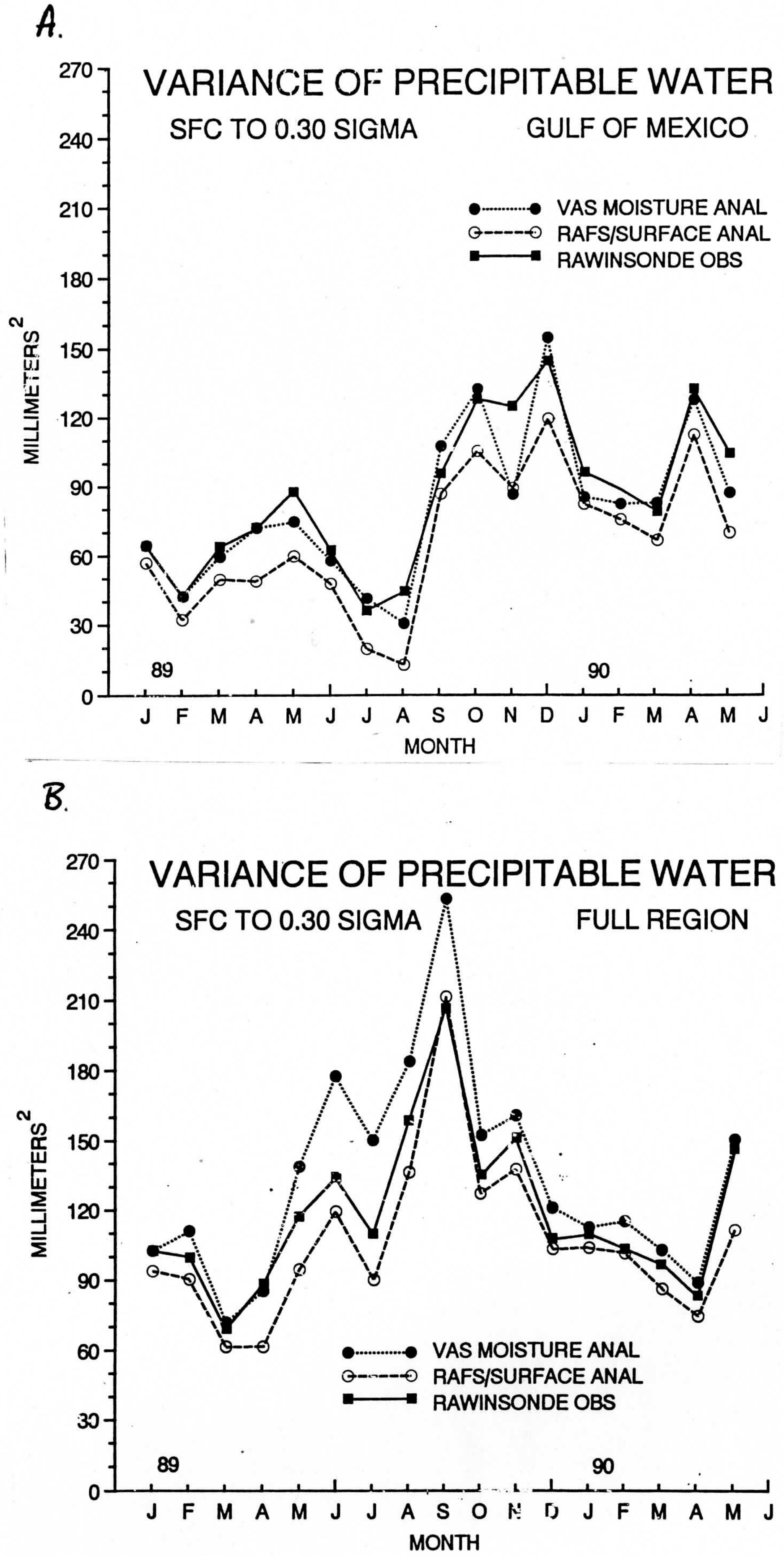A.
VARIANCE OF PRECIPITABLE WATER
SFC TO 0.30 SIGMA
GULF OF MEXICO
VAS MOISTURE ANAL
RAFS/SURFACE ANAL
RAWINSONDE OBS
MILLIMETERS^2
0
30
60
90
120
150
180
210
240
270
89
90
J F M A M J J A S O N D J F M A M J
MONTH
B.
VARIANCE OF PRECIPITABLE WATER
SFC TO 0.30 SIGMA
FULL REGION
VAS MOISTURE ANAL
RAFS/SURFACE ANAL
RAWINSONDE OBS
MILLIMETERS^2
0
30
60
90
120
150
180
210
240
270
89
90
J F M A M J J A S O N D J F M A M J
MONTH

Figure 2

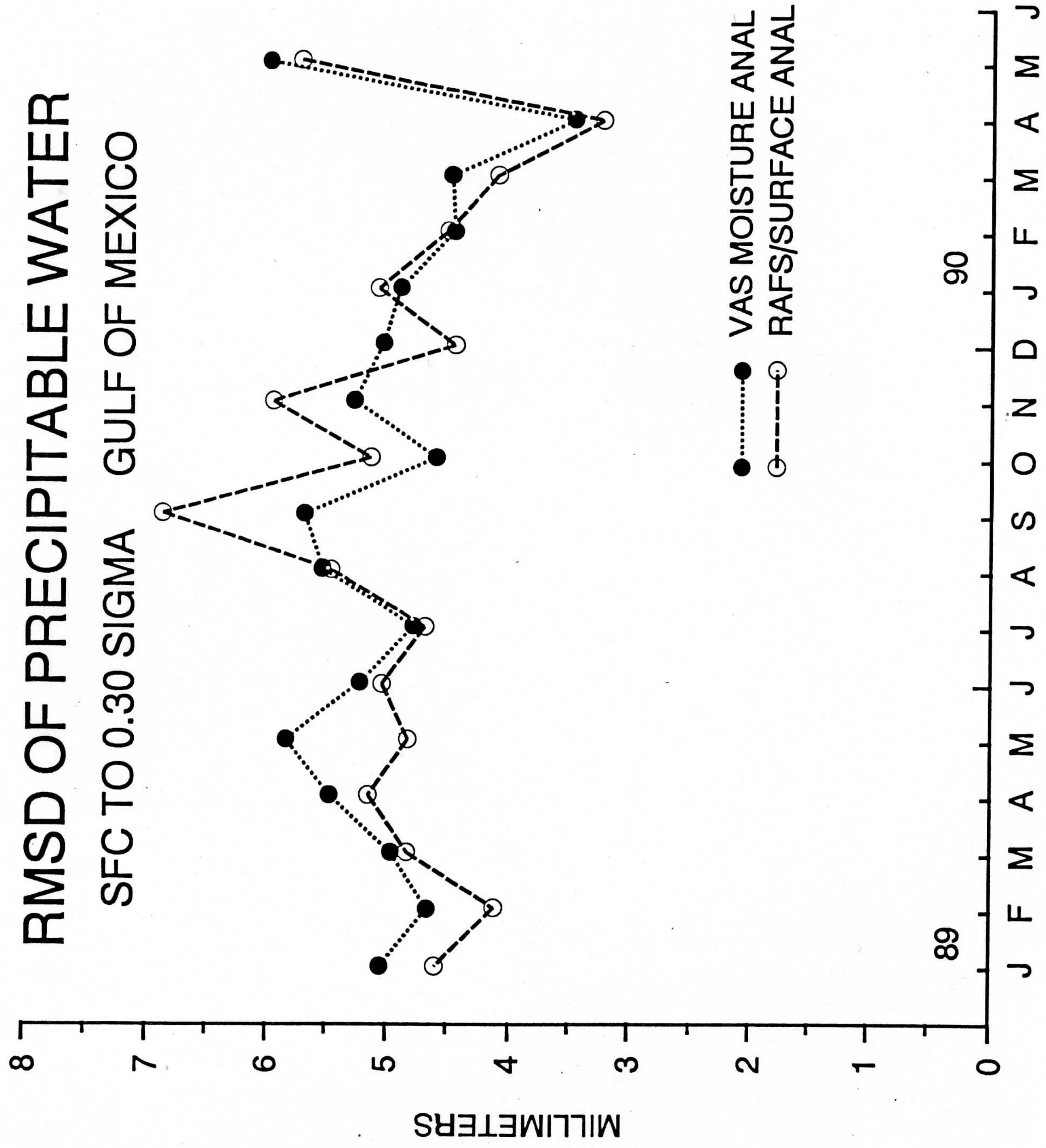
RMSD OF PRECIPITABLE WATER
SFC TO 0.30 SIGMA GULF OF MEXICO
MILLIMETERS
0
1
2
3
4
5
6
7
8
J F M A M J J A S O N D J F M A M J
89
90
MONTH
VAS MOISTURE ANAL
RAFS/SURFACE ANAL

Figure 3

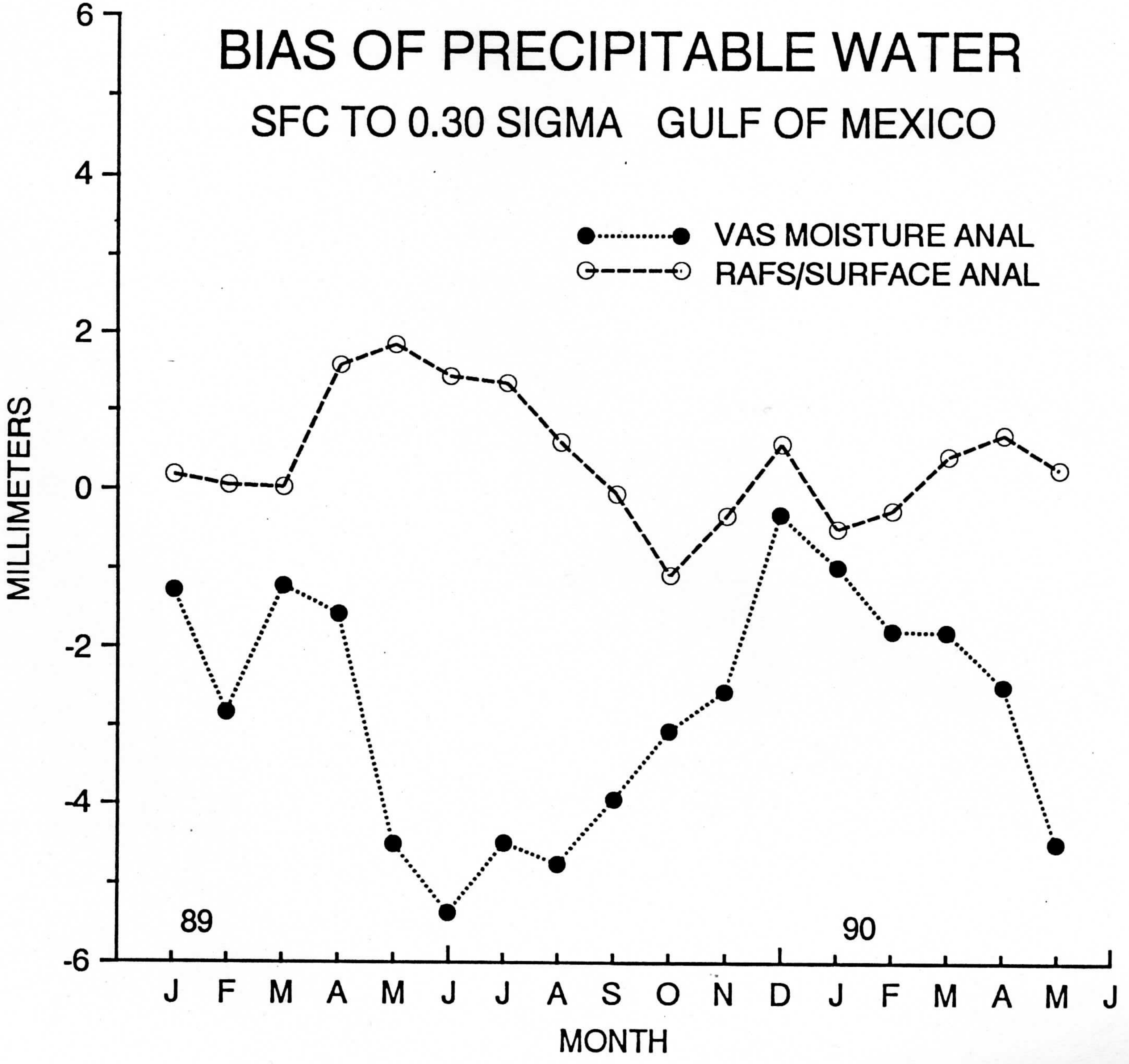
BIAS OF PRECIPITABLE WATER
SFC TO 0.30 SIGMA GULF OF MEXICO
● VAS MOISTURE ANAL
○ RAFS/SURFACE ANAL
MILLIMETERS
6
4
2
0
-2
-4
-6
89
90
J F M A M J J A S O N D J F M A M J
MONTH

Figure 4

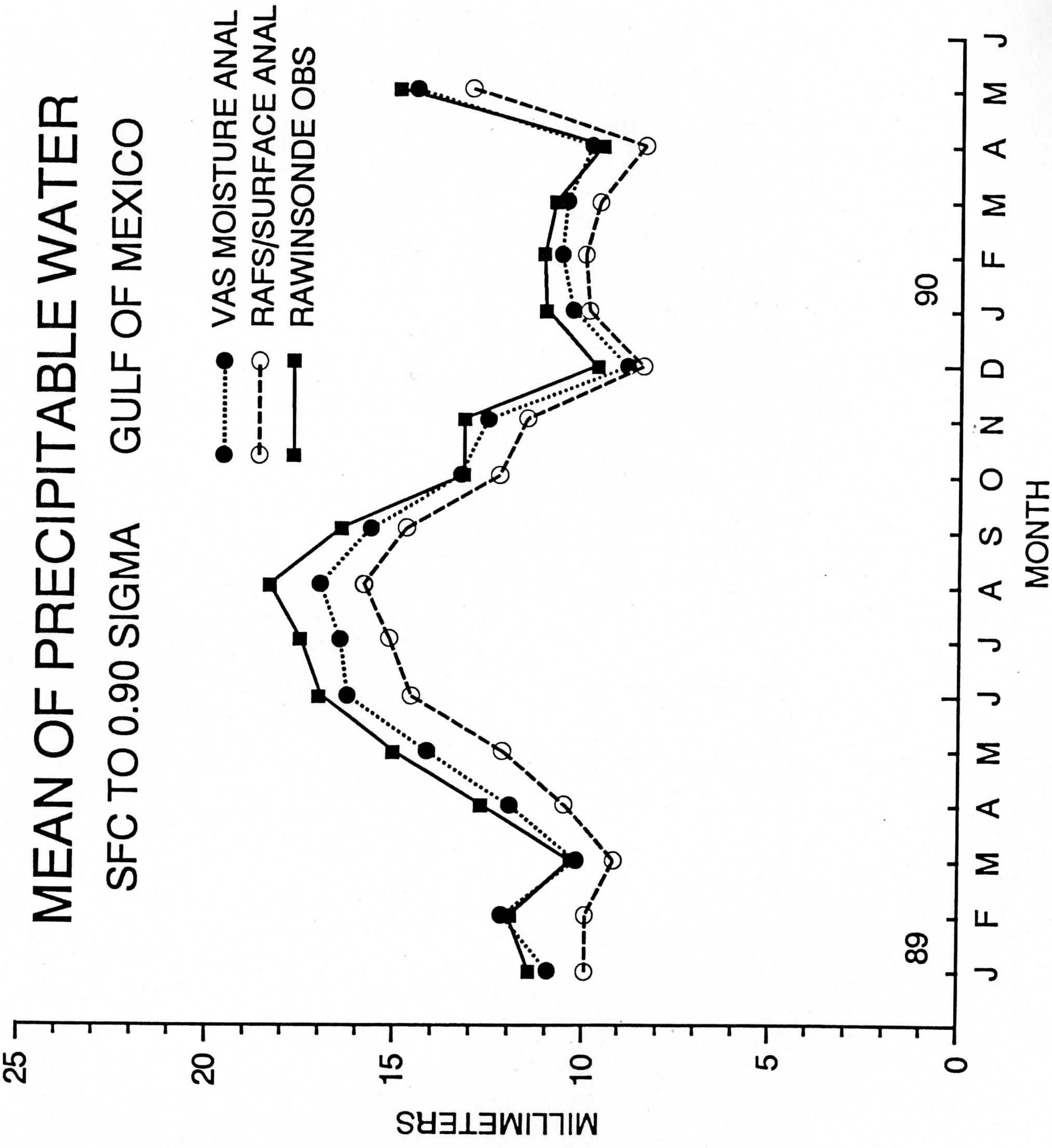
MEAN OF PRECIPITABLE WATER
SFC TO 0.90 SIGMA
GULF OF MEXICO
VAS MOISTURE ANAL
RAFS/SURFACE ANAL
RAWINSONDE OBS
MILLIMETERS
0
5
10
15
20
25
MONTH
J F M A M J J A S O N D J F M A M J
89
90

Figure 5

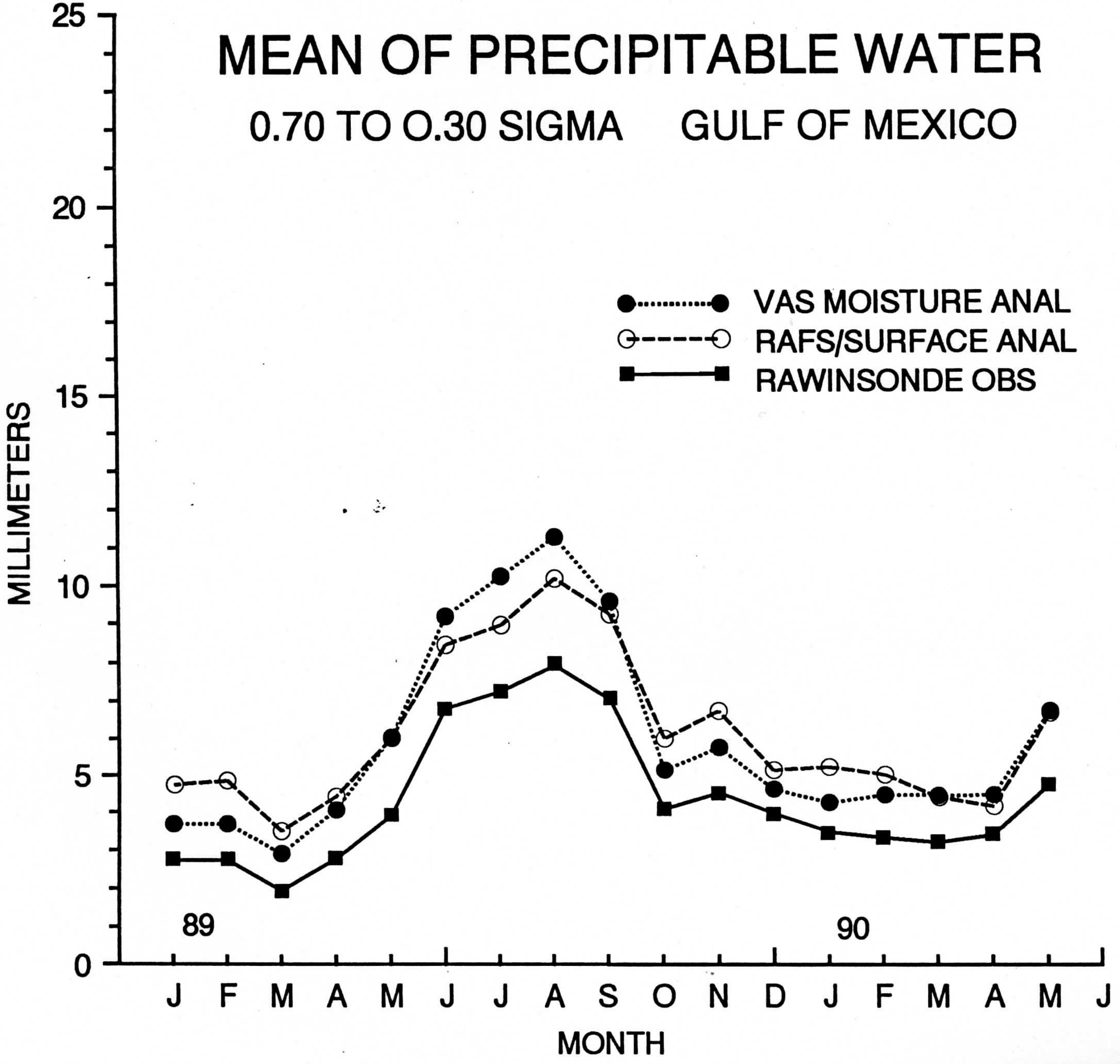
MEAN OF PRECIPITABLE WATER
0.70 TO O.30 SIGMA GULF OF MEXICO
VAS MOISTURE ANAL
RAFS/SURFACE ANAL
RAWINSONDE OBS
MILLIMETERS
25
20
15
10
5
0
89
90
J
F
M
A
M
J
J
A
S
O
N
D
J
F
M
A
M
J
MONTH

Figure 6

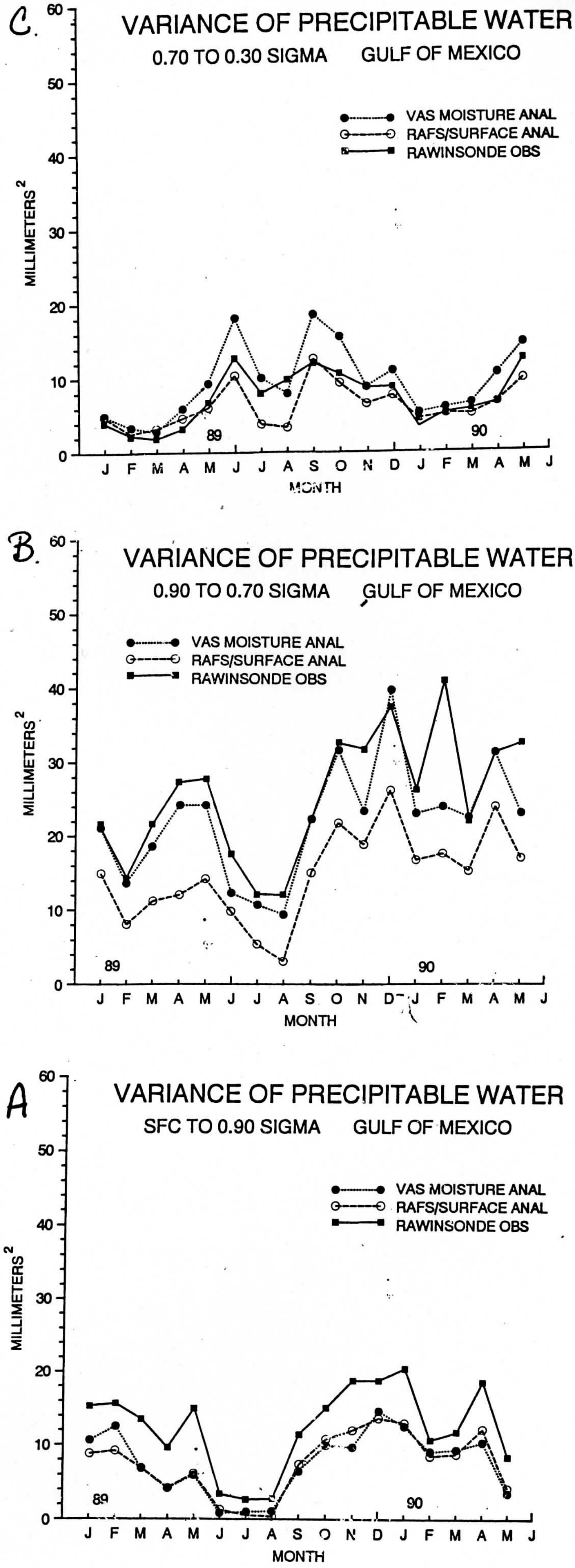C.
VARIANCE OF PRECIPITABLE WATER
0.70 TO 0.30 SIGMA GULF OF MEXICO
VAS MOISTURE ANAL
RAFS/SURFACE ANAL
RAWINSONDE OBS
MILLIMETERS^2
0
10
20
30
40
50
60
89
90
J F M A M J J A S O N D J F M A M J
MONTH
B.
VARIANCE OF PRECIPITABLE WATER
0.90 TO 0.70 SIGMA GULF OF MEXICO
VAS MOISTURE ANAL
RAFS/SURFACE ANAL
RAWINSONDE OBS
MILLIMETERS^2
0
10
20
30
40
50
60
89
90
J F M A M J J A S O N D J F M A M J
MONTH
A
VARIANCE OF PRECIPITABLE WATER
SFC TO 0.90 SIGMA GULF OF MEXICO
VAS MOISTURE ANAL
RAFS/SURFACE ANAL
RAWINSONDE OBS
MILLIMETERS^2
0
10
20
30
40
50
60
89
90
J F M A M J J A S O N D J F M A M J
MONTH

Figure 7

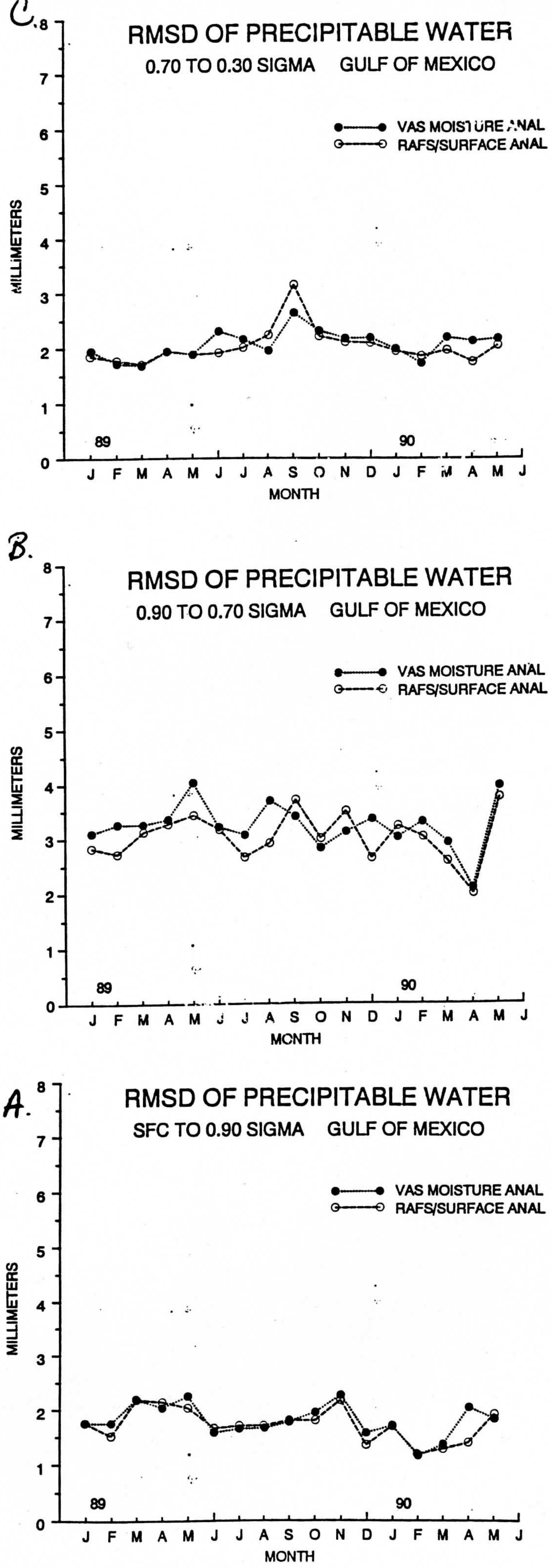
C.
RMSD OF PRECIPITABLE WATER
0.70 TO 0.30 SIGMA GULF OF MEXICO
VAS MOISTURE ANAL
RAFS/SURFACE ANAL
MILLIMETERS
0
1
2
3
4
5
6
7
8
89
90
J F M A M J J A S O N D J F M A M J
MONTH
B.
RMSD OF PRECIPITABLE WATER
0.90 TO 0.70 SIGMA GULF OF MEXICO
VAS MOISTURE ANAL
RAFS/SURFACE ANAL
MILLIMETERS
0
1
2
3
4
5
6
7
8
89
90
J F M A M J J A S O N D J F M A M J
MONTH
A.
RMSD OF PRECIPITABLE WATER
SFC TO 0.90 SIGMA GULF OF MEXICO
VAS MOISTURE ANAL
RAFS/SURFACE ANAL
MILLIMETERS
0
1
2
3
4
5
6
7
8
89
90
J F M A M J J A S O N D J F M A M J
MONTH

Figure 8

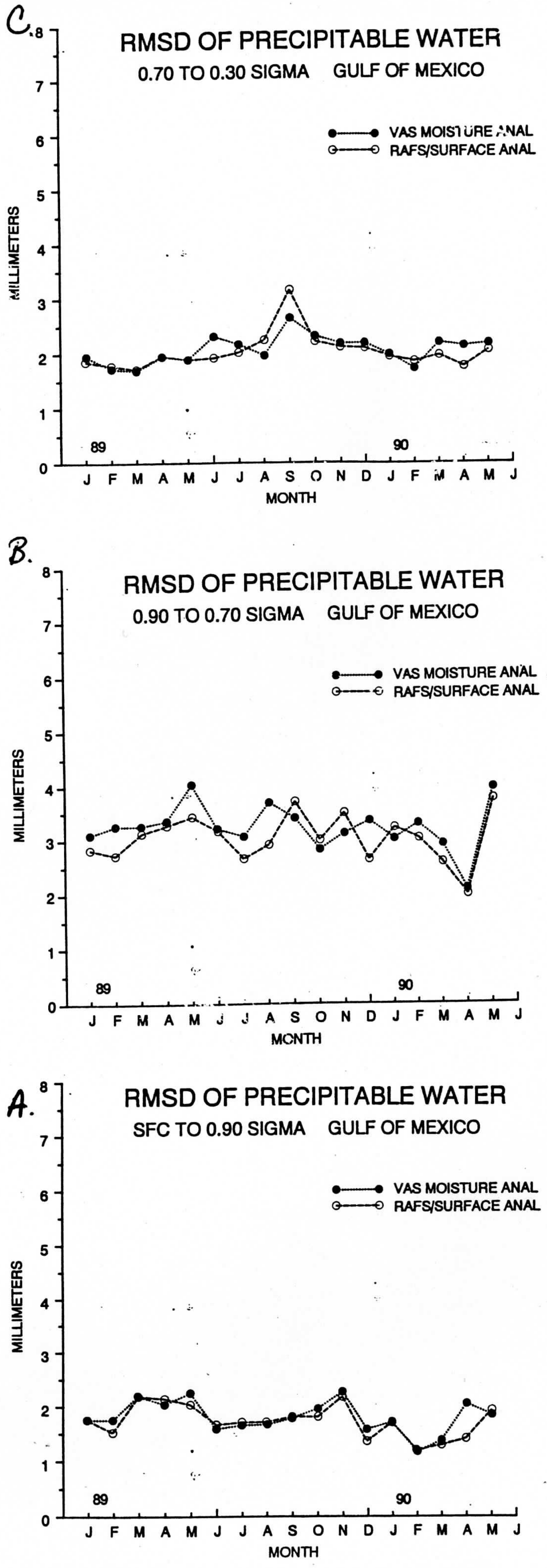
C.
RMSD OF PRECIPITABLE WATER
0.70 TO 0.30 SIGMA GULF OF MEXICO
VAS MOISTURE ANAL
RAFS/SURFACE ANAL
MILLIMETERS
0
1
2
3
4
5
6
7
8
89
90
J F M A M J J A S O N D J F M A M J
MONTH
B.
RMSD OF PRECIPITABLE WATER
0.90 TO 0.70 SIGMA GULF OF MEXICO
VAS MOISTURE ANAL
RAFS/SURFACE ANAL
MILLIMETERS
0
1
2
3
4
5
6
7
8
89
90
J F M A M J J A S O N D J F M A M J
MONTH
A.
RMSD OF PRECIPITABLE WATER
SFC TO 0.90 SIGMA GULF OF MEXICO
VAS MOISTURE ANAL
RAFS/SURFACE ANAL
MILLIMETERS
0
1
2
3
4
5
6
7
8
89
90
J F M A M J J A S O N D J F M A M J
MONTH

Figure 8

C. Monitoring precipitable water and surface wind over the Gulf of Mexico from microwave and VAS satellite imagery. Contributed by Gary S. Wade.

GUFMEX.

GUFMEX research with VAS sounding data was the subject of several presentations and publications supported by the Severe Weather Program: presentation at the Symposium on Air-Sea Interaction and Air Mass Modification (Galveston, TX Jan. 91); publication in Weather and Forecasting (Vol. 6, No. 2, Jun. 91, pp. 227-243) of: "Monitoring precipitable water and surface wind over the Gulf of Mexico from microwave and VAS satellite imagery"; and publication in the Journal of Applied Meteorology of: "Layered precipitable water from the infrared VAS sounder during a return flow event over the Gulf of Mexico" (accepted for July, 1992). [Authors for all of the above were: R. M. Rabin, L. A. McMurdie, C. M. Hayden, and G. S. Wade.]

A. Symposium

At the symposium, three topics were separately covered by three of the co-authors. L. A. McMurdie explained the use of microwave measurements from the SSM/I instrument, to determine the total precipitable water pattern over ocean surfaces. G. S. Wade then presented results from the VAS (infrared) instrument for the 10-12 March 1988 GUFMEX case, and compared the VAS data with the SSM/I and special GUFMEX rawinsonde data. R. M. Rabin described efforts to determine the water budget over the Gulf, using both SSM/I data and NMC model fields, for a strong cold air outbreak in December 1990 and January 1991. (See - Scoggins, J. R., J. Arellano, Jr., B. Esposito, G. A. Johnson, and K. C. Brundidge, 1991: Report on a Symposium on Air-Sea Interaction and Air Mass Modification over the Gulf of Mexico 7-9 January 1991, Galveston, Texas. Bull. Amer. Meteor. Soc., Vol. 72, No. 6, pp. 827-832.)

B. Weather and Forecasting Article

Total precipitable water values were compared for three data sources: SSM/I (microwave), VAS (infrared), and rawinsonde (both NWS and CLASS sites). Accuracy of the precipitable water (PW) derived from the SSM/I and VAS were comparable (see Figure 1); standard errors were only about 3 to 4 mm. The microwave data provided more uniform coverage, when available, than the VAS, since they were relatively free from cloud contamination; the SSM/I moisture fields also appeared less noisy than the VAS fields. However, the VAS, with a geostationary perspective, has the potential to provide more complete monitoring, in space and time, than the SSM/I on a polar orbiting platform. In addition, as a sounding device, the VAS has some limited capacity to determine moisture distributions in the vertical. Trends in the PW at specific locations were generally well depicted by the satellite moisture estimates (see Figure 2); strong drying after the frontal passage was followed by gradual moistening during the southerly return flow. The analyses from the satellite data appeared to add considerable information to the moisture analysis over the Gulf (which was not evident in the visible imagery), and should be helpful in forecasting moisture evolution, particularly moist return flow near coastal areas.

C. Journal of Applied Meteorology Article

An examination of the vertical distribution of the moisture from the VAS data was considered. Precipitable water was estimated for two layers in sigma coordinates (1 to .84 and .84 to .25; or approximately, surface to 850 MB and 850 to 250 MB). The accuracy of the moisture estimates in each vertical layer was less than that for the total PW, but still good, with standard errors of 2 to 3 mm (see figures 3-4). A moist bias existed, especially for the lower PW values. An examination of the ratio of the lower layer PW to the total PW, showed lower values for the VAS compared to the rawinsondes (see Figure 5). The relatively poor vertical resolution of VAS is at fault and one cannot with confidence separate layers precisely.

Improvements in the determination of the PW for each layer were observed with respect to the first-guess profiles used in the retrieval process. In the mean, there was a positive impact of about 1 mm, or 25 percent of the initial difference of the guess. About a third of the retrievals had negative impacts. Results were similar for both layers (see Figures 6-7).

Trends of the satellite PW, at the special GUFMEX rawinsonde sites, also showed generally reasonable and consistent evolution of the moisture in the two layers (see figures 8-10). The moist VAS bias is evident.

The total PW fields had shown a triangular maximum in the central Gulf at 1200 UT on 12 March 1988. It is particularly interesting to note how the moisture was partitioned in the vertical for that same time period. At lower levels, the maximum is located in the central western Gulf, while the upper levels appeared most moist in the central Gulf (see Figures 11-12). This more eastward position of the upper layer PW is consistent with the elevated moist layer described by Merrill (1992) (See IIA above).

List of Figures

Fig. 1. Scatter plots of precipitable water (PW) data: (a) rawinsonde vs. SSM/I, (b) rawinsonde vs. GOES-VAS, (c) SSM/I vs. GOES-VAS. Solid line is best fit to data. Data are perfectly correlated if they fall on dashed line. Ellipse indicates the shape of data distribution.

Fig. 2. Time series of total precipitable water for some stations in vicinity of the Gulf of Mexico.

Fig. 3. Scatter plots of precipitable water (PW) determined from rawinsonde and VAS data for the surface to 850 MB layer. Solid line is best fit to data. Data are perfectly correlated if the

fall on dashed line. Ellipse indicates the shape of data distribution. Circled points indicate CLASS soundings and solid points indicate conventional rawinsondes.

Fig. 4. Same as Fig. 3, except coverage is for the 850 MB to 250 MB layer.

Fig. 5. Same as Fig. 3, except the ratio (R) for the lower layer is compared. R is defined as: PW1/total precipitable water, where PW1 is precipitable water of the lower layer.

Fig. 6. Difference in precipitable water (PW) between rawinsonde and guess (circles), and between rawinsonde and VAS retrievals (crosses) as function of precipitable water for the surface to 850 MB layer.

Fig. 7. Same as Fig. 6, except for the 850 MB to 250 MB. layer.

Fig. 8. Time series at Brownsville, TX of layered precipitable water and ratio R from VAS and rawinsondes in vicinity of the Gulf of Mexico. Solid and dashed curves in the upper plots give lower (surface to 850 MB) and upper layer (850 MB to 250 MB) precipitable from rawinsonde. The corresponding VAS values are indicated by "L" and "H". The VAS and rawinsonde values of R are indicated by the circles and curves in the lower plots.

Fig. 9. Same as Fig. 8, except the location is the US Coast Guard ship Salvia located in the Gulf of Mexico.

Fig. 10. Same as Fig. 8, except the location is a Mobil Oil platform located in the Gulf of Mexico.

Fig. 11. VAS precipitable water image for the layer sfc. to 850 MB. Rawinsonde values of precipitable water are plotted along with the surface wind for the times indicated under each image.

Fig. 12. Same as fig. 11, except the precipitable water vapor is for the 850 MB to 250 MB layer.

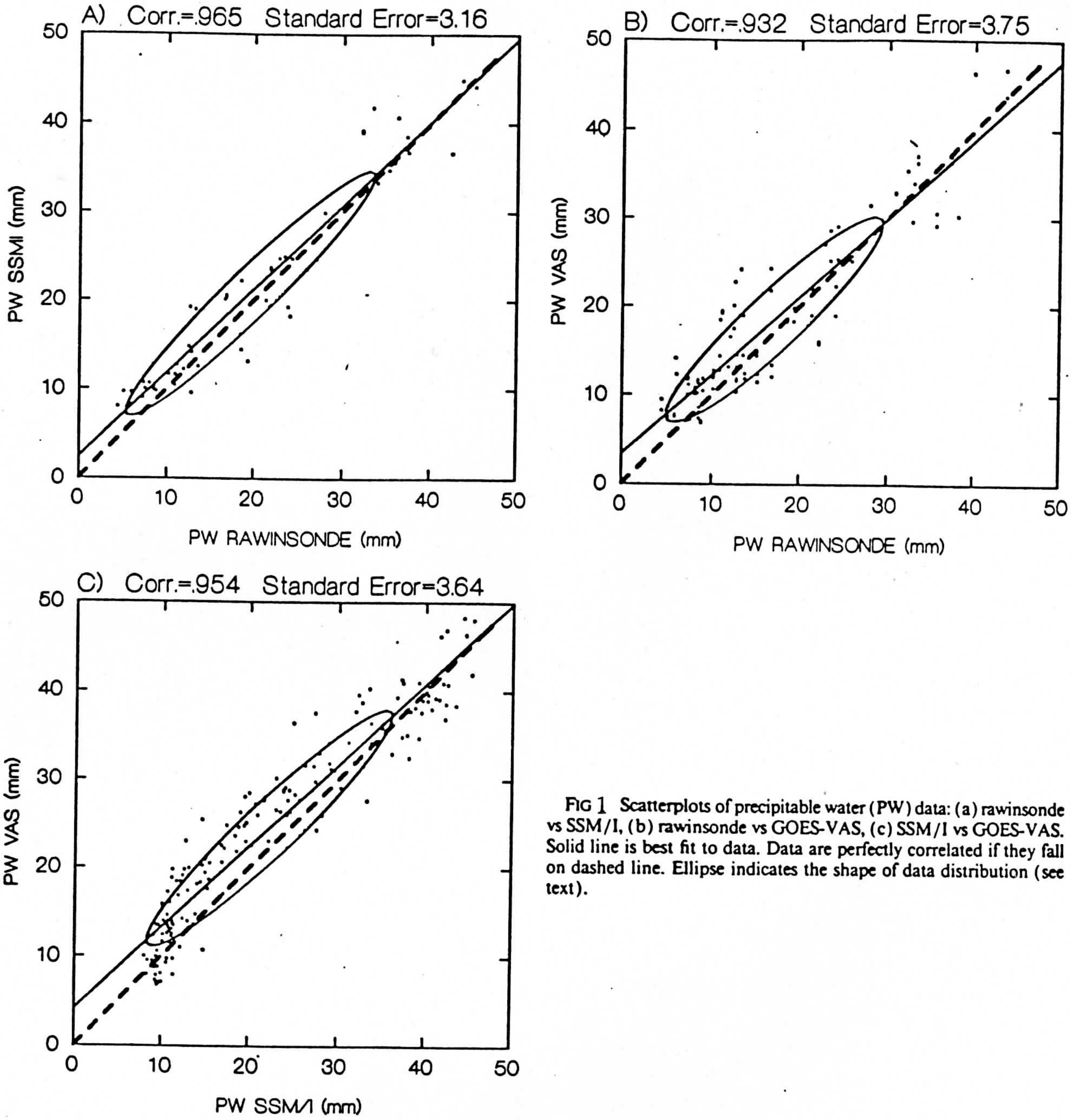

FIG 1 Scatterplots of precipitable water (PW) data: (a) rawinsonde vs SSM/I, (b) rawinsonde vs GOES-VAS, (c) SSM/I vs GOES-VAS. Solid line is best fit to data. Data are perfectly correlated if they fall on dashed line. Ellipse indicates the shape of data distribution (see text).

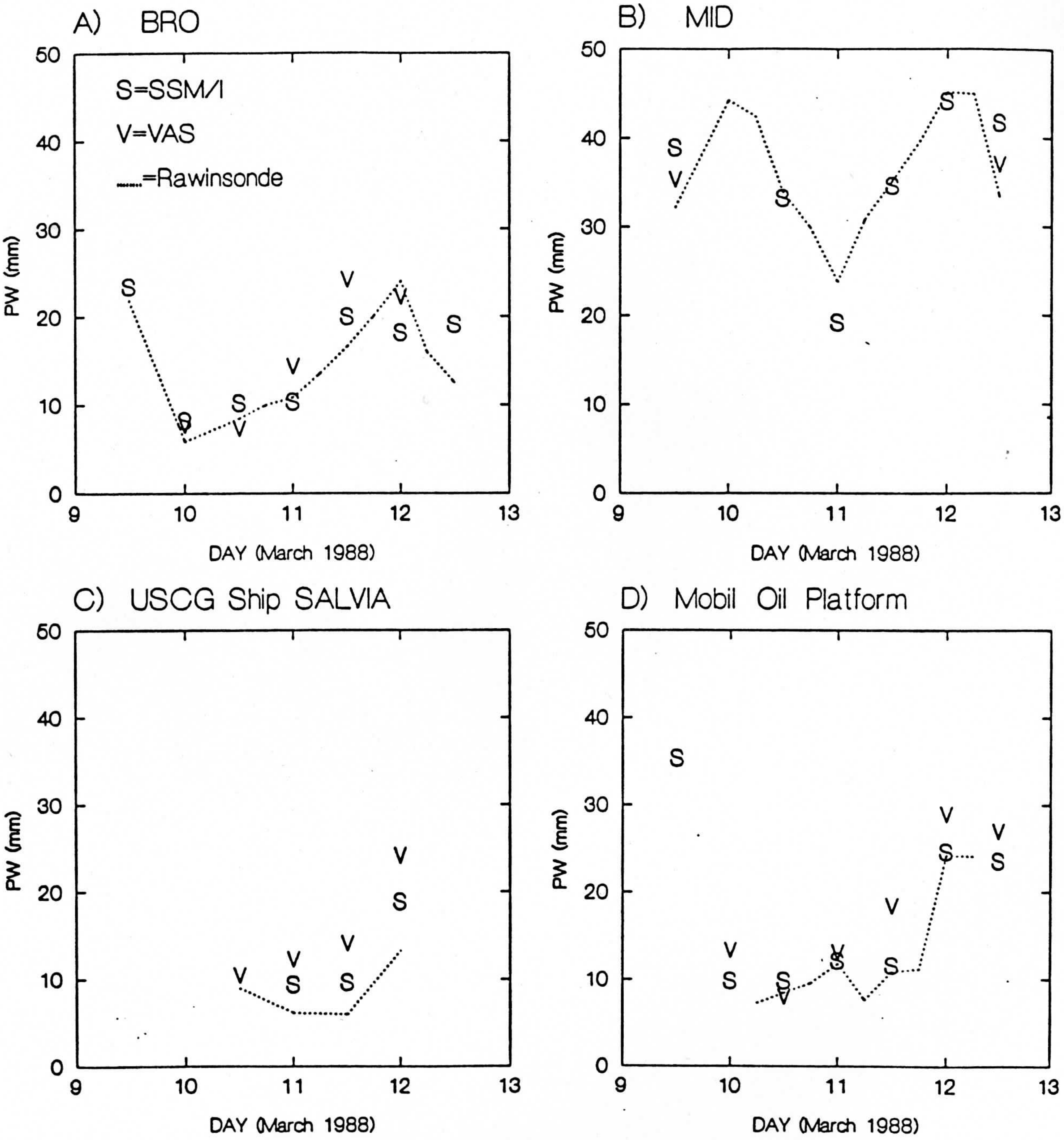

FIG. 2 Time series of total precipitable water for some stations in vicinity of the Gulf of Mexico.

VAS VS. RAWINSONDE-Low Layer

FIG. 3

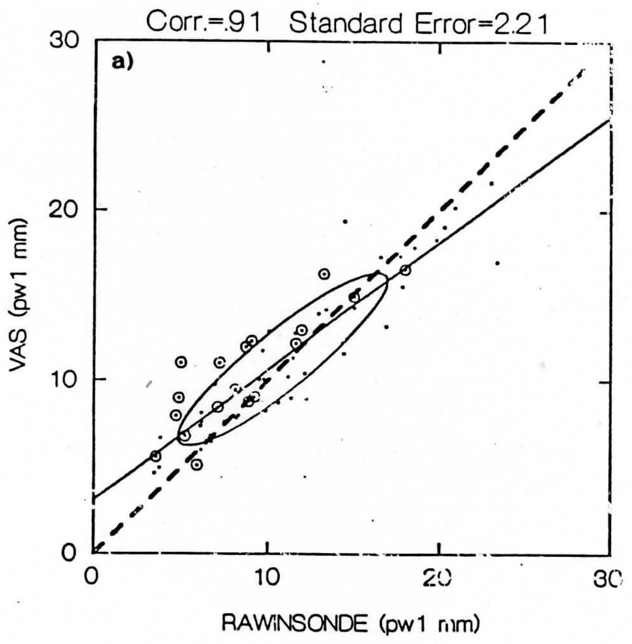

VAS VS. RAWINSONDE-Upper Layer

FIG. 4

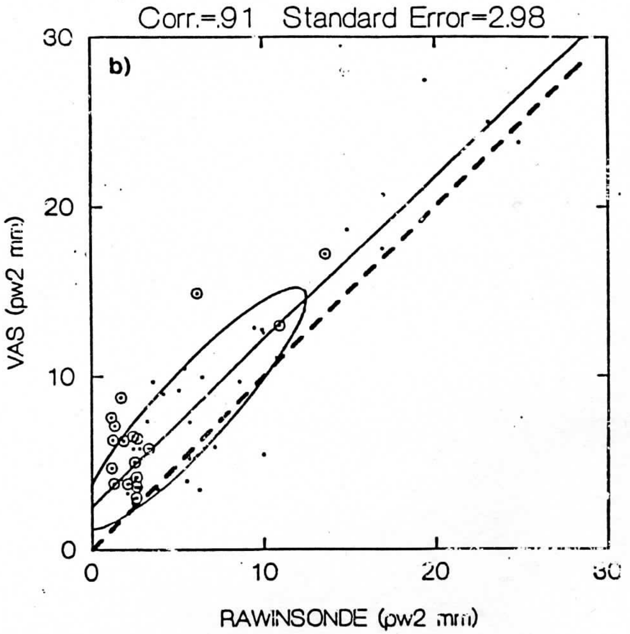

VAS VS. RAWINSONDE-Ratio

FIG. 5

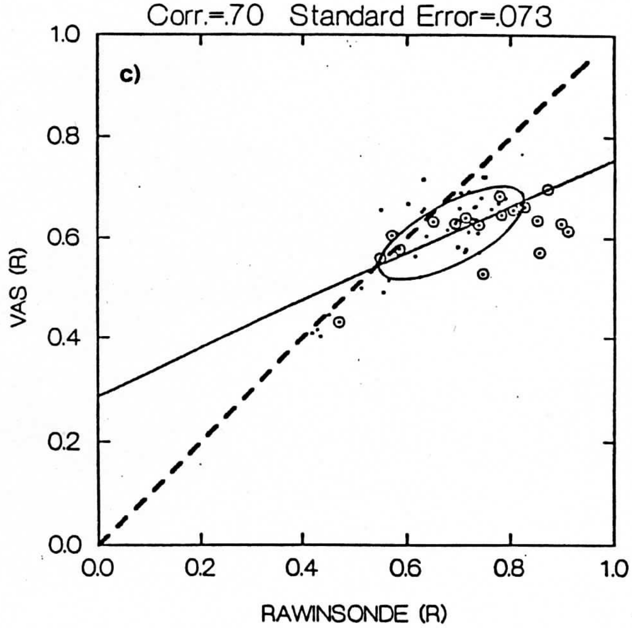

Fig. 6

DIFFERENCE from RAWINSONDE-Low Layer

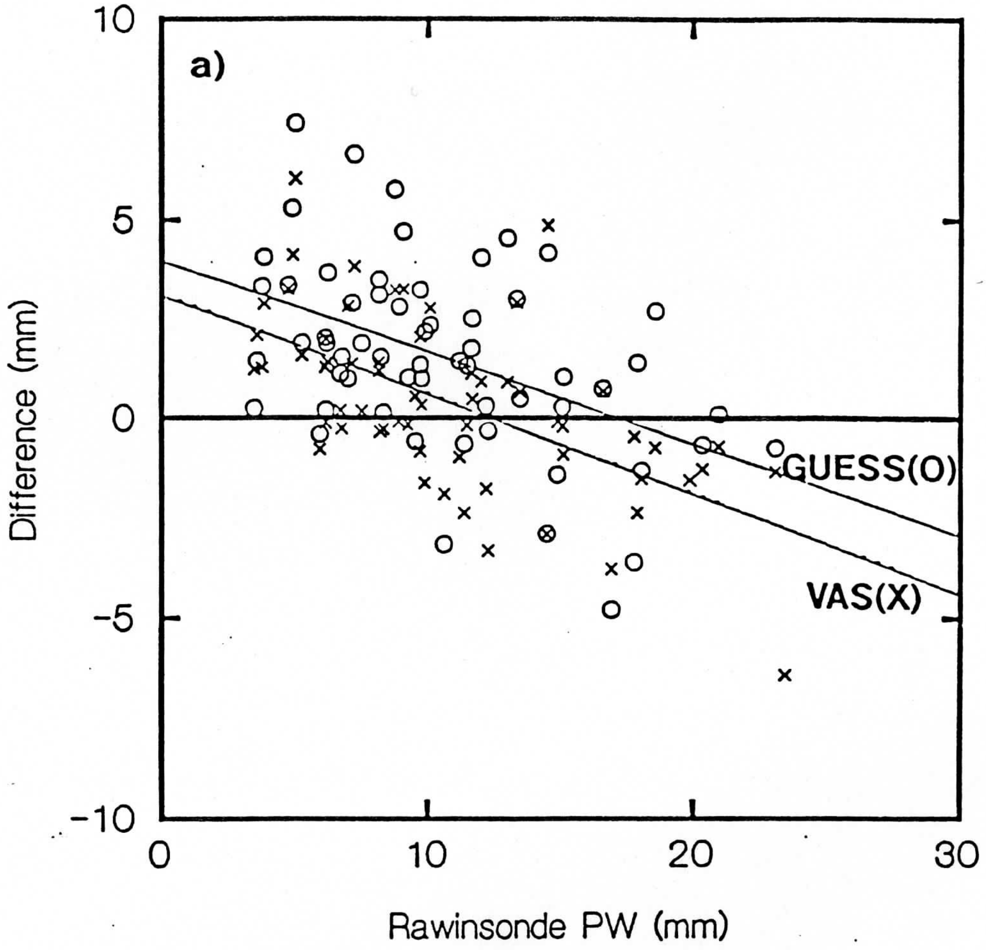

Fig. 7

DIFFERENCE from RAWINSONDE-Upper Layer

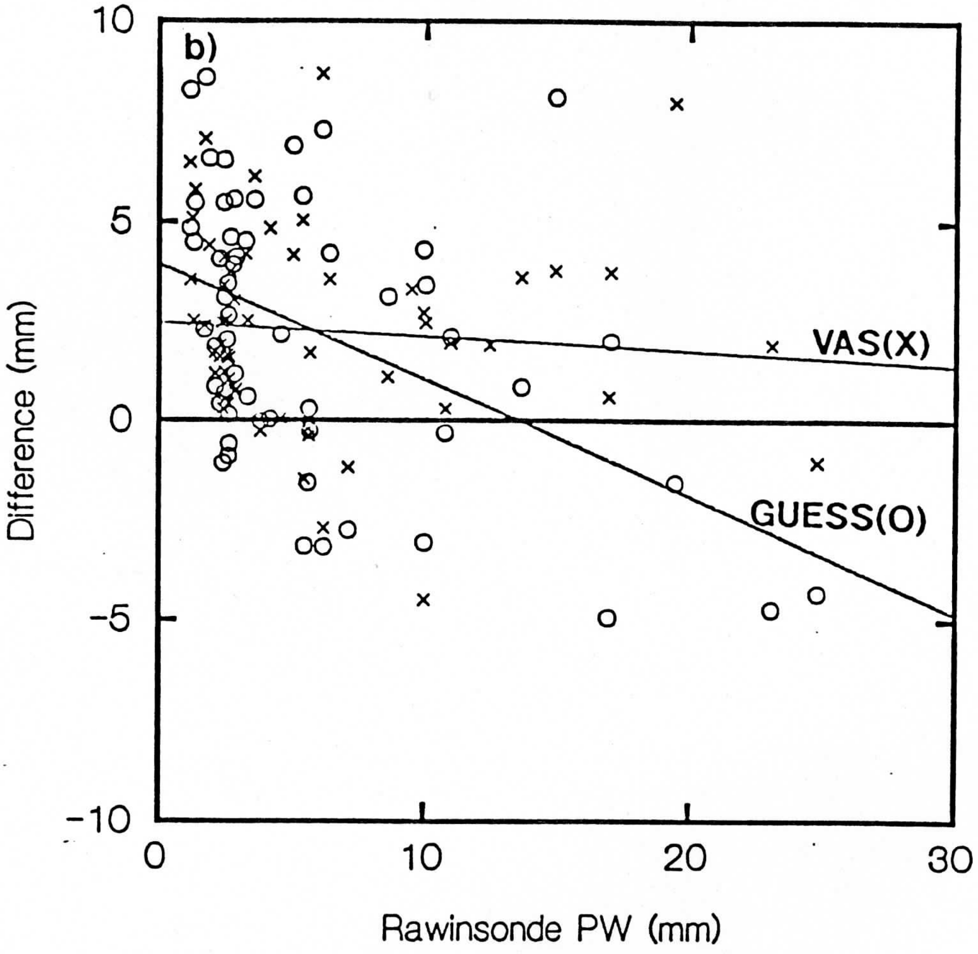

Fig. 8

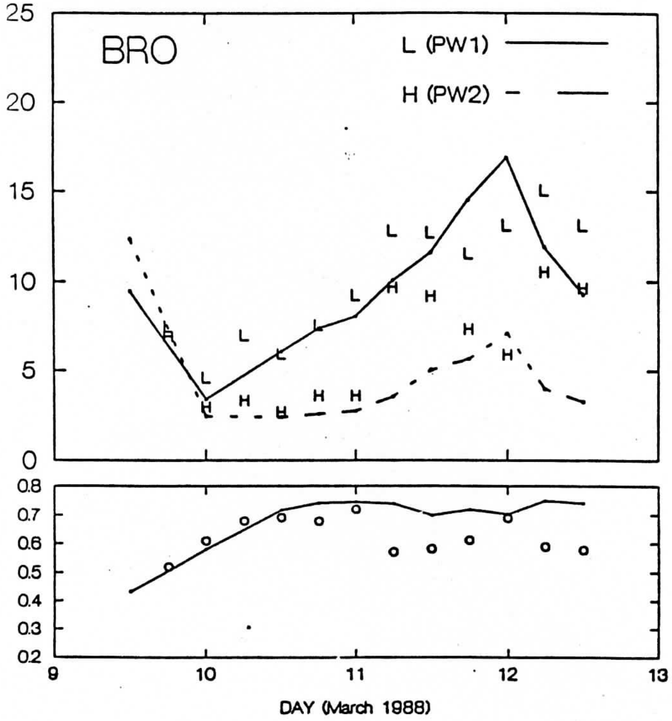

Fig. 9

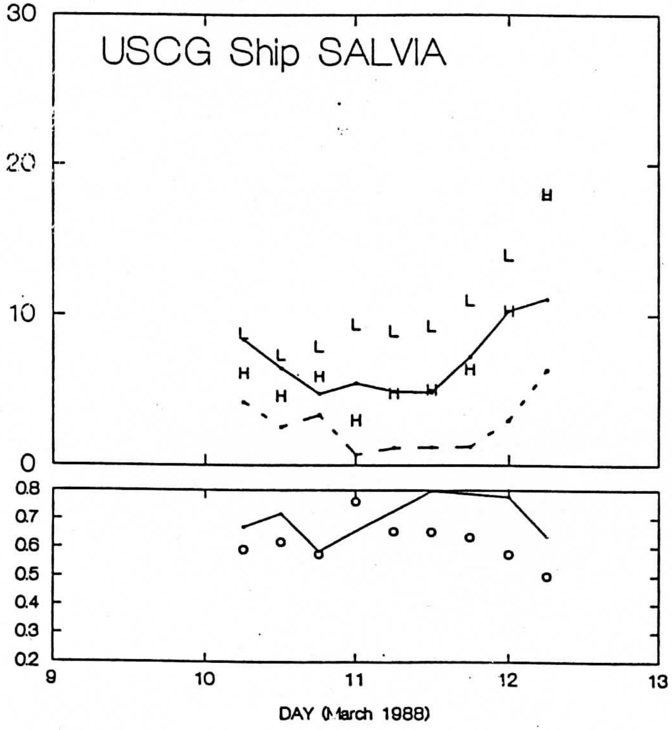

Fig. 10

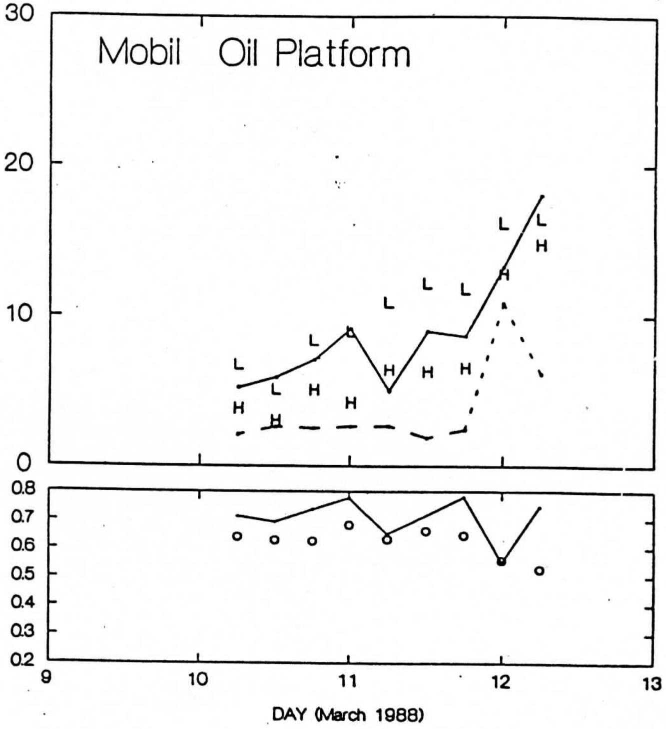

GUFMEX

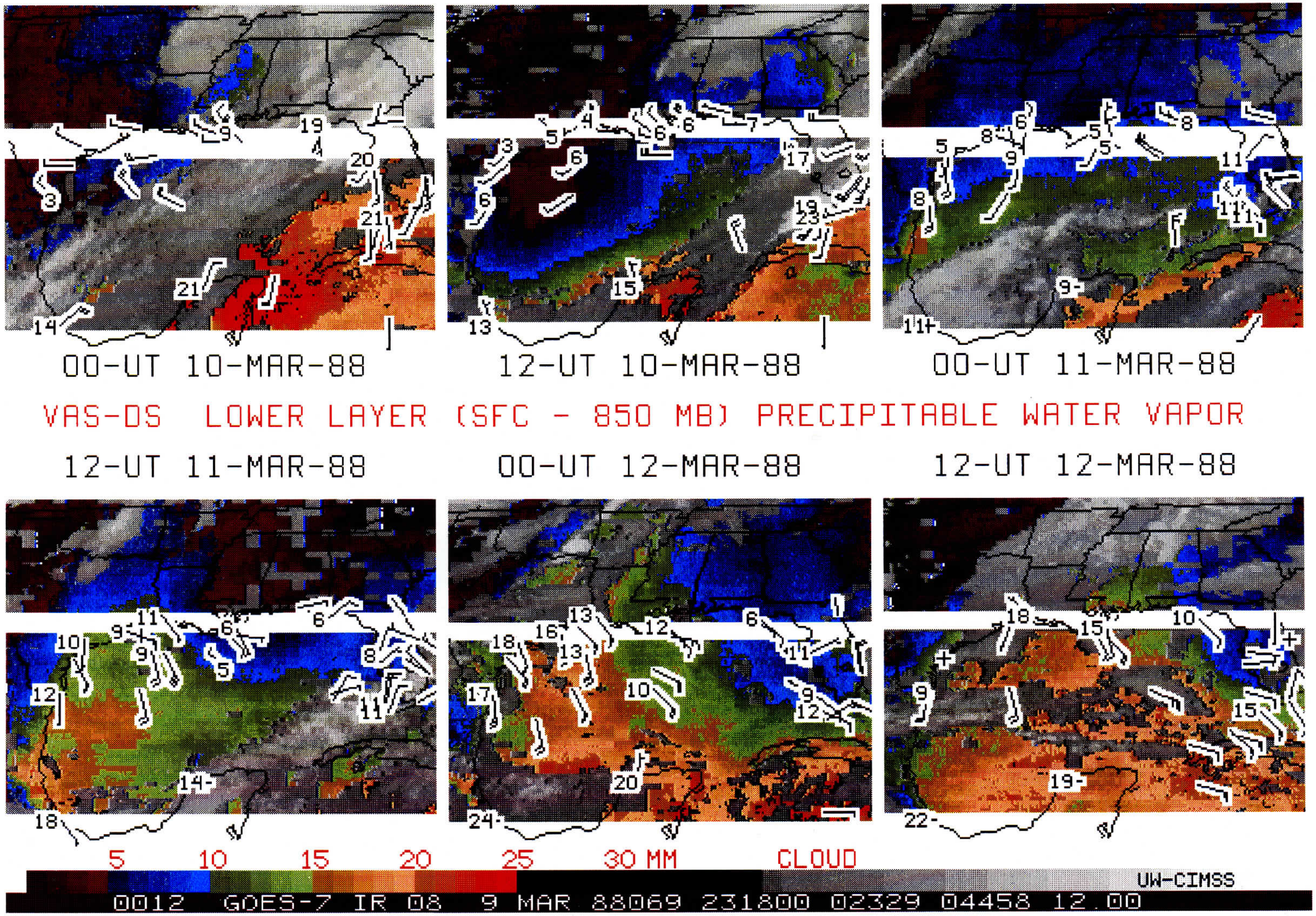

00-UT 10-MAR-88

12-UT 10-MAR-88

00-UT 11-MAR-88

VAS-DS LOWER LAYER (SFC - 850 MB) PRECIPITABLE WATER VAPOR

12-UT 11-MAR-88

00-UT 12-MAR-88

12-UT 12-MAR-88

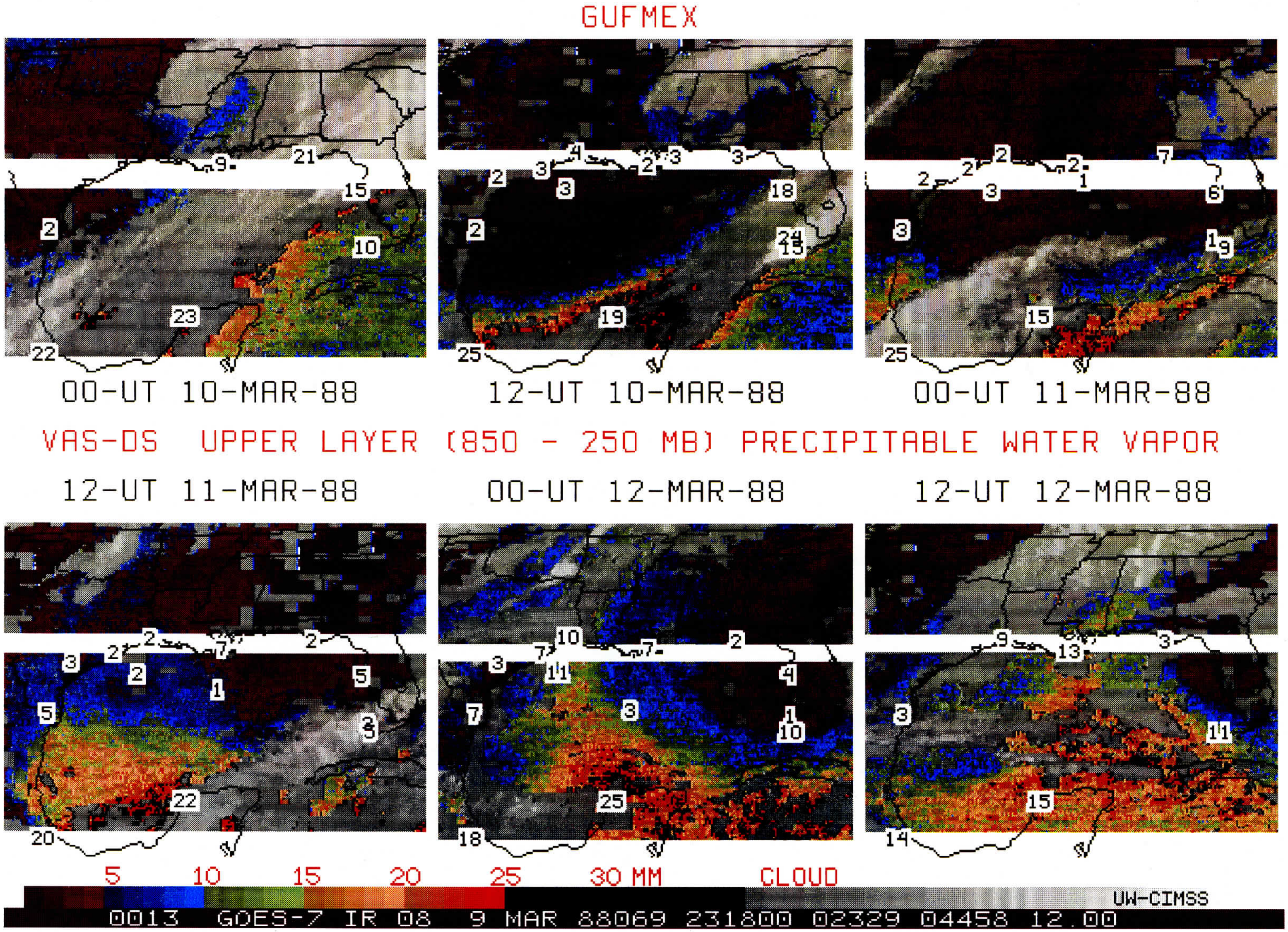

GUFMEX

00-UT 10-MAR-88

12-UT 10-MAR-88

00-UT 11-MAR-88

VAS-DS UPPER LAYER (850 - 250 MB) PRECIPITABLE WATER VAPOR

12-UT 11-MAR-88

00-UT 12-MAR-88

12-UT 12-MAR-88

D. CIMSS model assimilation. Contributed by Robert M. Aune.

The Analysis/Forecast System

The CIMSS Regional Assimilation System (CRAS) consists of three major subsystems: 1) the Analysis/Preprocessing Subsystem; 2) the Model Assimilation Subsystem; and 3) the Post processor/Visualization Subsystem. The CRAS has evolved from a long-standing collaborative effort with the analysis/forecast group of the Bureau of Meteorological Research Center, Melbourne, Australia.

Analysis/Preprocessor

The analysis is performed on a relocatable, limited area domain using a Lambert conformal map projection. The horizontal resolution is defined by the user. Typically, a grid spacing of 190 km to 40 km is used. The vertical resolution is 50 MB; twenty levels are used starting at 1000 MB. The analysis is performed using successive corrections with mass-momentum coupling provided by a variational blend of optional velocity components (gradient, geostrophic, non-divergent or real winds) with analyzed geopotential heights (Seaman, et al., 1977). Input data sets include significant and mandatory rawinsondes, hourly surface data, VAS temperature and moisture retrievals, cloud drift winds from GOES or METEOSAT, and precipitable water retrievals from SSM/I. Significant and mandatory level rawinsonde data are validated against a background guess and merged onto 50 Mb levels. Data quality assignments are made using background field checks and neighborhood checks using statistical interpolation parameters describing the variances and correlation functions of background field errors and observational errors. Analysis first-guess fields come from the NMC Global analysis or forecast, NMC RAFS analysis or forecast, or a previous model forecast. After the analysis is complete a preprocessor is run to interpolate the analyzed fields from pressure surfaces to a user specified sigma vertical coordinate. Further quality checks are made to eliminate errors introduced by the vertical interpolation. In addition to the analysis scheme described above, a scheme using optimal interpolation is currently being interfaced to CRAS.

Model/Assimilation

The forecast subsystem, known as the CIMSS Sub-Synoptic Model (SSM), consists of a state-of-the-art primitive equation model developed by Leslie, et al., 1985. The forecast is performed on the same horizontal domain as the analysis using an Arakawa C grid. Up to 20 sigma levels can be used in the vertical. The model incorporates a semi-implicit time integration scheme and a flux form of the equations. Physical parameterizations include: vertical diffusion, cumulus parameterization, large scale precipitation with evaporation, stability dependent bulk PBL with eddy diffusivities a function of bulk Richardson number, and a surface heat budget with a prognostic equation for surface temperature. Initial imbalances in the initial fields are reduced using a vertical normal mode initialization (Bourke and McGregor, 1983).

The assimilation of observations in the model is currently being handled by a Newtonian nudging module. Asynoptic data are first objectively analyzed to a model forecast data set. The model is then restarted at a previous time and the fields are then nudged toward the new data set. In addition a number of post-analysis adjustment schemes have been designed to allow the model to use asynoptic satellite data directly in the model. One such scheme, a 1D mixing ratio profile vertical adjustment scheme using precipitable water retrievals from VAS has been used with some success.

A number of modifications/enhancements are either currently being added to or are being considered for the CRAS. These include: enhanced cumulus parameterization, explicit cloud water, and various approaches allowing for the assimilation of asynoptic data.

Post processor/Visualization

A comprehensive post processor has been developed to produce diagnostic fields on pressure, height, and sigma surfaces from the model forecast data sets. Model output fields and post processed fields can be viewed using PC/DOS and UNIX/RISC software packages developed at CIMSS. The PC/DOS package known as SSM Field Utility (SFU) can produce field plots, data overlays, skewt plots, profile plots, and cross sections. The UNIX/RISC based package, known as XSFU, can perform all the tasks of SFU along with the addition of 2D animation.

CRAS has also been interfaced to VIS-5D (Visualization of 5-Dimensional Data sets), a software system that allows a user to interactively explore 4-dimensional gridded data sets. VIS-5D is currently under development at the Space Science and Engineering Center (SSEC) at the University of Wisconsin as a subsystem of the Man/computer Interactive Data Access System (McIDAS). It runs on a Stardent model ST2000 workstation and can generate 3-D animated graphics in real time. The software accepts 3-D gridded data of the type generated by most numerical weather prediction models. These data are loaded, preprocessed, and then displayed as a 3-D time sequence. Field selection and configuration remain under the control of the user through a mouse driven menu while the time sequence is looping. The power and flexibility of the system allows scientists to produce and direct animation using their own data sets with amazing ease. VIS-5D is currently being used at CIMSS to test new physical parameterizations and to study the impact of 4-D data assimilation on numerical forecasts. A video recording capability is also available. A more detailed description of VIS-5D is given by Hibbard and Santek (1990).

Computer System

The CRAS is currently running on an IBM Series 6000 RISC computer Model 550. The system has 128 megabytes of real memory, 256 megabytes of virtual memory, and runs under UNIX. The processor performs at speeds up to 22 megaflops. Approximately 3.5 gigabytes of disk space is available to the system. Data are transferred to and from the system via ETHERNET. This system has increased the throughput of CRAS by a factor of five over the IBM 4381 used previously. In addition, up to four forecast runs can be executed simultaneously making the system ideal for data assimilation impact studies.

Real-time Forecasts for STORM-FEST

A major goal of the Assimilation Group at CIMSS is to be able to run the CRAS in real-time, producing control forecasts and assimilation forecasts simultaneously to assess the impact of various data sources, in particular, remotely sensed data from satellites. The recent acquisition of two IBM Series 6000 RISC workstations has provided the computational power to accomplish such a task. To test the feasibility of producing real-time forecasts the CRAS was configured to provide forecasting support for CIMSS during STORM-FEST. A grid of 75 by 63 with 20 sigma levels in the vertical was selected to provide coverage for all of continental US. A depiction of the forecast grid is shown in Fig 1. NMC's NGM analysis was used as the initial guess for the analysis. NMC's Aviation forecast provided the 12 hr, 24 hr, and 36 hr forecast boundary conditions. These data sets were received from the McIDAS via ETHERNET at scheduled intervals. The CRAS was then executed on the RISC workstation after the data were received. The system was tested for a period of three days and provided reasonable forecasts in a timely manner. Permanent implementation of the system is expected to commence on 01 February, 1992, in time for STORM-FEST.

Recent impact studies using the CRAS have been performed. Two such studies are briefly described.

Impact of VAS Precipitable Water Retrievals on a Numerical simulation of Return Flow in the Gulf of Mexico

Introduction

During February and March of 1988, comprehensive data sets were collected in the Gulf of Mexico. The Gulf of Mexico Experiment (GUFMEX) was conducted to examine two phenomena in the Gulf: (1) Air mass modification over the loop current, and (2) the origin and characteristics of the return flow that follows a cold-air outbreak over the Gulf. A complete overview of

GUFMEX is presented by Lewis et al. (1989). Data sets from GUFMEX could be used to identify any impact VAS retrievals might have on a numerical simulation of a return flow event.

A study was conducted at CIMSS to determine if VAS precipitable water retrievals can be used to enhance a three-dimensional analysis of moisture in the Gulf and can have a positive impact on a numerical simulation of return flow. VAS precipitable water observations were inserted into a numerical simulation of the 9 - 12 March, 1988 GUFMEX case. Data were inserted at 12 hour intervals using an analytical approach that combines the high resolution horizontal gradients of precipitable water as observed by VAS with the detailed mixing ratio profiles produced by the forecast model.

Assimilation Technique

Studies have shown that temperature and moisture profiles derived from VAS radiances can have a positive impact on an analysis of the preconvective environment. Mostek et al. (1986) demonstrated a positive impact when using VAS retrievals to enhance the conventional observing network in an analysis of one case over the central United States. Their results were particularly promising when vertically integrated quantities were analyzed, such as precipitable water, mainly because such a parameter is physically representative of how the instrument senses. To overcome the limited vertical resolution of the VAS, Gal-Chen (1983) proposed using a calculus of variations approach that would assimilate vertically integrated quantities, such as thickness and precipitable water from geostationary satellites into mesoscale numerical models. The advantage of this technique is that it allows for the insertion of timely satellite information with high horizontal resolution, while simultaneously preserving the vertical profiles of temperature and moisture predicted by a numerical model. Gal-Chen et al. (1986), and more recently Aune et al. (1987), have obtained favorable results using similar forms of this technique to assimilate VAS thickness data into a mesoscale model without moisture. By using a dry model, i.e. no predictive equation for moisture, no moist physics, etc., they were able to clearly trace the impact of the VAS data throughout their simulations. The impact would have been less obvious with moist processes present.

A scheme was derived to analytically adjust model mixing ratio profiles to reflect precipitable water retrievals from VAS. The vertical distribution of differential mixing ratios was constrained to the preadjusted mixing ratio profile of the model. In other words, where VAS precipitable water retrievals show an increase over the predicted model value, mixing ratio adjustments are added to the model profile, with moist layers receiving proportionally more adjustment than dry layers. This approach has three advantages: 1) The adjusted moisture profile reflects the precipitable water observation exactly; 2) it inherently inserts more moisture in the lower levels and reduces the chances of accidentally saturating a layer which would contradict the presence of a cloud free VAS retrieval at that location; and 3) it is simple and economical. If an adjustment forces a layer to saturation, mixing ratios are iteratively redistributed to adjacent layers below until a clear air criteria is met. This scheme was tested on hundreds of mixing ratio profiles taken from the 20 July, 1981 case used by Aune et al. (1987). Two significant shortcomings emerged: 1) changes in the mixing ratio lapse rates, or thermodynamic stability, resulting from a mixing ratio adjustment are not systematically minimized; and 2) horizontal gradient information from the VAS precipitable water retrievals are not directly incorporated. In spite of these drawbacks the technique was able to show some skill.

The technique is summarized as follows: 1) The precipitable water retrievals from VAS are analyzed to the model forecast grid; 2) VAS precipitable water analysis is then compared to the model forecasted precipitable water. Where differences occur, analytically adjust the collocated moisture profile of the model to reflect the VAS observations; 3) The resulting three dimensional precipitable water field is then converted back to mixing ratios and inserted into the forecast model which is then restarted. Time integration continues until the next VAS retrieval is available and the cycle is then repeated.

Experiment Design

A sequence of VAS/NOVAS simulations were conducted to determine if VAS total precipitable water retrievals can be used to enhance a three-dimensional analysis of moisture in the Gulf and if this analysis can have a positive impact on a numerical simulation of a moist return flow. The CRAS was used to produce a series of data/no data simulations of the 9 - 12 March case. The experiment design is as follows: 1) Generate a 72 hr fine mesh (75 km) Control Forecast commencing 09 March 88, 12 UT with rawinsonde insert every 12 hours. Full physics, no VAS data; 2) Repeat Step 1 with RAOB+VAS insert every 12 hours; 3) Compare simulations to determine impact of VAS retrievals. Verify model forecasted moisture profiles against rawinsondes. A 72 hr coarse mesh (190 km) forecast commencing 9 March 88, 12 UT was generated to produce a 6 hourly boundary condition data set for the fine mesh. NMC Global Spectral Model analyses were used as initial conditions and time dependent boundary conditions. Sixteen sigma coordinate levels were used in the vertical. VAS retrievals used to generate the derived product imagery for the study were provided by Hayden and Schreiner (1989).

Results

The VAS precipitable water data were digitized directly from the derived product image (Rabin, et al., 1992) for analysis onto the model grid. Figure 1 shows the resulting VAS precipitable water analysis (mm) at the first VAS insertion time, 00 UT, 10 March 88. Here the prior 12 hr model forecast was used as the guess field. Both RAWInsondes and VAS precipitable water retrievals were used in the analysis. Clouds from the corresponding GOES IR image (not shown) were overlaid to mask where VAS retrievals were not possible. Figure 2 depicts the difference field of total precipitable water (mm), VAS minus NOVAS analysis. The area of zero differences running southwest to northeast across the Gulf is due to a frontal cloud band associated with a low system in the Carolinas, where no retrievals were derived. As a result of VAS a significant reduction in the total precipitable water occurred in the clear air behind the frontal band, whereas an increase in precipitable water occurred over Mississippi. As expected differences over areas with RAWINSONDE coverage are generally smaller than over data sparse areas. The corresponding change in the moisture profile due to the VAS insert at the location depicted with a dot in Fig. 2 is shown in Fig. 3. Significant drying has occurred as a result of the adjustment (heavy dashed line), however, the dew point lapse rate has changed very little.

After the VAS insert at 00 UT 10 March 88, the model was restarted and a 12 hr forecast was generated. Figure 4 shows mixing ratio (g/kg) differences (VAS minus NOVAS) after 12 hours of integration at the lowest model sigma level. The impact of the VAS precipitable water insertion at 00 UT 10 March is still evident. The area of maximum differences south of Louisiana appears to have advected eastward which is consistent with the predicted low-level wind flow in the area (not shown). The location of the cross section is shown in Fig. 4. For this 12 hour assimilation period the VAS insert has significantly altered the predicted three dimensional distribution of moisture over the Gulf.

Now that impact has been established, the next step is to repeat the assimilation cycle for the next four assimilation periods and verify predicted moisture profiles from the model against RAWInsondes. Figure 5 shows the predicted mixing ratio profile at Brownsville, TX valid at 00 UT 12 March 88 from the Control forecast, the VAS forecast, and the observed RAWINSONDE. The assimilation of VAS data in the forecast has improved the forecasted moisture profile at this location.

Satellite Derived Winds Experiment

Introduction

Satellite Measured Winds (SMW) are derived from time sequenced geostationary imagery using pattern recognition techniques. Recently, an automated technique for obtaining upper level SMW's has been developed at CIMSS (Merrill et al., 1991). SMW's are computed and are quality controlled based on an algorithm developed by Hayden and Velden, 1991.

Assimilation Technique

As a first attempt SMW's were incorporated directly into the Analysis Subsystem of CRAS. SMW's were given the same treatment as rawinsonde winds in the analysis. In an effort to preserve the SMW information and reduce mass-momentum imbalances in the model, two additional techniques were applied. First, the 3D variational blending of wind observations to the analyzed geopotential height fields used in the Analysis Subsystem was applied to SMW's only and not to the rawinsonde winds. This helped to isolate the impact of SMW's in areas where no mass information was available. Second, Newtonian nudging was used in addition to the variational blend to further balance the mass field with the SMW's.

Experiment Design

Four forecasts were made using the initial conditions of NMC's aviation forecast on 24 April, 1990 at 00 UT. The initial analysis was followed by a 12 hr forecast, an analysis at 24 April, 12 UT, and finally, another 12 hr forecast. A Control forecast was generated using only rawinsondes. Three additional experiments were conducted with rawinsondes/SMW's, rawinsondes/SMW's/Blending, and rawinsondes/SMW's/Blending/Nudging. Each forecast was then compared to the control to determine impact.

Results

As expected the forecast incorporating rawinsondes, SMW's, blending, and nudging produced the strongest impact. Figure 6 shows the forecast error of 250 MB isotachs of the Control compared to the analysis at 00 UT, 25 April, 90. Figure 7 is the same as Fig 6 except it shows the forecast error of the SMW run. The SMW's have had a positive impact in general. The domain rms error for the control is 4.4 m/s, for the SMW forecast, 3.9 m/s. Both forecasts have a huge error at 250 Mb for the jet along the west coast of the US, but the maximum error for the SMW forecast was about 5 knots less. An error of 10 knots over Texas was removed by the SMW's. The 20 knot difference for the Control in the subtropical jet southwest of Baja has been reduced to 10 knots. Since there are no rawinsondes in this area this result should probably be construed as consistency in the SMW rather than an error reduction. Figure 8 shows the forecasted isotach field at 250 Mb valid for 00 UT, 25 April, 90. The SMW's for the same time are superimposed. The difference in isotachs between the SMW forecast and the Control are shown in Fig 9, along with the SMW's from 00 UT 24 April, 90 superimposed. The differences are small, rarely more than 10 knots. Larger differences were not realized in the tropics were SMW's are plentiful, probably because the geopotential blend is not performed south of 15N.

List of Figures

Fig. 1. Total precipitable water analysis (mm) valid 00 UT 10 March 88 derived from 12 hr model forecast of mixing ratios, rawinsondes and VAS retrievals.

Fig. 2. Difference of total precipitable water analysis (mm), Figure 1 minus same analysis without VAS retrievals.

Fig. 3. Profile of forecasted dew points (C). Light dashed, before adjustment; Heavy dashed, after adjustment. Temperature remains unchanged. Location of profile is depicted as dot in Figure 2.

Fig. 4. Change in the 12 hr forecasted, lowest model level mixing ratio resulting from the VAS precipitable water insert at 00 UT 10 March 88. Line represents location of cross section in Figure 6.

Fig. 5. Profiles of temperature and dew point from A) a 12 hr Control forecast valid at 00 UT 12 March 88, B) same as A except from the NOVAS Experiment, and C) the same as A except from the VAS Experiment.

Fig. 6. Isotach errors (knots), Control forecast minus analysis, valid 00 UT 25 April 90.

Fig. 7. Isotach errors (knots), SMW forecast minus analysis, valid 00 UT 25 April 90.

Fig. 8. SMW forecast isotachs valid 00 UT April 90. SMW's at the valid time are superimposed.

Fig. 9. Isotach differences, SMW forecast minus the Control valid 00 UT April 90. SMW's form 24 hours earlier are superimposed.

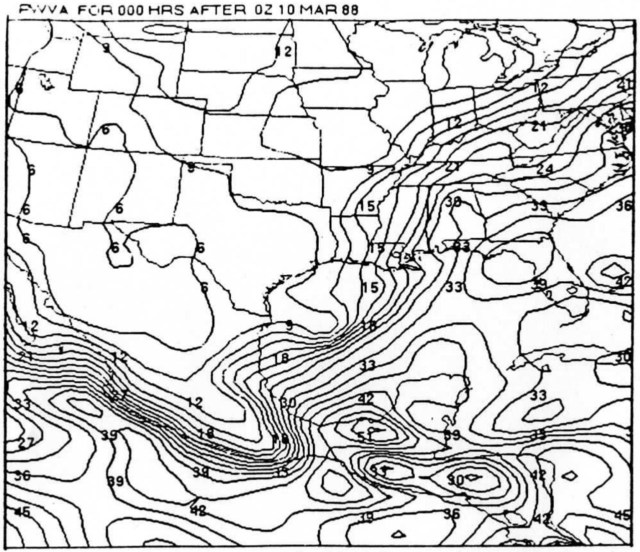

Fig. 1. Total precipitable water analysis (mm) valid 00 UTC 10 March 88 derived from 12 hr model forecast of mixing ratios, RAOBS and VAS retrievals.

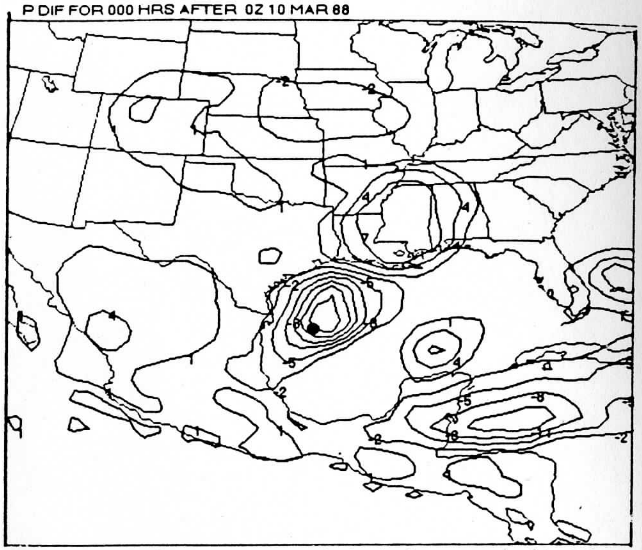

Fig. 2. Difference of total precipitable water analysis (mm), Figure 1 minus same analysis without VAS retrievals.

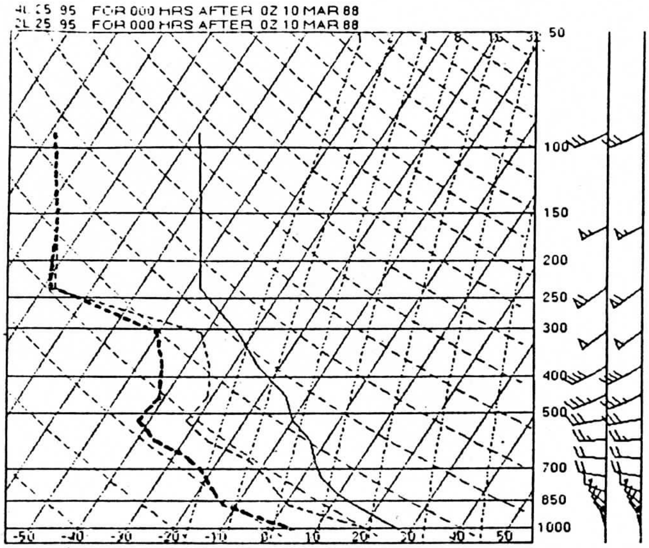

Fig. 3. Profile of model generated dewpoints (C). Light dashed, before adjustment; Heavy dashed, after adjustment. Temperature remains unchanged. Location of profile is depicted as dot in Figure 2.

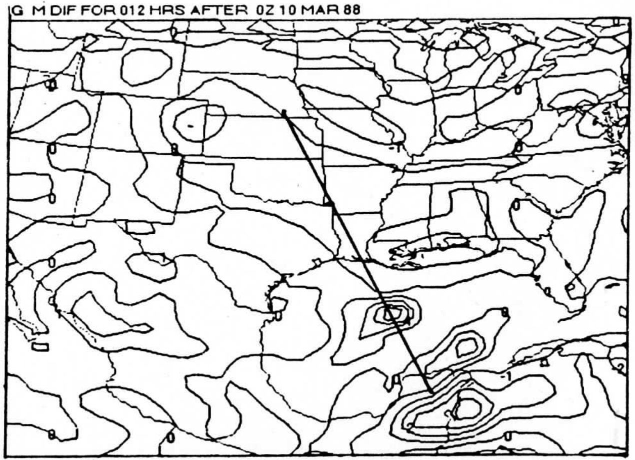

Fig. 4 Change in the 12 hr forecasted, lowest model level mixing ratio resulting from the VAS precipitable water insert at 00 UTC 10 March 88.

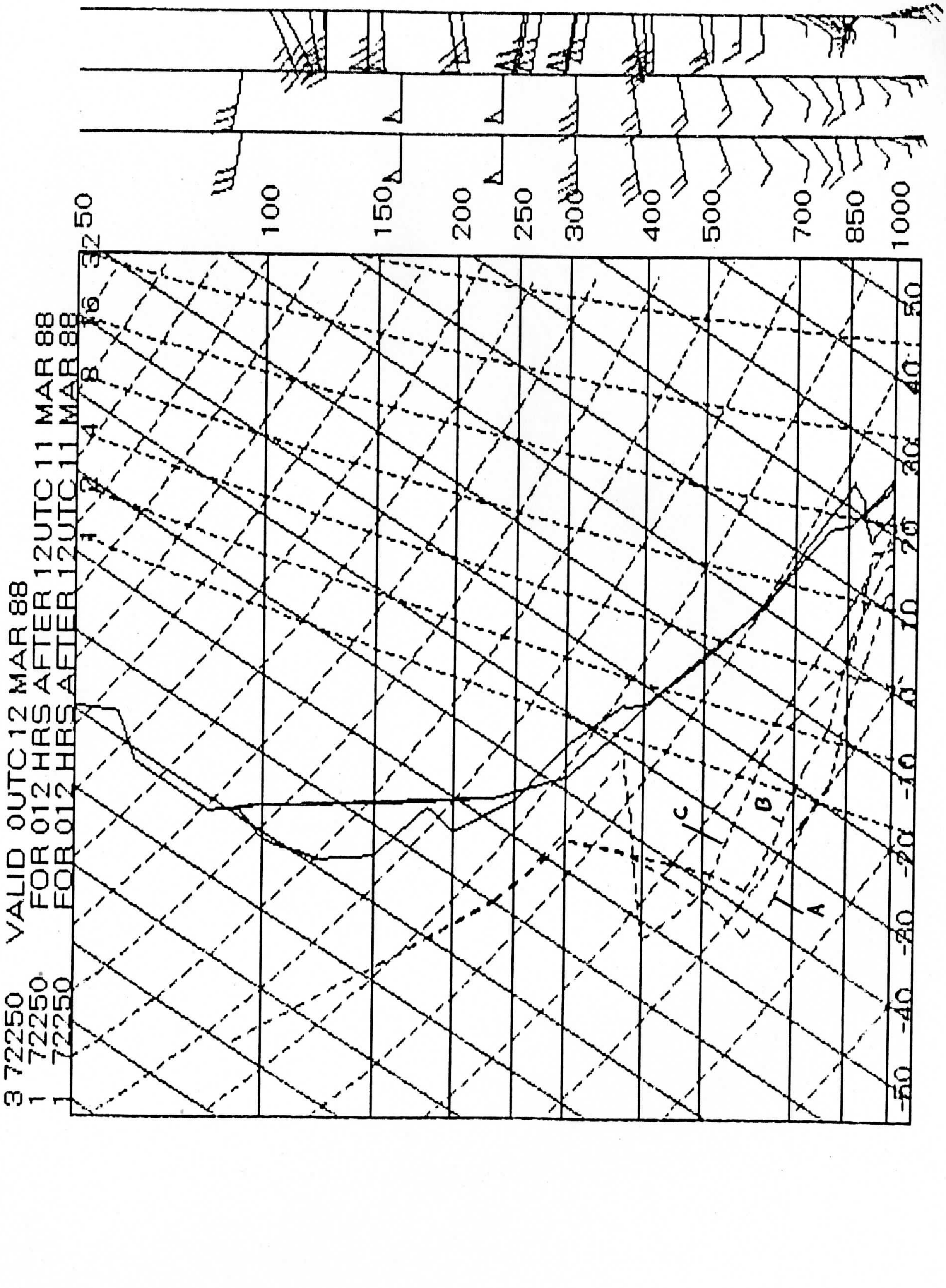
3 72250 VALID 0UTC 12 MAR 88
1 72250 FOR 012 HRS AFTER 12UTC 11 MAR 88
1 72250 FOR 012 HRS AFTER 12UTC 11 MAR 88
1
2
4
8
16
32
50
100
150
200
250
300
400
500
700
850
1000
-50
-40
-30
-20
-10
0
10
20
30
40
50
A
B
C

Figure 5

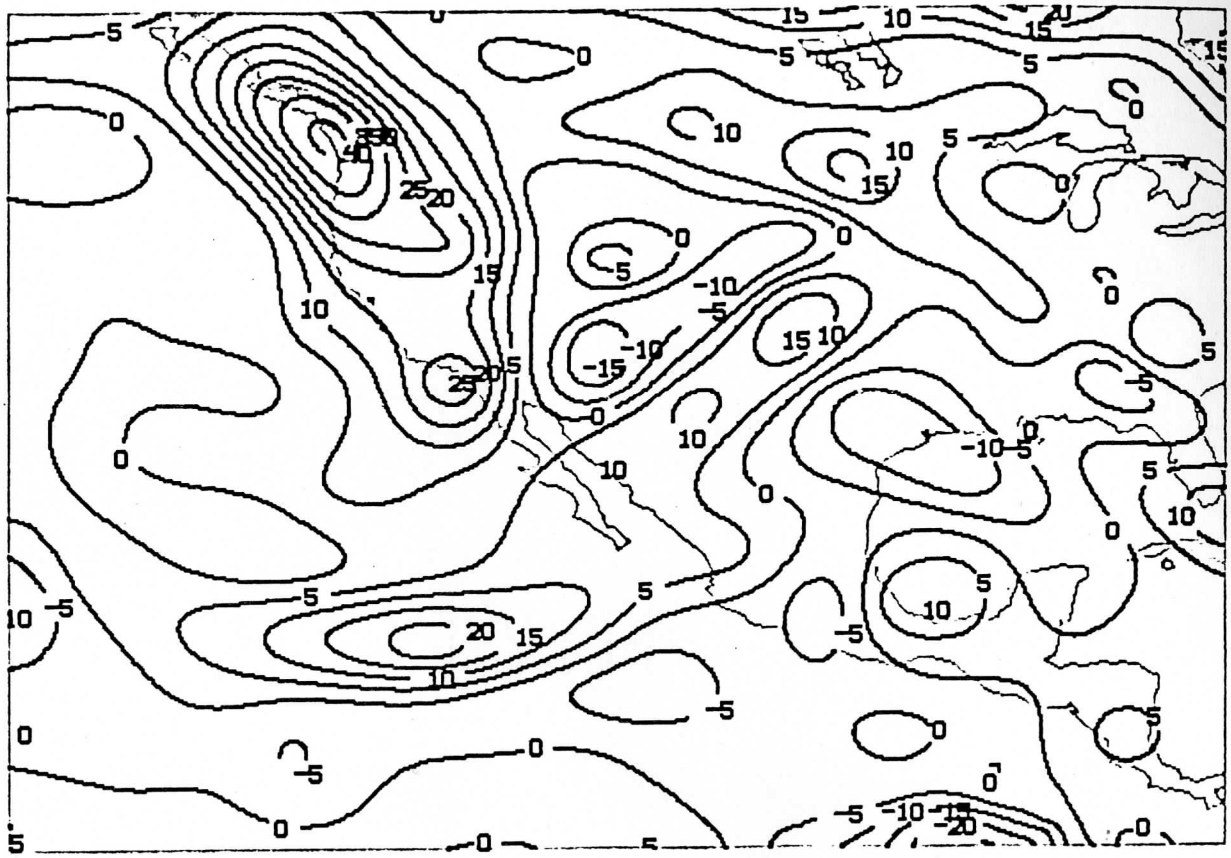

APRIL 25 90 00UT 250MB ISOTACH ANALYSIS-CONTROL FORECAST (KNOTS)

Figure 6

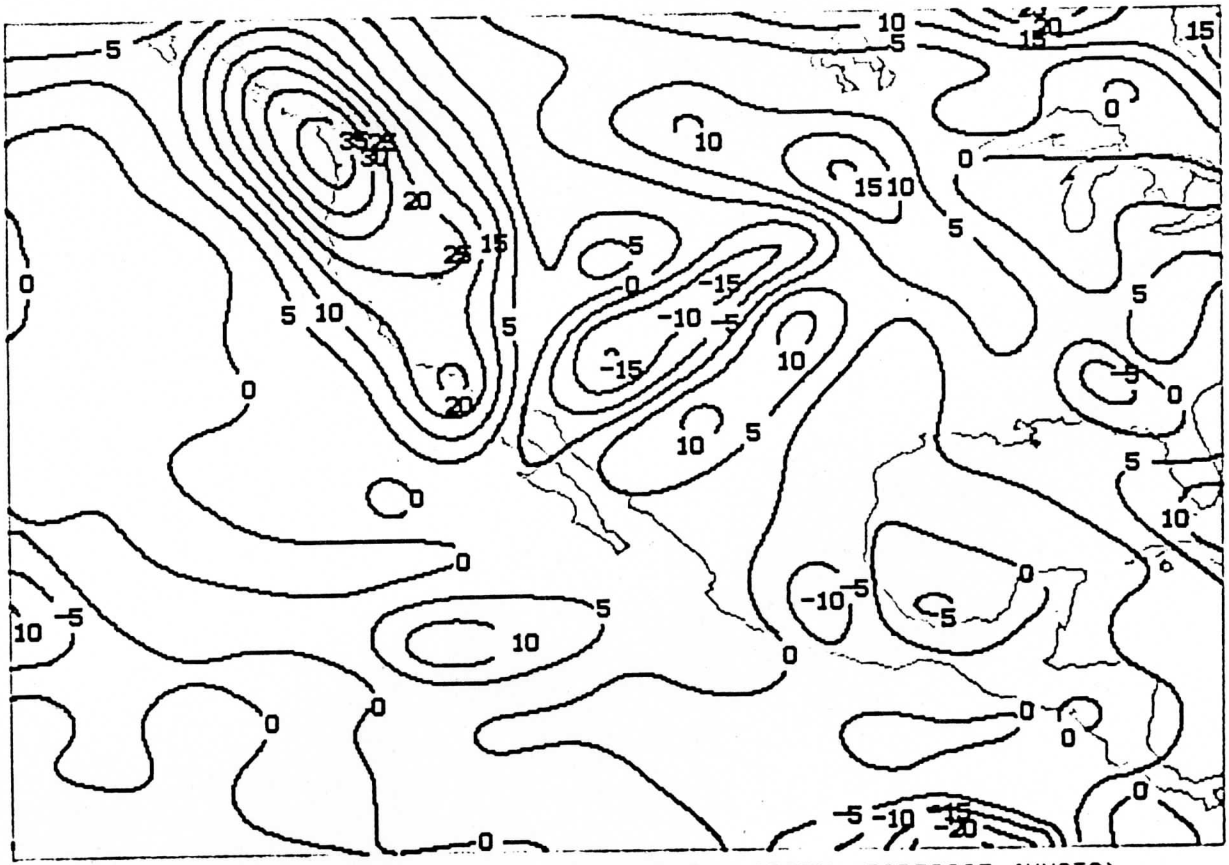

APRIL 25 90 00UT 250MB ISOTACH ANALYSIS-SMW ASSIM. FORECAST (KNOTS)

Figure 7

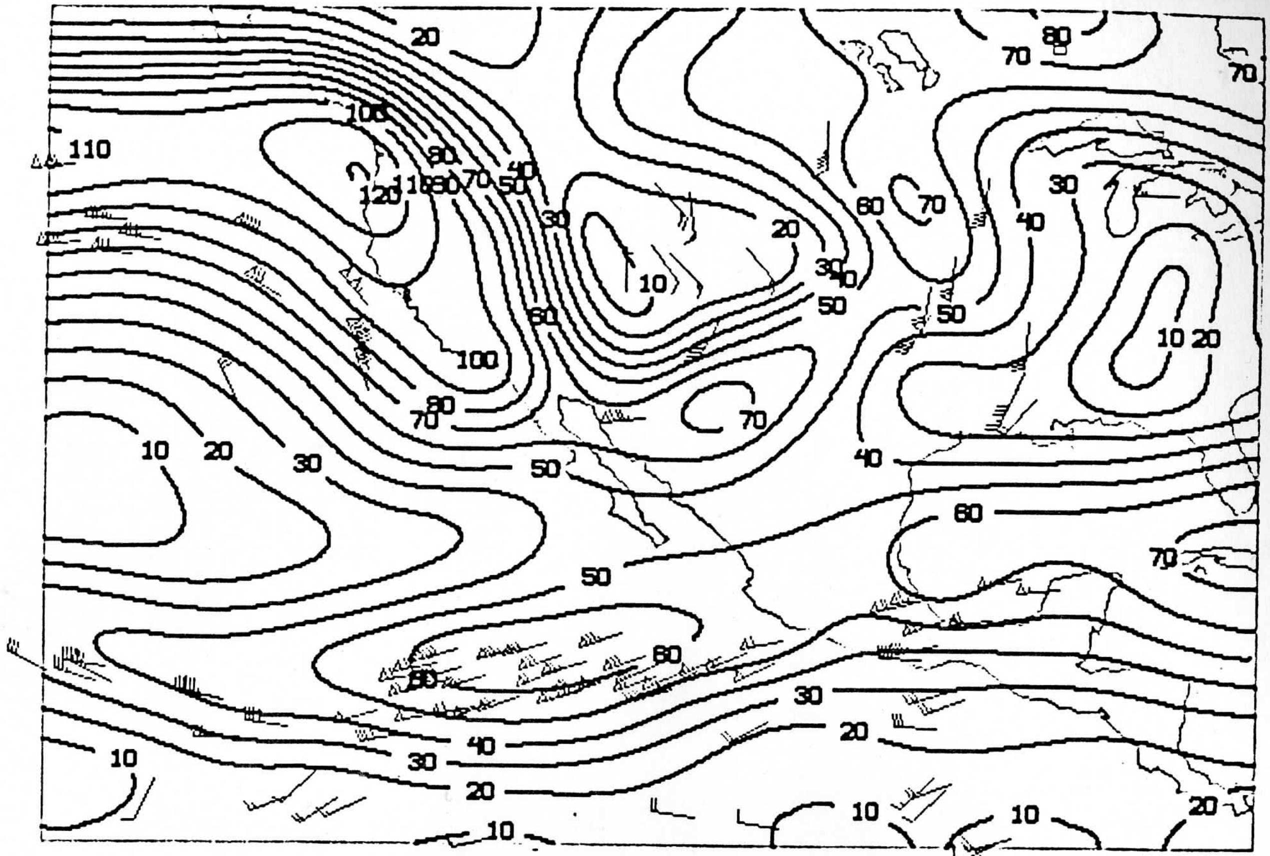

APRIL 25 90 00UT 250MB ISOTACH ANALYSIS (RAOB+SMW); SMW FOR 4/25/00

Figure 8

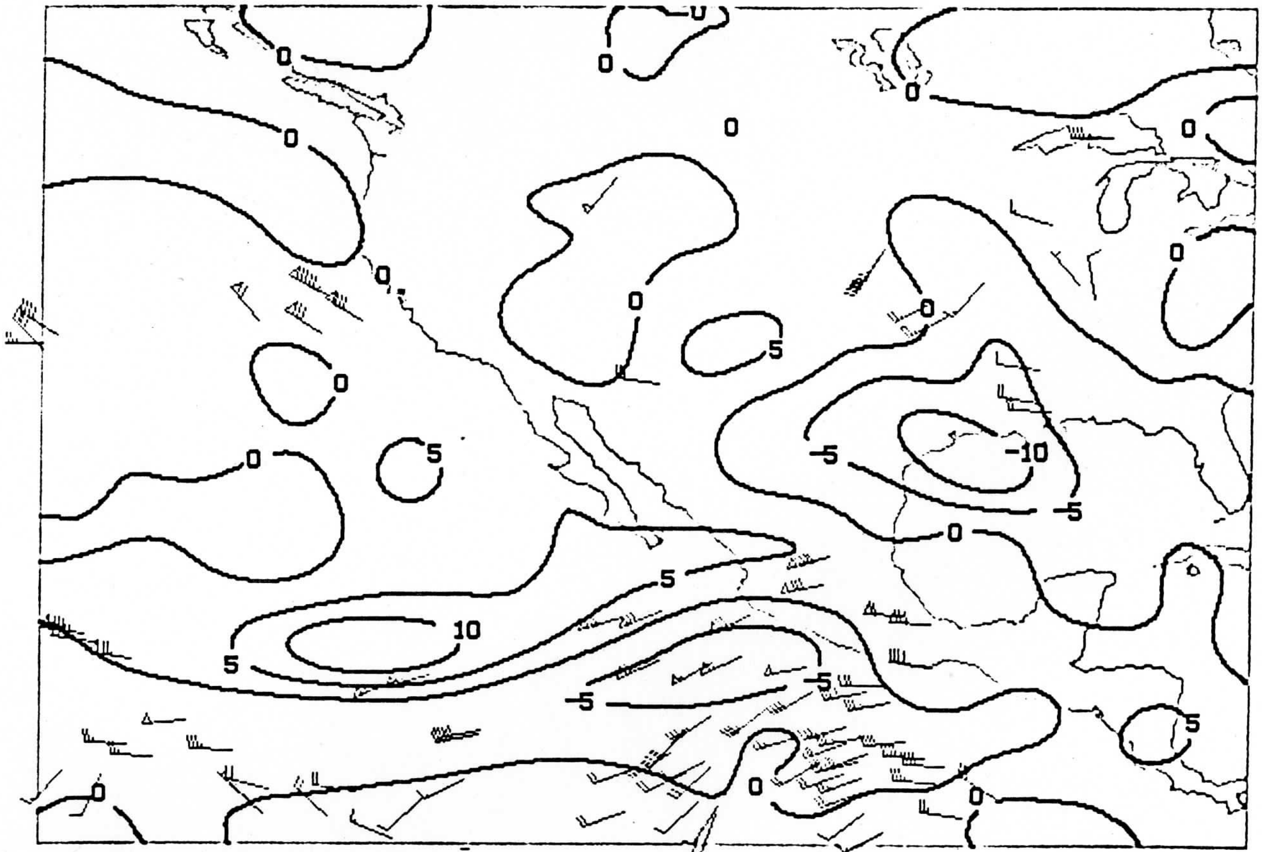

250 MB WIN ANOMALY (SMW-CNT) FCST 4/25 00; SMW FOR 4/24 00

Figure 9

E. Data assimilation of diabatic heating. Contributed by Xiaohua Wu.

This report summarizes work completed on numerical processing of diabatic initialization and cloud water initial specification on the CRAS during this year. The model used in this study is the CRAS with 80 km horizontal resolution and 16 σ levels. The report includes three sections. A brief description of the diabatic initialization procedure and tests of its impact to forecast are given in section 1. The cloud water initialization and its impact on the forecast are presented in section 2. Section 3 summarizes and discusses future work.

1. Diabatic initialization and its impact to forecast

The purpose of diabatic initialization is to incorporate diabatic heat release due to convection and large-scale condensation into the vertical mode initialization (VMI) procedure of the CRAS. The effect is to derive an initial divergence field consistent with these "heating sources". The diabatic initialization is static, and applied only during the iterations of the VMI. The balance conditions used in diabatic VMI are

$$(f_0\tau^{-1} - \nabla^2)\Delta\zeta = -f_0\tau^{-1}\frac{\partial\delta}{\partial t} \qquad (1)$$

$$(f_0\tau^{-1} - \nabla^2)\Delta\delta = t^{-1}\left[f_0\frac{\partial\zeta}{\partial t} - \nabla^2\left(\frac{\partial h}{\partial t}\right)_a - \nabla^2\dot{Q}\right] \qquad (2)$$

$$\Delta h = \tau f_0^{-1}\Delta\zeta \qquad (3)$$

where τ is a linear integral sigma coordinate operator, ζ is the vertical component of relative vorticity, δ is divergence on sigma surfaces, ∇^2 is the Laplacian operator on the SSM Lambert conformal grid, and h is called pseudo-geopotential which is a linear combination of the hydrostatic geopotential and $\ln(s(P_s-P_t)+P_t)$, subscript a indicates adiabatic tendency, $\dot{Q}$ represents all the diabatic terms.

The estimate of diabatic heating release, $\dot{Q}$, is obtained by time averaging the latent heat release from convective and large-scale condensation during a three hour forecast starting from an uninitialized analysis. These model produced latent heating rates are then incorporated in the VMI procedure as a forcing term. For assuring numerical stability of the VMI, this forcing term is kept unchanged during the iteration process so there is no interaction between the forcing and the iteration.

The impacts of diabatic initialization for model forecast are considered from two aspects:

--- the control of noise

--- the spin-up problem

Noise control

Fig. 1 shows the evolution of surface pressure during a 12 hour forecast started from an uninitialized (dash-dotted line), an adiabatic initialized (full line) and a diabatic initialized (dashed line) analysis for a grid point in a rainfall area. The initial fields used for these initialization are obtained from an analysis of RAWINSONDE data (3/13/91, 00Z) using the NMC global model analysis as background to the SSM grids. The uninitialized forecast shows high frequency noise for the first 6 hours of one forecast, evidenced by unrealistic surface pressure variations. Both adiabatic and diabatic initialized forecasts predict the slow changes in pressure without the high frequency oscillations.

The spin-up problem

To test the impacts of diabatic initialization for the "spin-up" problem, the adiabatic and diabatic initializations with different modes are compared to a "control run". For the control run, a 24-h forecast is initialized at t=-12h (3/12/91, 12Z) with adiabatic initialization. Test runs begin at t=0hr (3/13/91 00Z, with a large-area precipitation in the model forecast domain) and end at t=12hr (3/13/91 12Z). A 12-h spin-up (t=-12h to t=0hr) allows the control experiment to achieve dynamic balance, and thus develop important mesoscale features of realistic cloud water and rain water distribution which can be used for initialization of the test runs. The second twelve hours of the control run are used to evaluate the test forecasts.

Fig. 2 and Fig. 3 show the hourly grid-scale rainfall integrated over the whole forecast domain for the test forecast (t=0hr to t=12hr). Comparing to the precipitation of control run (thick solid line), it is shown that the spin-up problem is more severe as the modes increase in adiabatic initialization (Fig. 2). Fig. 3 shows that the performance of diabatic initialization with first two modes is almost same to that of adiabatic one. However, diabatic initialization with three and four modes does not show additional degradation as in the adiabatic case (Fig. 3).

Fig. 4 is the first two hours of precipitation forecasted by control run. Fig. 5 shows the difference in the diabatically initialized w field and adiabatically initialized ω field (at σ=0.7, p$\approx$ 500 MB level) with 3 modes. Comparing Fig. 4 and Fig. 5, the pattern of $\Delta\ \omega$ between two initialization procedures for 3 modes is consistent with the precipitation (latent heat release) distribution. This analysis implies that the lack of diabatic heating in adiabatic initialization is a main cause of the "spin-up" problem. The difference in w for 4 mode initialization (Fig. 6) is similar but more pronounced since high mode in adiabatic initialization tends to weaken further the divergent circulation which is diabatically driven.

2. Cloud water initialization

The lack of initial specification of cloud water/rain water for the explicit cloud water /rain water physics included in the SSM is another major reason for the "spin-up" problem. Initial efforts toward cloud water initialization seek to build the initial cloud water profiles using a parabolic distribution based on the satellite-simulated total amount of cloud water in each mesh column between (satellite) observed cloud top and "diagnosed" cloud base. The diagnosed cloud water distribution shortens the spin-up time, even though the initial rain water is still neglected.

Fig. 7 (a), (b) are the comparisons of hourly domain grid-scale rainfall and coverage under different initial cloud water specifications. The initial T, q, u, v fields of these forecasts are from the "control run" described in the previous section. These forecasts represent the control run (thick solid line) which keeps the initial cloud water and rain water; a forecast without initial cloud/rain water (thin solid line) which is similar to the current CRAS; a forecast with "correct" initial cloud water distribution but no rain water (dashed line); and a forecast with the diagnosed cloud water distribution and no rain water. It is shown that the forecast with zero initial cloud/rain water has the most obvious spin-up problem. The spin-up time is three hours. Precipitation of the forecast with diagnosed initial cloud water distribution is close to that with "correct" initial cloud water distribution, but the coverage of this forecast is smaller than that "correct" one. With initial cloud water distribution, Fig. 7 (a) shows that the spin-up time shortens by approximately one hour.

Other experiments have tested the impact of diabatic initialization and cloud water initialization on more realistic analyses (i.e. not the control run). To simulate measurements from a synoptic scale network, a Barnes' Gaussian weighting function was used to smooth model output u, v, q grid data which are the initial u, v, q fields of the control run (3/13/91, 00Z). Figures 8 (a) and 8 (b) show the hourly domain grid-scale rainfall and coverage area of four independent forecasts started from the smoothed u, v, q fields, different initial cloud water specifications, and different initialization procedures. Compared to the control run, the forecast with adiabatic initialization and zero cloud/rain water distribution (thin solid line), which corresponds to the current CRAS model, has the worst spin-up performance; in the case of either diabatic initialization but no initial cloud water (dotted line) or only cloud water distribution but adiabatic initialization (dash-dotted line), the effects on improving spin-up problem are almost same; the forecast with both diabatic initialization and cloud water initialization (dashed line) reduces the "spin-up" problem further. This result indicates that initial enhancement of moisture field (e.g., initial cloud water specification) can enhance the diabatic initialization improvement of the "spin-up" problem. This tendency is further analyzed based on the results of the first two hours of precipitation from these forecasts. The first two hours rainfall of control run is shown in Fig. 9. Corresponding to it, Fig. 10 shows the rainfall from the simulated CRAS forecast (corresponding to the thin solid line in Fig. 8). Fig. 11 represents the rainfall of the forecast adiabatically initialized but with non zero cloud water distribution. The rainfall produced by the forecast with both diabatic initialization and non zero initial cloud water distribution is shown in Fig. 12. Both rainfall amount and coverage area of Fig. 12 are closer to the control run. However, since the diabatic heating rates are evaluated by the prediction model during the very first hours of forecast, a deficiency of rainfall amount and coverage still exist.

3. Summary and future work

The main conclusions reached concerning diabatic initialization and cloud water initialization are listed below.

1. With noise-free diabatic heating rates, diabatic vertical mode initialization can be used to generate divergent circulations which are consistent with the heating and are dynamically balanced. The main feature to note is that diabatic initialization is effective only when the higher vertical modes (≥ 3) are initialized.
2. Cloud water initialization is effective in shortening the surface precipitation spin-up time, even though the initial rain water is still neglected. Combining both diabatic initialization and initial cloud water specification can further reduce the precipitation spin-up time.
3. While the diabatic initialization with the noise-free heating rates is effective in shortening spin-up time, the diabatic heating evaluated by the prediction model during the very first hours of integrations is deficient. It is, therefore, necessary to develop a method based on other independent data sources (e.g., satellite-observed water vapor, cloud liquid water and surface rain rates) to modify initial moisture field in order to improve the spin-up problem in the amount of condensation or the amount of released latent heat. Further, the diabatic heating evaluated by the prediction model should be corrected based on surface rain rates.

List of Figures

Fig. 1. The evolution of surface pressure during forecast started from the uninitialized (dash-dotted line), adiabatic initialization (solid line) and diabatic initialization (dashed line) for a grid point in a rainfall area.

Fig. 2. Hourly domain grid-scale precipitation during the forecasts with adiabatic VMI and initializing variance vertical modes.

Fig. 3. As in Fig. 2, but for diabatic initialization.

Fig. 4. Two hours precipitation forecasted by the control run.

Fig. 5. Difference in diabatically initialized w field and adiabatically initialized w field (at $\sigma = 0.7$, $p \approx 500$ MB level). 3 modes are initialized.

Fig. 6. As in Fig. 5, but 4 modes are initialized.

Fig. 7(a). Hourly domain grid-scale rainfall under different initial cloud water specification conditions.

Fig. 7(b). As in Fig. 7 (a), but for hourly domain grid-scale rainfall coverage area.

Fig. 8(a). Hourly domain grid-scale rainfall under different initial cloud water specifications and different initialization procedures.

Fig. 8(b). As in Fig. 8 (a), but for hourly domain rainfall coverage area.

Fig. 9. Two hours precipitation forecasted by control run.

Fig. 10. Two hours precipitation predicted by a forecast with adiabatic initialization and zero initial cloud water distribution.

Fig. 11. Two hours precipitation predicted by a forecast with adiabatic initialization and non zero initial cloud water distribution.

Fig. 12. Two hours precipitation predicted by a forecast with both diabatic initialization and non zero initial cloud water distribution.

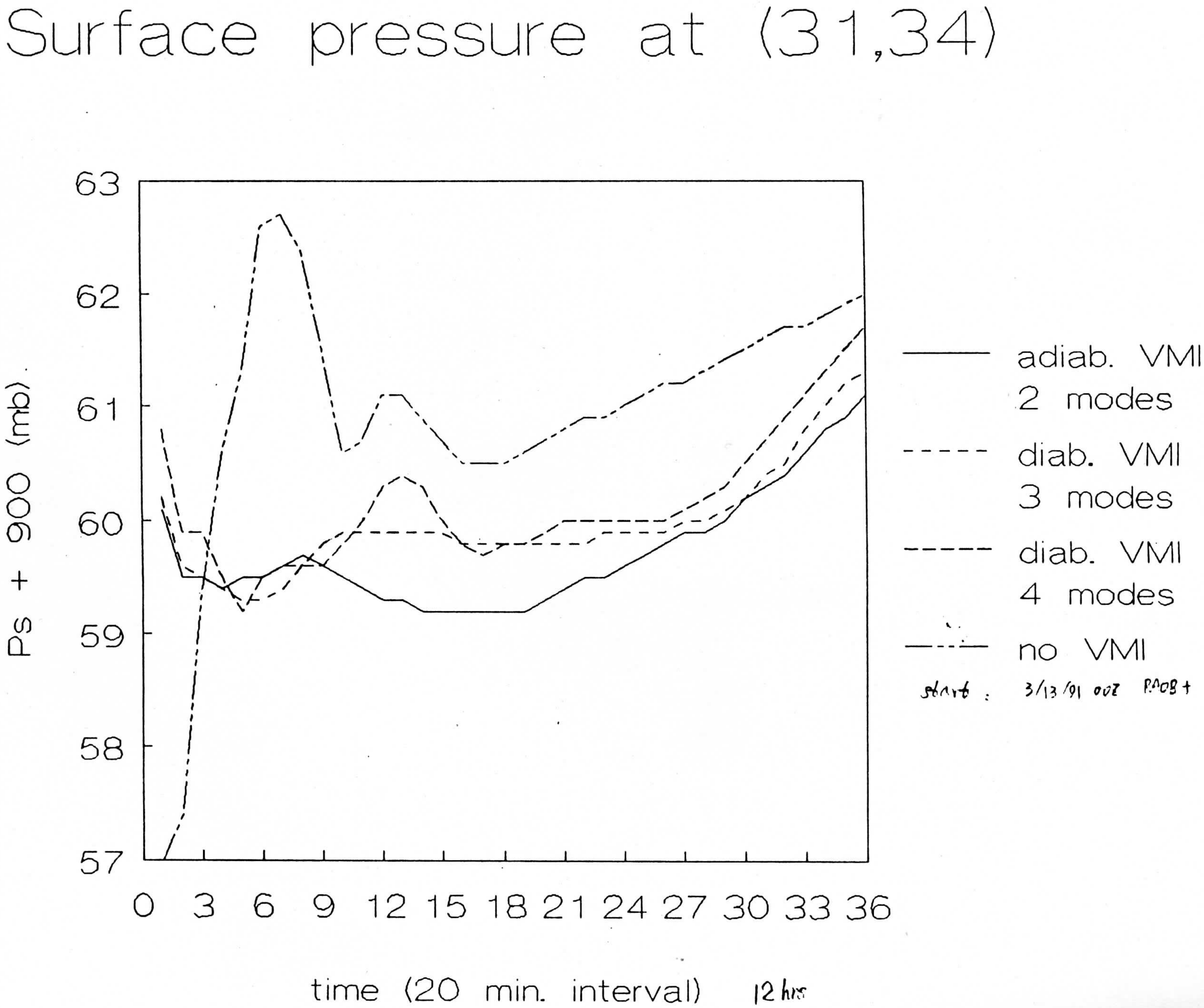

Fig. 1 The evolution of surface pressure during forecast started from the uninitialized (dash-dotted line), adiabatic initialization (solid line) and diabatic initialization (dashed line) for a gridpoint in a rainfall area.

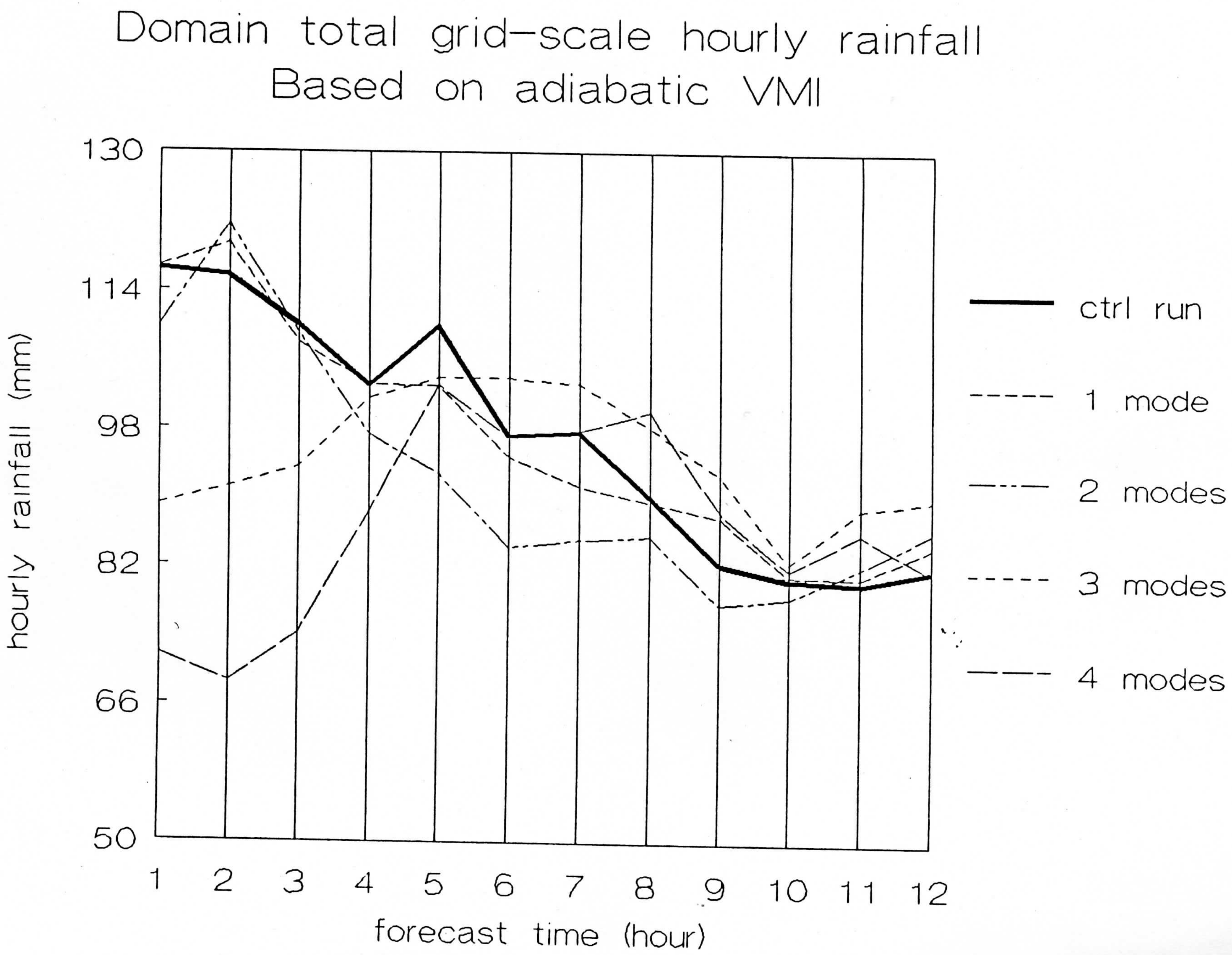

Fig. 2 Hourly domain grid-scale precipitation during the forecasts with adiabatic VMI and initializing variance vertical modes.

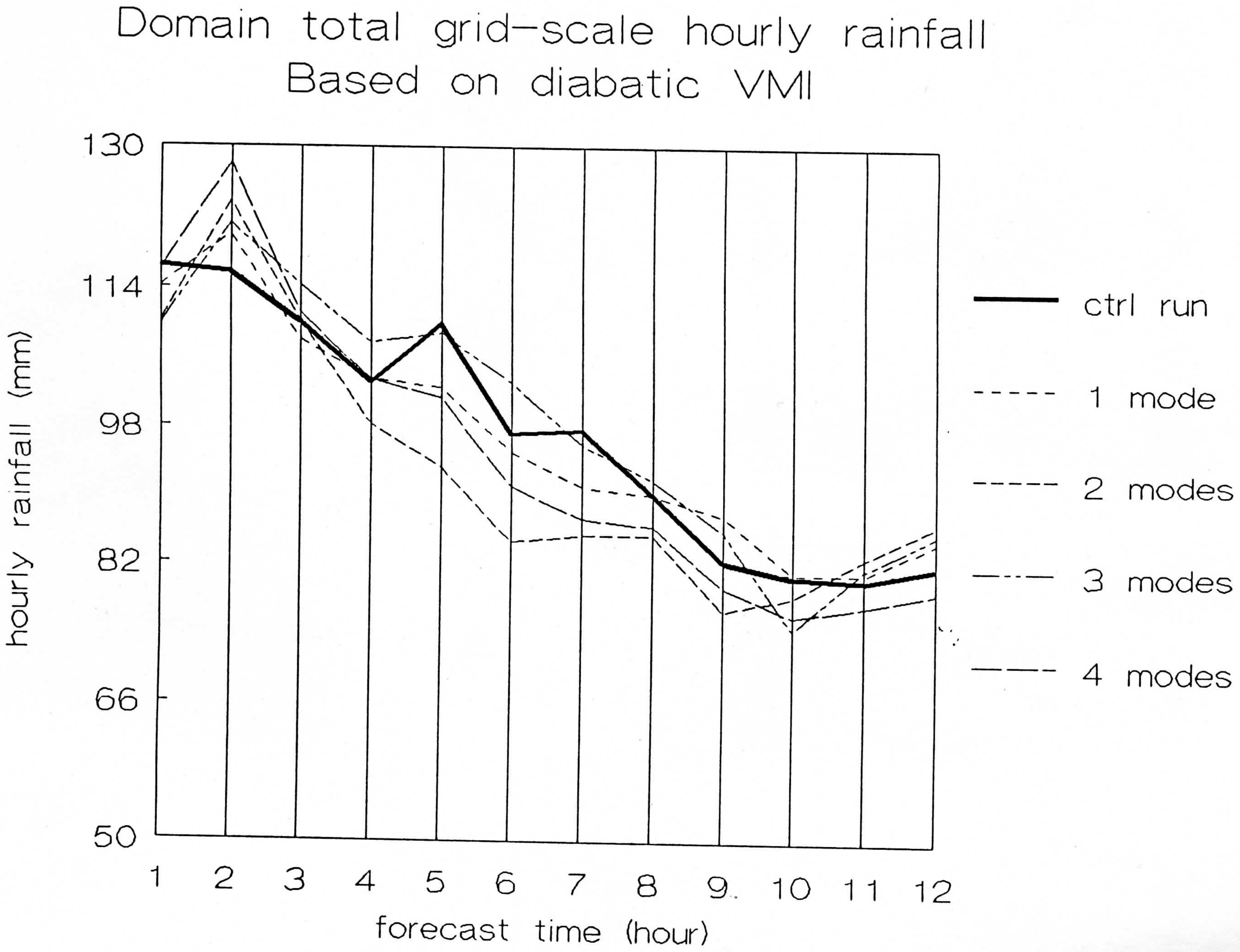

Fig. 3 As in Fig. 2, but for diabatic initialization.

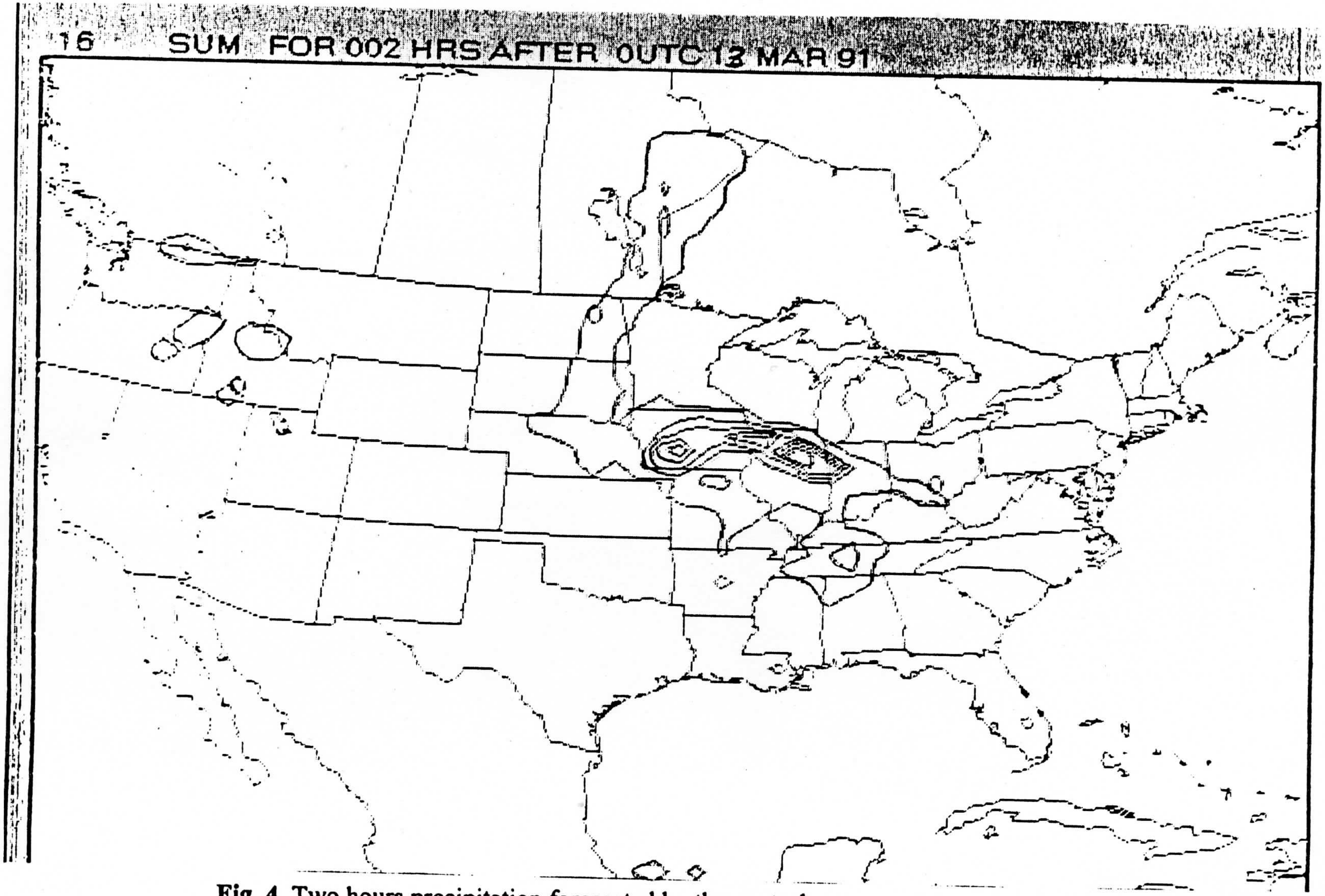

Fig. 4 Two hours precipitation forecasted by the control run.

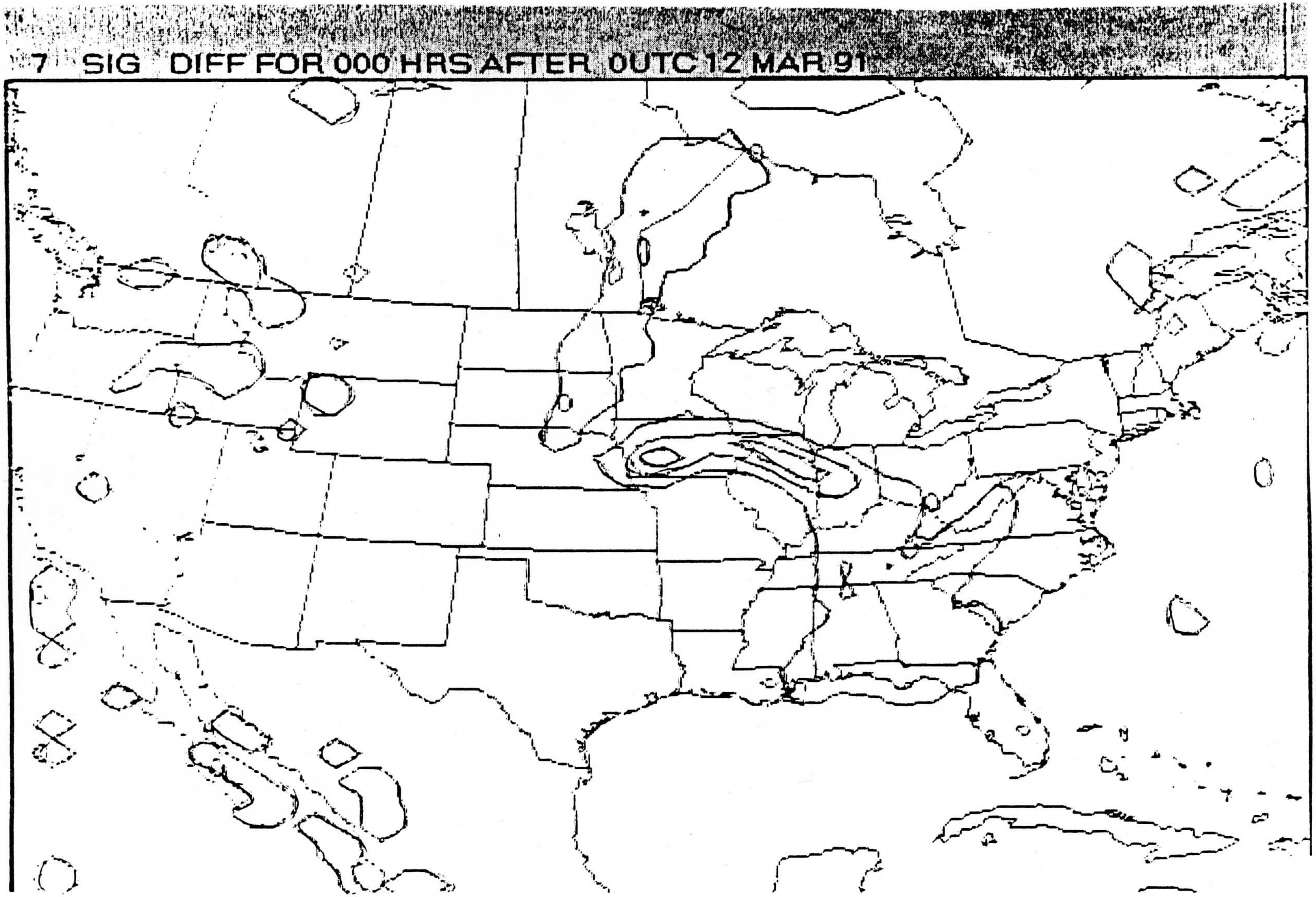

Fig. 5 Difference in diabatically initialized ω field and adiabatically initialized ω field (at $\sigma = 0.7$, $p \sim 500$ mb level). 3 modes are initialized.

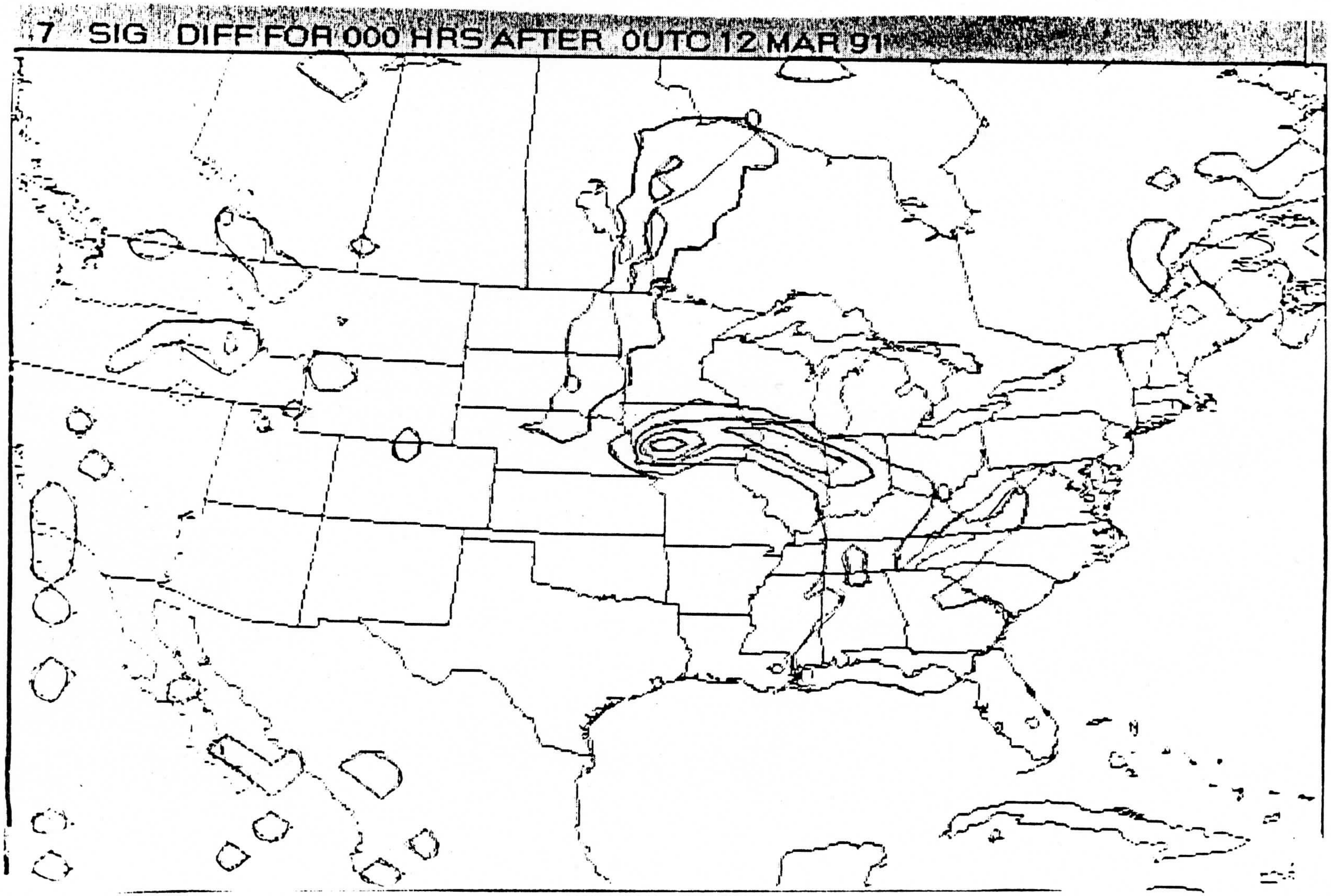

Fig. 6 As in Fig. 5, but 4 modes are initialized.

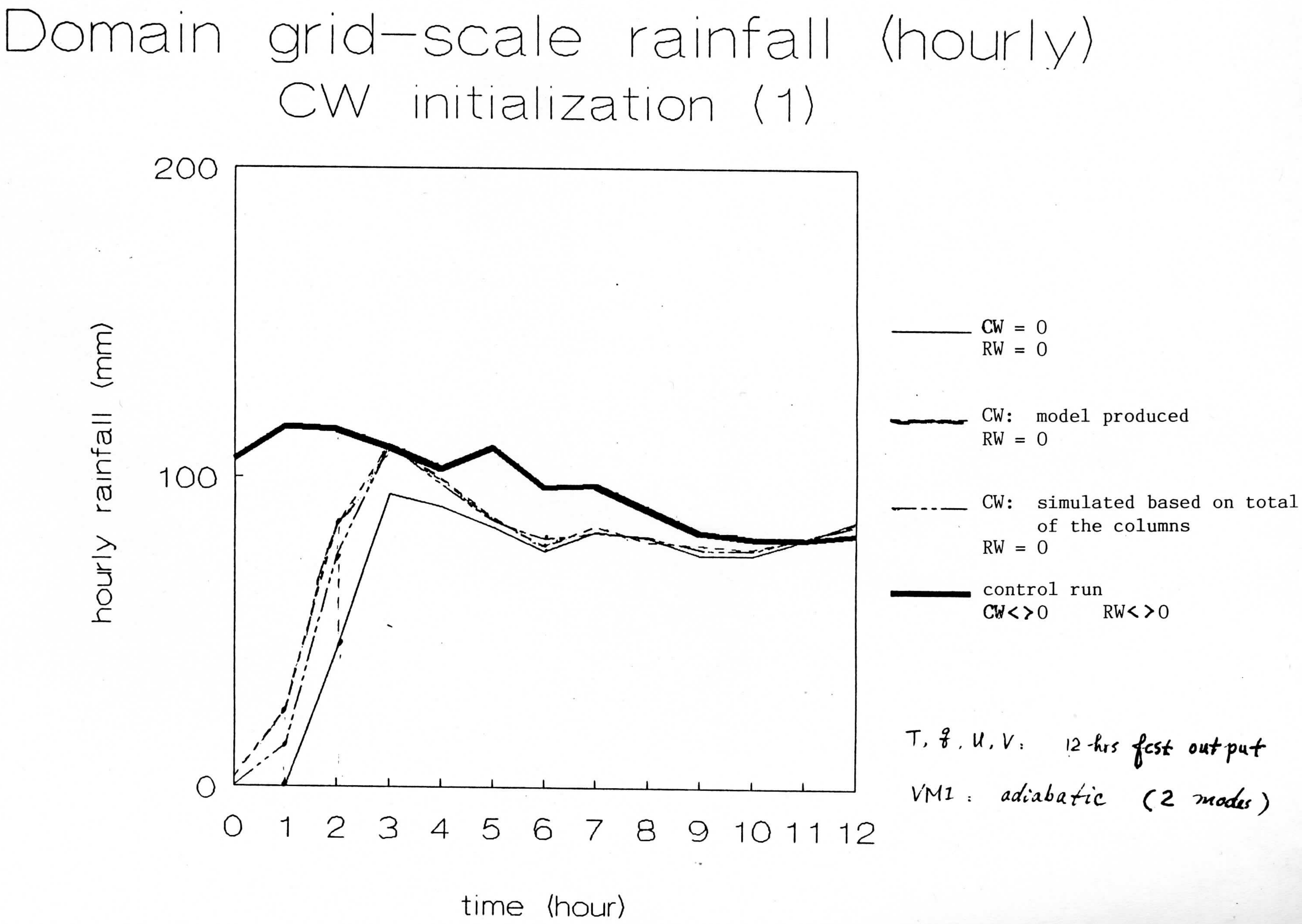

T, q, u, v: 12-hrs fcst output

VM1: adiabatic (2 modes)

Fig. 7 (a) Hourly domain grid-scale rainfall under different initial cloud water specification conditions. To test the effects of cloud water for rainfall forecasting.

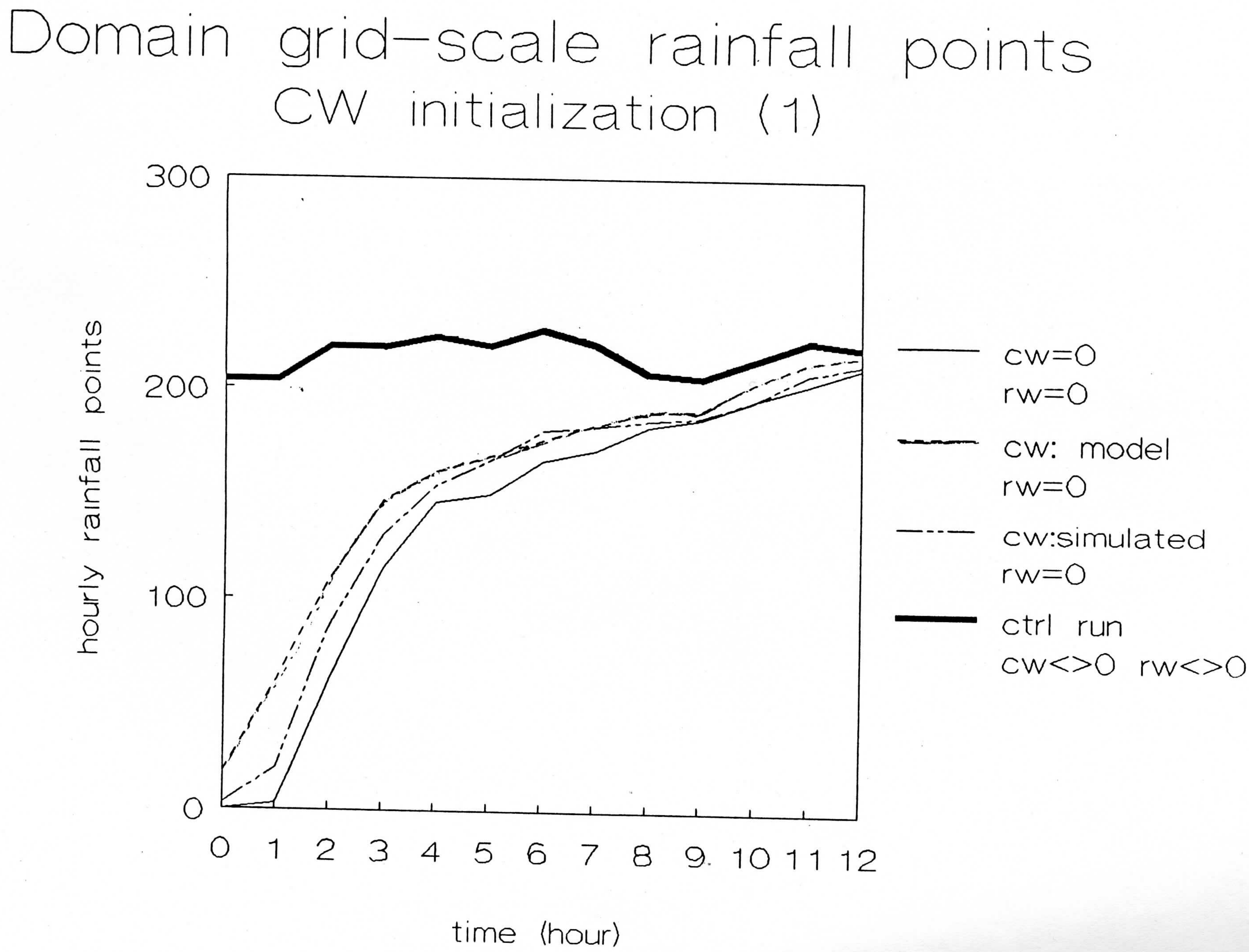

Fig. 7 (b) As in Fig. 7 (a), but for hourly domain grid-scale rainfall coverage area.

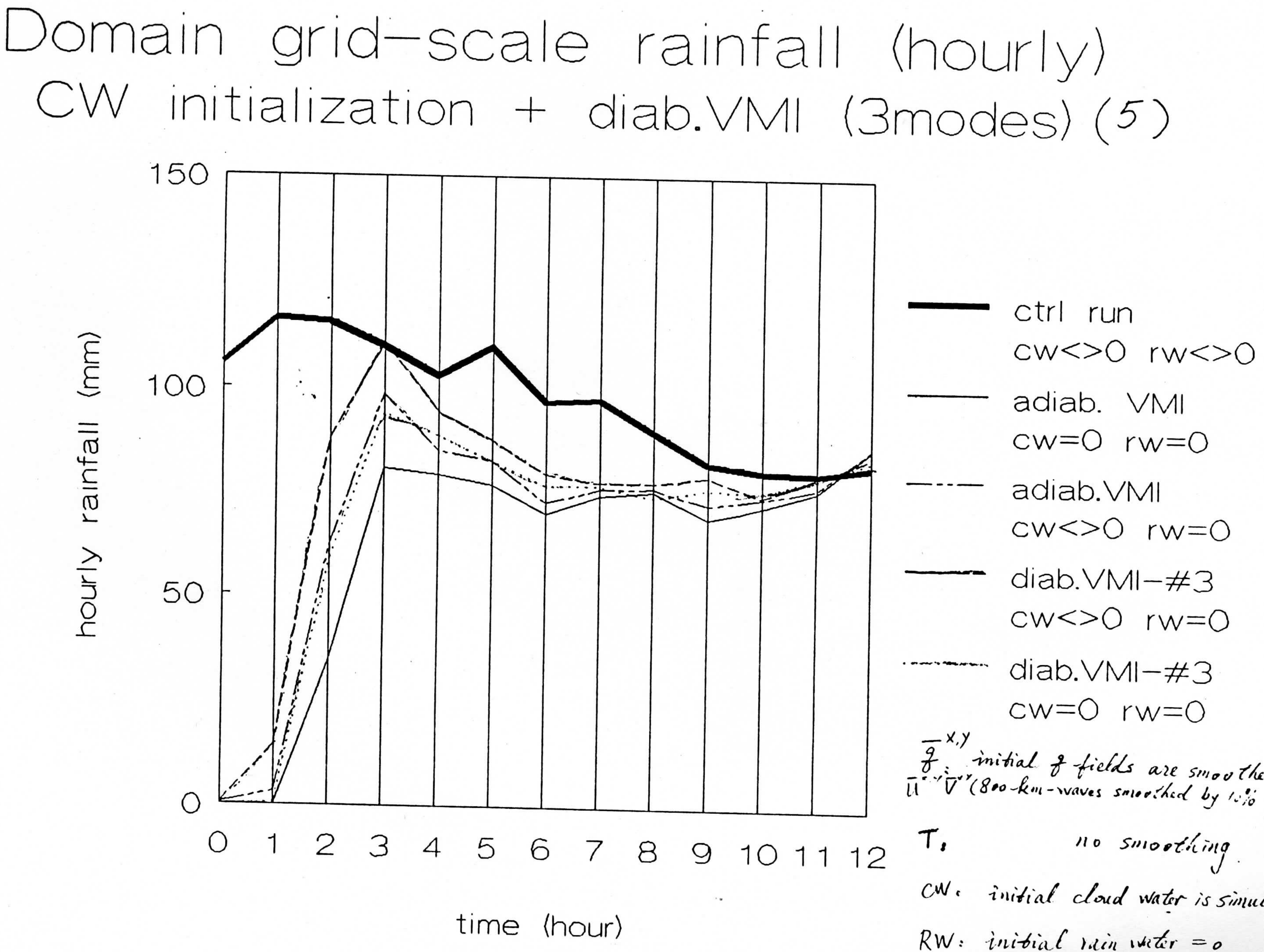

$\overline{q}^{x,y}$: initial q fields are smoothed;
$\overline{u}^{x,y}$ $\overline{v}^{x,y}$ (800-km-waves smoothed by 10%)

T : no smoothing.

CW : initial cloud water is simulated.

RW : initial rain water = 0

$\overline{QR}^{t}$: time averaged.

Fig. 8 (a) Hourly domain grid-scale rainfall under different initial cloud water specifications and different initialization procedures.

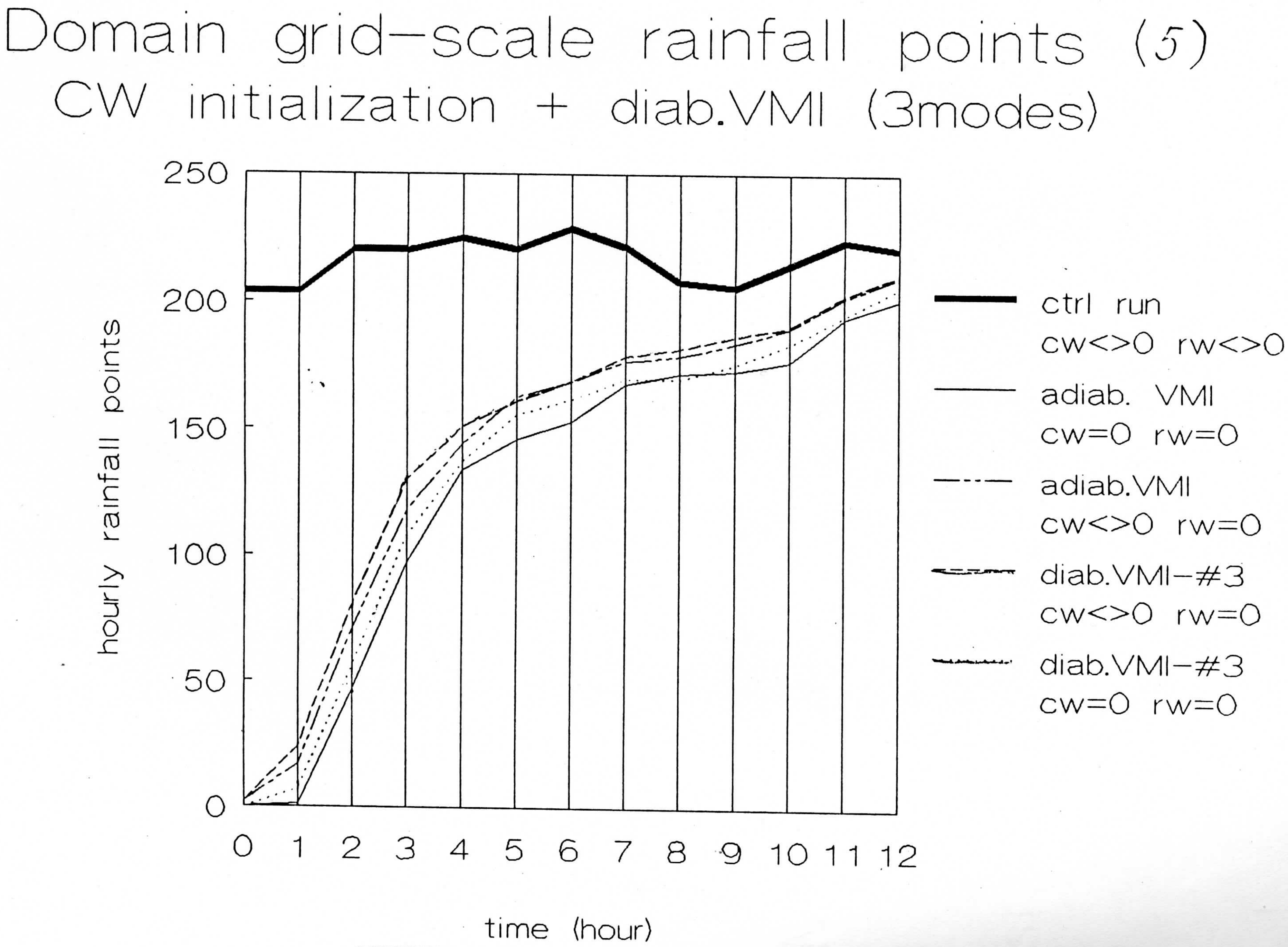

Fig. 8 (b) As in Fig. 8 (a), but for hourly domain rainfall coverage area.

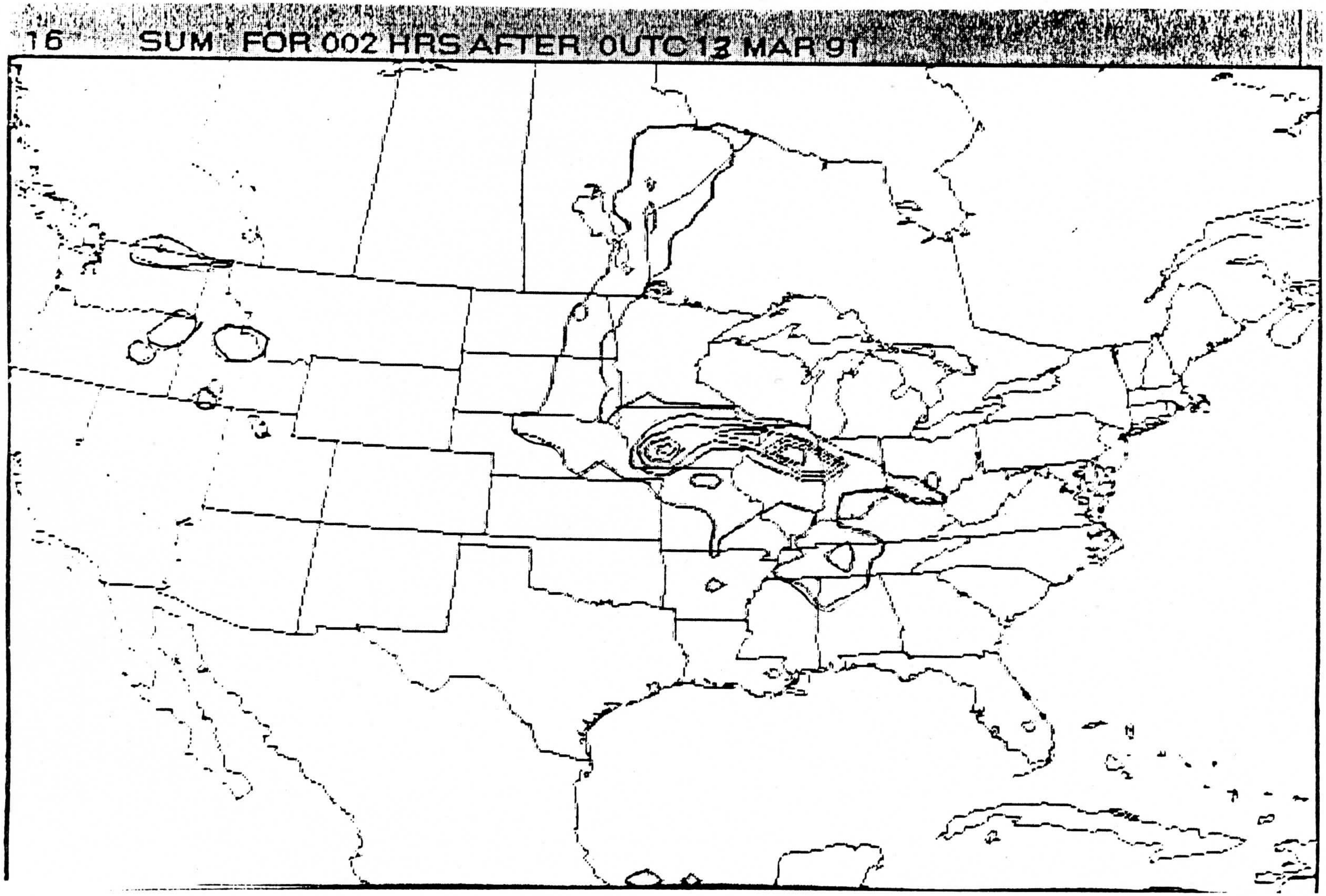

Fig. 9 Two hours precipitation forecasted by control run.

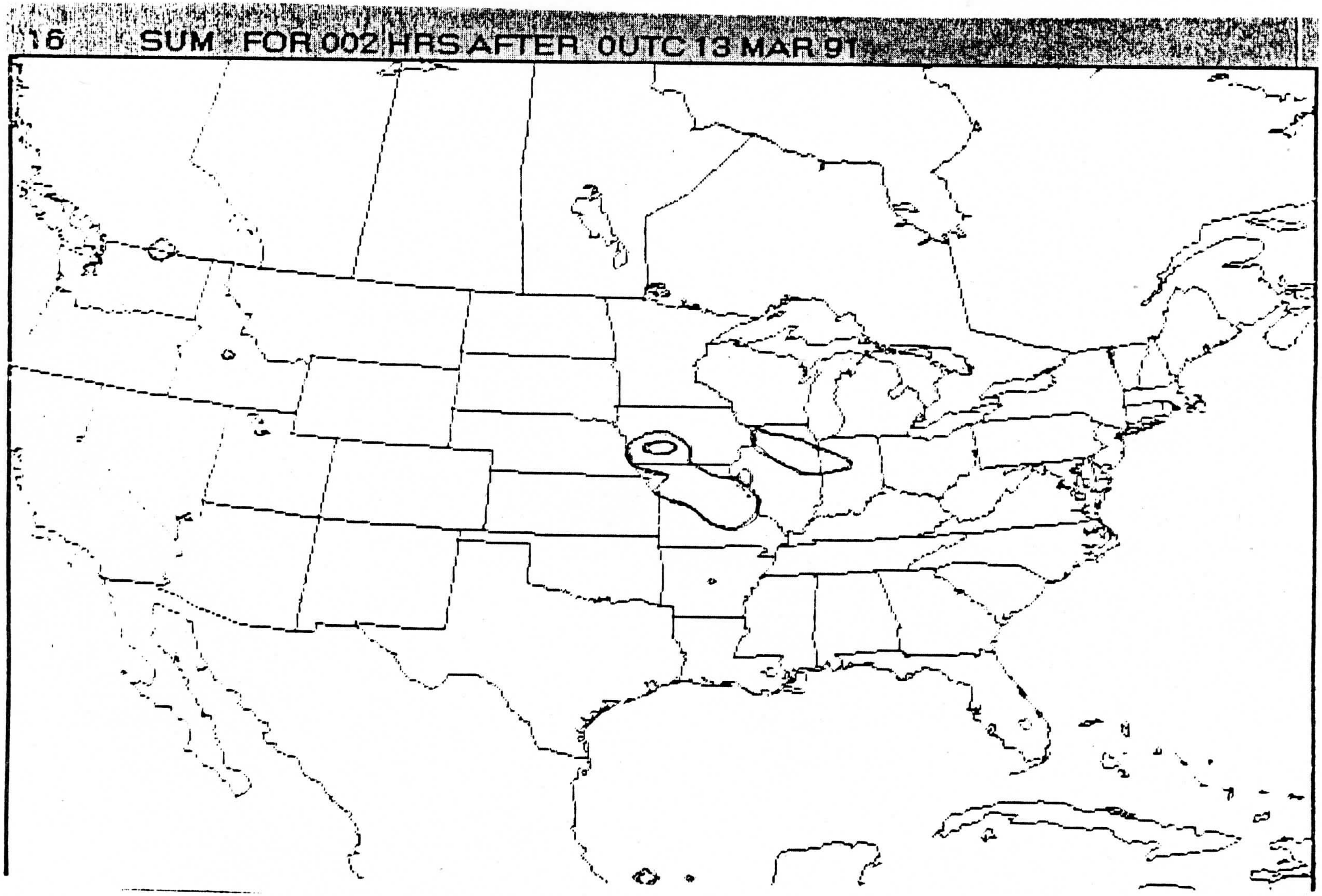

Fig. 10 Two hours precipitation predicted by a forecast with adiabatic initialization and zero initial cloud water distribution.

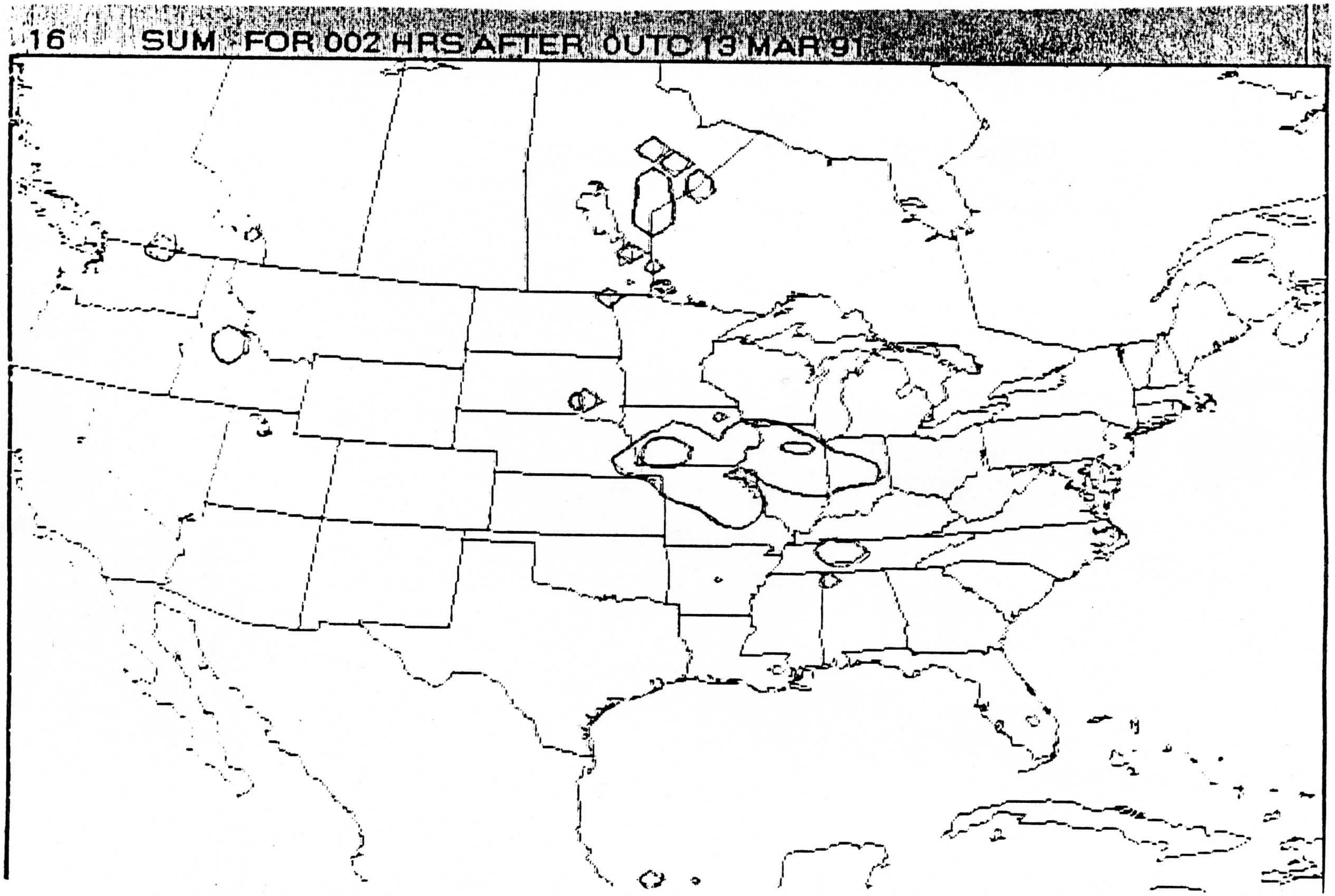

Fig. 11 Two hours precipitation predicted by a forecast with adiabatic initialization and nonzero initial cloud water distribution.

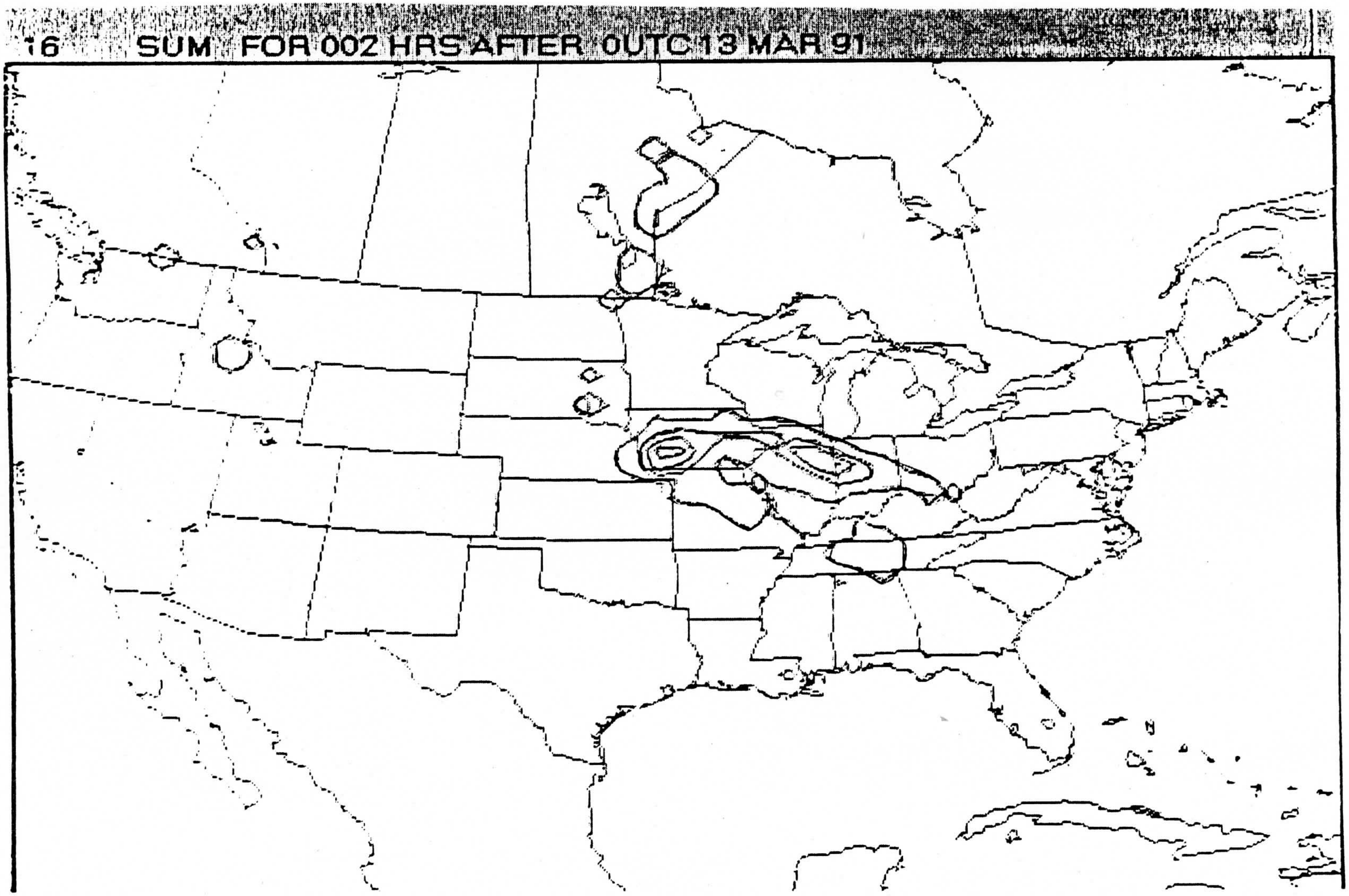

Fig. 12 Two hours precipitation predicted by a forecast with both diabatic initialization and nonzero initial cloud water distribution.

F. The improvement and implementation of the automated WINDCO system. Contributed by Christopher M. Hayden and Christopher S. Velden.

Introduction

Satellite Measured Winds (SMW) have been derived from time sequenced imagery since the inception of the geostationary meteorological satellite (ATS-1, 1966). In broad terms, these SMW fall into two classes representative of low and high level flow. The former is associated with the motion of cumulus humilis, the latter generally with cirrus. Since the discrimination of SMW is a pattern recognition problem, it would seem to lend itself naturally to automated techniques, and, in fact, for lower-level tracers, automated techniques have been in use for many years (Leese et al., 1971). For the high level tracers, however, progress has been slow. The targets are more tenuous, and it has proved difficult to substitute for the eyeball, although the manpower intensive effort required by this tool in routine operations has long been a bane to managers. Relatively recently, automated methods have been introduced to operations, first by the European Satellite Operations Center (ESOC) (Schmetz and Nuret, 1987), and now by NESDIS (Merrill et al., 1991), to obtain upper-level motion. However, somewhat perversely, the manpower intensive aspect of the procedure did not disappear, but merely shifted to the task of editing, since the current automated algorithms do not include sophisticated quality control, particularly with respect to the height assignment. An automated quality control procedure which is to be applied in the NESDIS SMW production has recently been introduced.

Approach

Automatic processing of the SMW at NESDIS involves; target selection (from image 1 of a sequence) based on brightness temperature and spatial gradients; pressure height assignment by a variety of methods; a first guess displacement derived by time and space interpolation of forecasts from the National Meteorological Center (NMC); and modification of the first guess by minimizing the difference between a template about the target in image 1 and a similar template in image 2 which is searched over a fixed area centered at the first guess displacement. The last step is repeated using the second and a third image to give two vector estimates for each target. The final SMW value is the average of the two.

The use of the forecast for quality control by the data producer is a step not lightly taken. This process could be, should be, and usually is performed by the user of the data. Why then are we proposing it? One reason is to provide the user with an often requested quality flag which he may or may not use at his discretion. A second reason is to edit SMW which are clearly in error, as these only serve to diminish confidence in the product. The manual editing already provides this function, but as mentioned earlier, we are seeking to replace this manpower intensive task.

Finally, and perhaps most importantly, we are experimenting with using the objective analysis to reassign the pressure height, the rationale being that the height assignment is the greatest source of SMW error. Unquestionably, the tracers indicate motion in the atmosphere. It may not be motion of the air at a given level, as we commonly assign it, but it is certainly some layer-averaged atmospheric motion. In reassigning the pressure height via objective analysis, we seek to assign the SMW to the level where it best fits other information. In this sense the quality control has an element of data assimilation as well.

Method

The objective analysis used in the SMW quality control is an adaptation of the 3-dimensional recursive filter analysis described by Hayden and Purser (1988). In this application, the analysis is performed over the entire western hemisphere from 50S to 60N at 13 levels as shown in Table 1. The grid spacing is 2.4 degrees of latitude and longitude on a pseudo Mercator projection. The same NMC 6 hour forecast used to provide first guess displacements for the SMW generation is used to provide both a background field and "guess reports" for the objective analysis. The latter are complete vertical profiles on a uniform, low density pattern which are treated as reports throughout the analysis' iterations. The analysis is of the successive approximation type and uses five iterations.

Fig. 1 is a schematic of the quality flag/height reassignment algorithm. As currently configured it is a three step process as indicated by the numbered arrows. The first step is an analysis accomplished using the SMW at their original height assignment. Quality control implicit to the analysis system (described below) is in effect. The second step performs a pressure altitude reassignment, and the third step involves a re-analysis with the SMW at their new height assignment and provides final quality flags.

At each iteration of the analysis, a quality indicator varying between zero and one is assigned to each observation based on a simple empirical function. This function (Fig. 2) involves the "fit" of the data D (observation minus background), an assigned "tolerance" T (explained below), and an exponent which controls the shape of the function (larger exponent leads to sharper slope). Fig. 2 (top) shows the function for several choices of exponent. The quality function may be tuned by adjusting either the tolerance or the exponent n. Note that independent of the exponent, if D = T, (i.e. the fit equals the tolerance), the quality Q is 0.5. Also, if D = 0 (the fit is exact) the quality Q is 1, independent of both T and the exponent. In current practice, the value of n is 2. Tolerance is varied by both vertical level and iteration, with initial values as given in Table

1. Since the fit for good data improves with succeeding iterations, the tolerance is reduced according to

$$T = Tl + Ts^{i-1} * (T0 - Tl) \qquad (1)$$

where T0 and Tl (we use Tl=T0/5) are initial and final tolerances, Ts is a slope factor (we use 0.7) and i is the iteration. This relationship for a normalized tolerance is shown in the bottom of Fig. 2.

Table 1. Pressure levels and initial tolerances

Level	Tolerance
925	15
850	15
775	15
700	18
600	18
500	20
400	20
350	25
300	25
250	25
200	30
150	30
100	30

At the end of the first step shown in Fig. 1, each SMW has had the opportunity to influence the analysis and has an associated quality flag from the process. It is possible at this point to stop and use that flag as the final quality indicator. We have chosen instead to continue with an assimilation step where the pressure altitude may be reassigned. For each SMW an attempt is made to minimize, in the vertical pressure coordinate (p), the penalty function:

$$((V(p)-SMW)/VV)^2 + ((T(p)-TC)/VT)^2 + ((P-PW)/VP)^2 \qquad (2)$$

where TC and PW are the temperature and pressure of the SMW assigned during generation. T(p) is obtained from the global temperature guess. The denominators VV, VT, and VP are weights which may be varied to emphasize the vector, temperature or pressure terms respectively. Currently these are given the empirically determined values 20, 200 and 200 where the units of the variables are ms^{-1}, K, and MB. We have not explicitly included the quality flag resulting from the initial analysis step, although it is certainly implicitly included via the "fit" of the first term in (2). The height reassignment may fail if no minimum is found or if the minimum is too large (we use 100 as a limit). In this instance the SMW is fatally flagged as a bad vector.

The full analysis is repeated in step 3 using the output of the first analysis as a background field, the initial "guess" reports, and the reassigned SMW (excluding those fatally flagged in the height reassignment). The output of this procedure provides the final quality flags. SMW which do not attain a certain quality are again fatally flagged as bad vectors. Currently we are using a fixed threshold of .75, but this is clearly not optimum for all situations.

Results

Fig. 3 is a scatter diagram where the abscissa represents the pressure altitudes assigned by CO_2 slicing (Merrill et al., 1991) and the ordinate the reassigned altitudes. The plot is for an hemispheric sample achieved at one time period. It is apparent that the reassignment has a substantial impact at all levels. The reassignment appears to reduce the pressure variability at low levels, but not at higher levels. For the latter there seems to be no systematic trend toward assigning either higher or lower pressures. The standard deviation of the pressure change is of the order of 50 MB.

Fig. 4. is a plot of original (top) and reassigned (bottom) pressure altitudes for a small section of the eastern tropical Pacific which includes the ITCZ and the subtropical jet. There is an indication that the reassignment places the SMW higher in the jet (over Mexico) and lower in the stratus (off Baja), which seems qualitatively correct, but the reader is left to draw his own conclusion.

Fig 5 is a diagram detailing the disposition of 435 targets selected in the NESDIS operational processing of data in support to the National Hurricane Center, where the area of consideration is bounded by 2-50 N and 40-140W. In this instance only the SMW from infrared window imagery with CO_2 slicing pressure assignment are considered although in practice water vapor and VAS gradient winds are also processed. The number of targets is dependent on a density selection available in the system, and in this case we sought one target per 24 x 24 Pixel template which is the standard NHC processing procedure. The figure shows that approximately half of the targets yielded acceptable winds. Most failures occurred during the wind processing with the acceleration check trapping the most (15 percent). Fifteen percent were fatally flagged by the auto editor.

Fig. 6 presents a scatter diagram and statistics for the sample of Fig. 5 as compared to rawinsondes. The abscissa is the error of the first guess and the ordinate the error of the SMW. Small crosses depict the full sample of 76 matches (within 3 hours and 110 km). The small boxes represent the 53 samples which passed the wind processing quality control, whereas the larger boxes are the 46 samples remaining after the auto editing. The larger solid boxes indicate where the original pressure altitude assignment was retained. The open boxes indicate where the pressure was reassigned. The statistics in the figure show that the two stages of quality control have significantly reduced the error of the SMW from 7.5 to 4.7 ms^{-1}. However, even the latter figure remains slightly higher than the error of the forecast which is 3.9 ms^{-1} for this sample. We typically find that the edited winds have an error comparable to the forecast with the parameters for the editing set as they currently are. Fig. 6 is particularly gratifying in that there are no examples where an SMW with small error, associated with a large forecast error, has been flagged. Such is not always the case.

Summary

The foregoing has given a brief overview of an automatic quality control algorithm which has been prepared for SMW. We make no claim that the system is optimized; as with any objective analysis procedure there are numerous ways of empirically tuning. Nor have we described here the many details included in the system. For example, the acceleration check is revisited during the auto editing and, at the suggestion of the second author, high wind speeds are treated more leniently in terms of the fatal flagging threshold (if they are faster than the forecast). Nevertheless, the system is very promising, and the current statistical performance which yields errors comparable to those of the forecast is acceptable. A great deal of detailed analysis remains to be done, particularly for individual cases where good SMW are fatally flagged in areas of very poor forecast. We would like to find ways of retaining these. It should be noted that the fatally flagged SMW are not forwarded to the user. In a related but more general issue, we would like to improve the correlation between poor data and low quality flags. Unfortunately, there is currently no provision for passing more than one pressure altitude in the GTS format, so the altitude given is the result of the data assimilation rather than the initial more forecast-independent method. In partial compensation, the temperature associated with the SMW is <u>not</u> changed, so the user can infer a good estimate of the original height assignment if he so desires, and he can perform his own data assimilation adjustments as he pleases. We feel that the data assimilation method is the right approach, especially for tracers which do not have the advantage of CO$_2$ slicing.

List of Figures

Figure 1. Algorithm for reassigning pressure altitude based on 3-d recursive filter analysis.

Figure 2. top: Empirical function used to assign quality flags. Function involves ratio of "fit" D and "tolerance" T. Bottom: Normalized tolerance assignment as a function of analysis iteration.

Figure 3. Scatter plot of initial pressure altitude assignment (PW58) and reassigned pressure (APW).

Figure 4. Top: Original SMW pressure altitude from CO$_2$ slicing method. Bottom; Reassigned SMW pressures. Case is for June 13, 1991.

Figure 5. Distribution of flags for 435 targets assigned in processing of window SMW for NHC support, June 14, 1991. "Final" indicates portion passing all tests. Auto refers to sample fatally flagged by auto editor.

Figure 6. Scatter diagram of SMW error, as compared to rawinsondes, vs. NMC forecast error at same location. Matches are taken from sample of Fig. 5. Crosses are SMW that failed processing tests before auto editor. Small rectangles indicate flag by auto editor. Large rectangles are SMW that passed all tests.

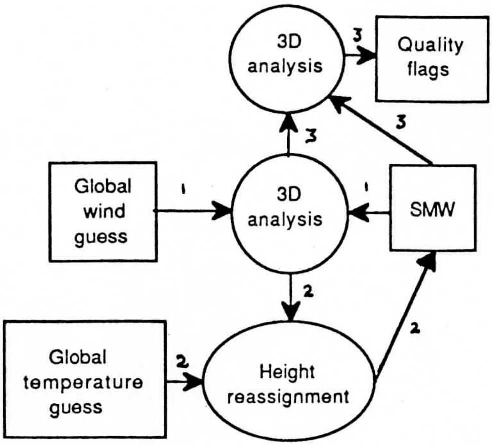

Figure 1. Algorithm for reassigning pressure altitude based on 3-d recursive filter analysis.

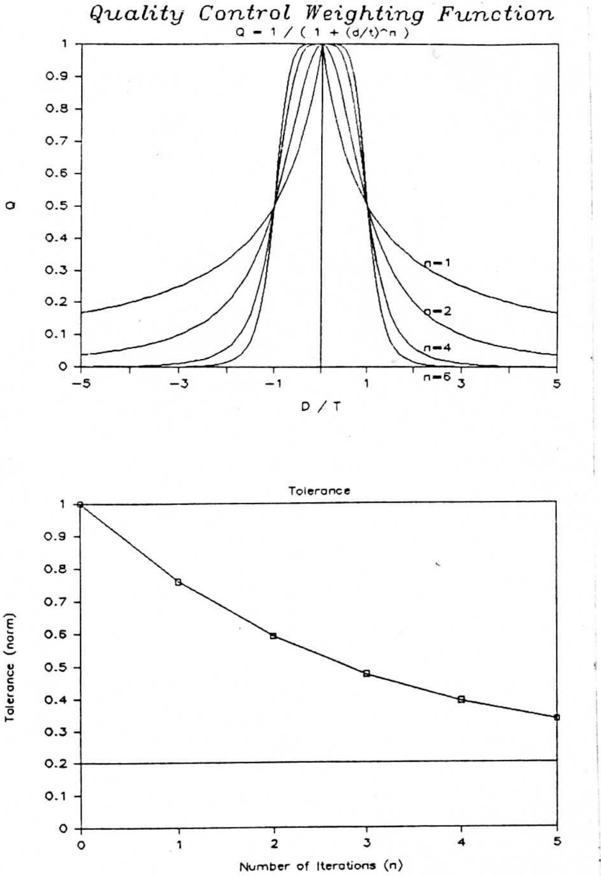

Figure 2. top: Empirical function used to assign quality flags. Function involves ratio of "fit" D and "tolerance" T. Bottom: Normalized tolerance assignment as a function of analysis iteration.

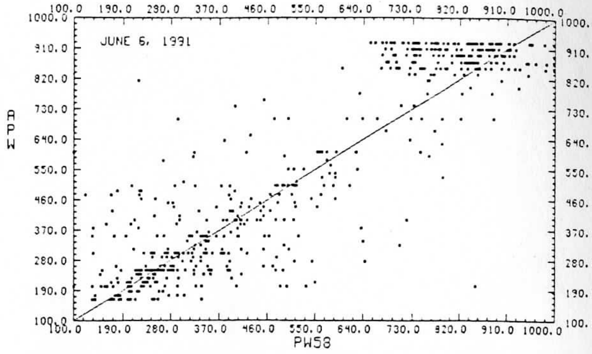

Figure 3. Scatter plot of initial pressure altitude assignment (PW58) and reassigned pressure (APW).

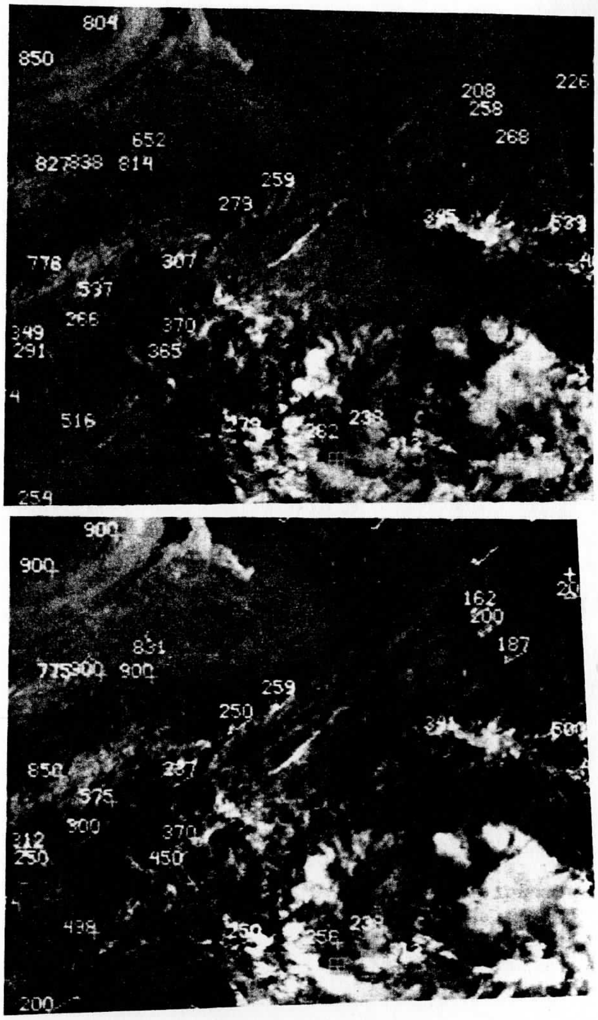

Figure 4. Top: Original SMW pressure altitude from CO_2 slicing method. Bottom; Reassigned SMW pressures. Case is for June 13, 1991.

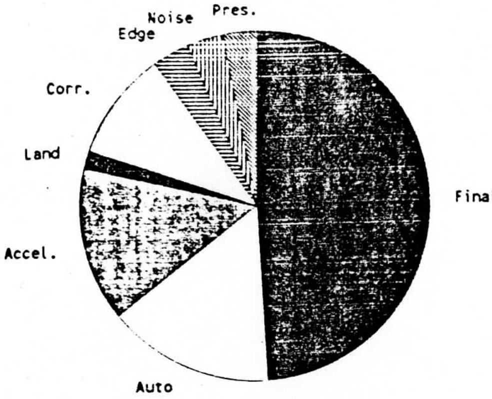

Figure 5. Distribution of flags for 435 targets assigned in processing of window SMW for NHC support, June 14, 1991. "Final" indicates portion passing all tests. Auto refers to sample fatally flagged by auto editor.

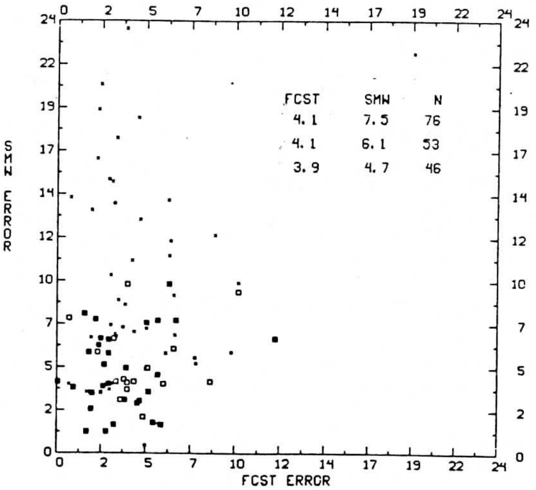

Figure 6. Scatter diagram of SMW error, as compared to rawinsondes, vs. NMC forecast error at same location. Matches are taken from sample of Fig. 5. Crosses are SMW that failed processing tests before auto editor. Small rectangles indicate flag by auto editor. Large rectangles are SMW that passed all tests.

G. Using a modified version of WINDCO in the polar regions. Contributed by Leroy D. Herman.

Introduction

Polar orbiting satellites in the NOAA series scan the earth from pole to pole providing complete coverage of the earth twice a day. These satellites carry the Advanced Very High Resolution Radiometer (AVHRR) on board to obtain observations in 5 wave lengths. Even before the first NOAA satellite was launched it was recognized (Shenk and Kreins, 1969) that it was possible to measure cloud motions from NIMBUS II where consecutive orbits overlap. In the past practical considerations prevented this. With advancing technology, these difficulties have been overcome (Turner and Warren, 1989). With the satellites passing over the poles on each orbit, high latitudes have complete coverage to about 58 degrees latitude.

Previous work has shown that the system known as WINDCO (Smith and Phillips, 1972) has the ability to detect and measure cloud motions from geostationary satellites. By adapting polar orbiting satellite data, this system of measuring cloud motion vectors is also effective at high latitudes (Herman, 1989). Reasonable results were also shown to be possible by Herman (1991), when compared with other in-situ data.

Further details of the use of the technique of measuring cloud motions at high latitudes are given in this paper. Examples of different types of high latitude coverage are shown. In regions where the cloudiness is featureless or barely discernible, an enhancement is described showing how additional cloud vectors can be obtained.

Data Selection

The NOAA satellite series are polar orbiters which pass over the north pole every 100 minutes. Resolution is either 1 km or 3 by 5 km. The width of each scan of the AVHRR instrument is about 2500 km. This coverage permits viewing of the poles on each orbit, and complete overlapping coverage on three successive orbits equatorial to 70 degrees. From that latitude it is possible to obtain complete coverage from two orbits down to about 58 degrees latitude. There a gap in coverage begins and grows until the width of coverage at the equator is only about 30 km.

Satellite images from the AVHRR are ingested into the McIDAS computer system and rectified to a common projection in order for the WINDCO program to operate. For visual tracking of an animated sequence the images are also enhanced by expanding the gray scale over the narrower range of temperatures found at high latitudes. The time interval between orbits is approximately 100 minutes, which is more than three times as long as the normal interval used with geostationary images. The area scanned on each orbit amounts to nearly half of the Arctic region. An example of part of the area of coverage in the Arctic on one orbit is shown in Figure 1.

The WINDCO program used in this research operates in two phases. In the first phase, likely cloud targets are selected. These targets are either the coldest clouds or are near regions where the gradient is strong. A sample is selected from all areas of the image unless gradients are small due to either a lack of clouds or uniformity of cloudiness. A cloud altitude is determined from a histogram estimation of a representative cloud top temperature which is matched with T(p) obtained from the National Meteorological Center's (NMC) global forecast. The second phase of the program uses the NMC wind forecast to determine the most likely area to which the cloud has moved in the given time interval. A search is made for the best correlation fit between the two images in the time interval. The best match between the two images for that target is selected and the cloud motion is measured relative to that displacement.

When clouds are present the system works well, however during the cold winter months over the Arctic Ocean with cold temperatures and little moisture available in the atmosphere clear skies are common. In that case the program may make matches with snow or ice features on the surface. Generally these are indicated by stationary or low velocity vectors. To avoid this as a practical matter, vectors less than 3 mps are discarded during winter. In figure 1 many of the mountains and snow fields of Ellsmere Island and Greenland could produce false, nearly calm cloud motion vectors.

Accuracy of Positioning

In order for the WINDCO program to operate, the AVHRR images must be translated from the satellite projection into a suitable uniform projection. For high latitudes the most favorable projection is a polar stereographic, while at middle and low latitudes a Mercator projection is more appropriate. In general practice the geographic positioning of landmarks has been good to excellent, and when the remapped pictures are animated the landmarks remain generally stationary.

Figure 2 shows a remapped enhanced picture from NOAA-11 of the Arctic Ocean area north of Alaska. The most interesting feature of the picture is the large number of lead lines in the ice which are seen as darker and warmer lines contrasting with the ice. At this time an anticyclone was centered near 76 N latitude and 177 W longitude.

The cloudiness is at low to middle altitudes and during the course of the loop the clouds pass over the lead lines with little or no obscuration of them. The warmest portion of the lead lines have temperatures of -20 degrees centigrade, while the majority of the gray clouds have temperatures of -33 degrees centigrade. The darker clouds are in the inversion layer with temperatures around -26 degrees centigrade. The northern most edge of Alaska is seen at the bottom of the picture.

Density of Vector Observations

One of the problems with using an automated technique for the selection of cloud targets is that the criteria for choosing a target has to be very specific. Certain limits are established in the computer program and these criteria can not be exceeded. In the Arctic, radiation from the very cold surface generally produces an inversion which creates difficulties for selection criteria chosen for mid latitudes. Often in the Arctic there are cases where clouds in the inversion zone are warmer than the surface temperatures. This rarely occurs at mid latitudes.

Another difficulty encountered in the Arctic is that gradients at cloud edges appear to be less than those at lower latitudes. An example of this is shown for a cyclone over Hudson Bay in January in Figure 3. The image is from NOAA-10 in the 11 micrometer window rectified to a polar stereographic projection. The image has been enhanced to bring out detail over a temperature range from about -25 to -50 degrees centigrade.

Figure 3a. shows the cloud motion vector locations measured in this case using the normal selection criteria. After these had been measured it was noted that there were additional cloud motions which seemed to be consistent with the first guess wind field's cyclonic flow over Hudson Bay. The few vectors (14) in figure 3a. do not adequately depict the circulation. To remedy this, modifications of the target selector program were made.

The first modification was to choose potential targets in all the areas where none had been selected on the first pass. The gradient criterion was relaxed and supplementary targets were passed on for further processing. This increased the number of targets from 104 to 233, and the number of vectors that were produced by the correlation program increased from 14 to 60 (see figure 3b.). Although the amount of processing time used was more than doubled, the number of vectors more than quadrupled.

Parallax Problem

Equatorward of the Arctic the viewing angle of clouds in the overlap region from the satellite altitude becomes increasingly oblique, and location errors due to parallax result. This happens because of the change in satellite position in space from orbit to orbit. In effect the satellite is revolving around the earth on a fixed orbit, while the earth rotates beneath it from west to east.

Consider the case of a stationary cloud observed from a pair of orbits which are used to compute cloud motion. On the first orbit the position of a stationary cloud at a given altitude above the earth will appear to be farther to the west than it's true position. On the second orbit the satellite views the cloud looking eastward, which causes an apparent eastward shift from its true position above the earth. Taken together, these two apparent shifts in position cause a false east to west displacement, which can be misconstrued to be cloud motion. For nonstationary clouds the effect is to cause a false west wind component to be introduced and included in the motion computation. In practice, in the zone of prevailing westerlies this component may not be detected by the eye.

The magnitude of this parallax component depends on the altitude of the cloud, the altitude of the satellite, and the nadir angle of the cloud. The cloud altitude and satellite altitude are constant for a given target. The nadir angle is determined by the cloud's position within the satellite field of view for each pass. Hence it is possible to measure the total parallax displacement.

Computations of the parallax effect have been made for a few cases. For NOAA-10, for example, the most northerly point of the path of the sub satellite track is about 81.5 degrees north. Two consecutive orbits cross near 81 degrees. In this vicinity the parallax correction is negligible. For computation purposes, the only locations where the error becomes significant is near the edges of the orbits, because for the most part the viewing angles are similar in the Arctic over the rest of the image. In a Global Area Coverage (GAC) resolution image the error is estimated to be less than 2 mps for cirrus clouds which are more than 15 elements from the image edge. Close to the orbit edge, resolution is somewhat reduced, so care should be taken in using vectors measured there. For a cloud at mid-latitudes with an altitude of 10 km and located 15 degrees of longitude from the sub satellite point on both passes the displacement vector is about 7 mps. Incorporation of a method to automatically correct for the parallax error in the WINDCO system is under development for use, if the technique is applicable at these latitudes.

Conclusion

Experience using the WINDCO program on the McIDAS computer has shown that much of the data that can be produced on this system is of high quality. It has been tested under a variety of conditions in the Arctic with good results. False stationary clouds can be safely discarded and program target selectivity can significantly increase the number of vectors produced. The parallax problem is generally not significant in the Arctic. At lower latitudes where it becomes significant, a system of accounting for its effect is under development.

List of Figures

Fig. 1. Original NOAA-10 AVHRR GAC 10.7 micrometer image for 1525 GMT September 12, 1989.

Fig. 2 Remapped NOAA-10 AVHRR 10.7 micrometer image for 0141 GMT January 5, 1990. The gray scale is enhanced to show more contrast.

Fig. 3. Remapped NOAA-10 images in window channel for 2248 GMT January 27, 1991 showing the Hudson Bay region in Canada. a. Original cloud motion vectors. b. Enhanced method used for selection of cloud motion vectors.

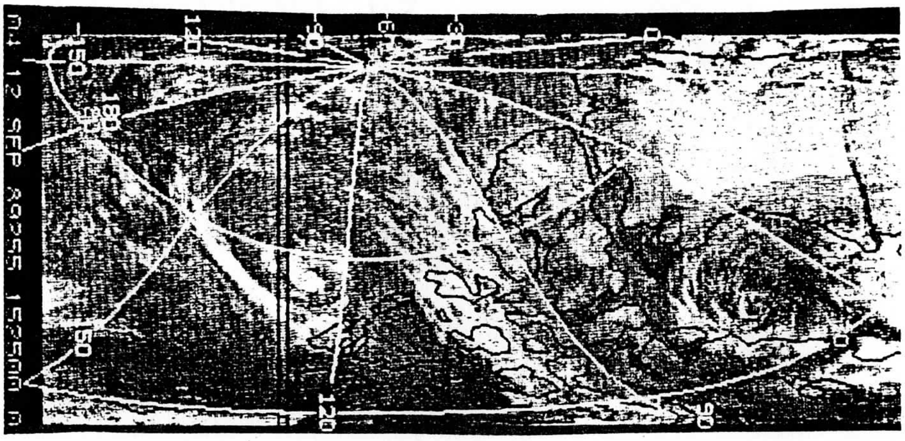

Fig. 1. Original NOAA-10 AVHRR GAC 10.7 micrometer image for 1525 GMT September 12, 1989.

Fig. 2 Remapped NOAA-10 AVHRR 10.7 micrometer image for 0141 GMT January 5, 1990. The gray scale is enhanced to show more contrast.

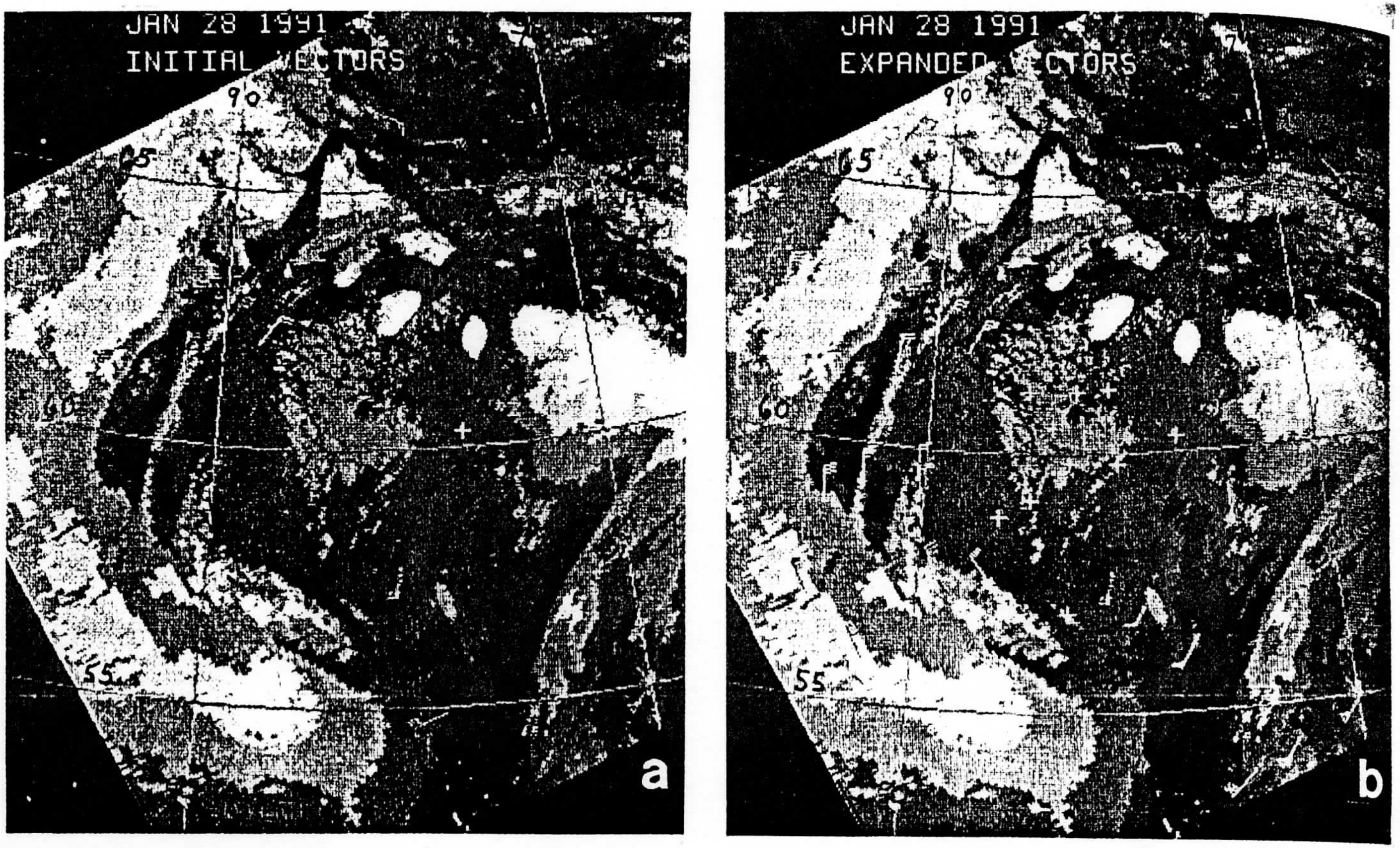

Fig. 3. Remapped NOAA-10 images in window channel for 2248 GMT January 27, 1991 showing the Hudson Bay region in Canada. a. Original cloud motion vectors. b. Enhanced method used for selection of cloud motion vectors.

H. Tracking low level wind patterns based on the "split window" images over cloud free areas. Contributed by Toshiro Inoue.

This study is the first to demonstrate the feasibility of low-level wind estimation over cloud free ocean area using the brightness temperature difference (BTD) images from the split window data of the VAS onboard GOES-7. By tracking small scale features in the BTD images, i.e., water vapor patterns, wind vectors have been derived assuming no vertical wind and no air modification within one hour. The technique is potentially important especially in regions where no appropriate cloud tracers exist. Even though the study is limited to a few cases within the region of 10N to 45N over the western part of the Atlantic Ocean during northern summer, the results show that the BTD wind statistically represents 825 MB level wind with the magnitude of vector error being about 5.2 m/s. This error is comparable to cloud drift wind technique for low levels.

When the cloud free area has significant amount of water vapor, a moisture pattern in the enhanced infrared image is observed as indicated by Aoki (1979) working with AVHRR data. The features of the moisture pattern can be tracked to infer low level wind. Reasonable agreement between the wind derived from enhanced infrared images and the winds derived from BTD images and from cloud motion observed in visible images is found.

The spectral characteristics of VAS split window data are slightly different from AVHRR split window. Since the cirrus cloud characteristics in AVHRR split window are not clear in VAS split window data, visible images are required to discriminate cirrus clouds. Since the AVHRR split window will be obtained in geostationary orbit from GMS-5 and the GOES-I/M, the BTD images can be used to derive both high and low level cloud drift winds, as well as moisture traced winds in cloud free areas. As shown by Inoue (1987, 1989), cirrus clouds and low level cumulus clouds are easily identified in the BTD images. The high cloud winds can be estimated by tracking cirrus clouds which shows larger BTD than cloud free area and low level winds by tracking low level cumulus which shows very small BTD. These results are to be reported elsewhere.

In this study, the BTD winds are estimated over ocean regions where surface temperature is nearly constant within 100 km area. By the inspection of rapid succession of BTD images of hourly intervals over the US continental area, some BTD features show similar movement to winds estimated from near-by rawinsonde data. Further studies conducted over the continents will be reported in the near future.

Although further study is required for a height assignment in the technique, it is believed the level of wind vector in this study is between 700 MB to surface since the peak of the weighting function of the split window is generally lower than 700 MB. Unfortunately, the peak of the 12.2 micrometer weighting function derived from forecast models can probably not be used because of inaccuracies in the forecast moisture.

The results of this study suffer from the noisy data of the channel 7 of VAS and from the relatively low spatial and temperature resolution. However, GMS-5 and the future GOES-I/M series of geostationary satellites will have the split window sensor of higher spatial and better temperature resolution. It is believed the wind vector estimation technique using BTD images is most promising for future split window data obtained from geostationary orbit.

I. Performance of a ground based HIS instrument in an operational scenario during the winter STORM-FEST in Feb. and Mar. 1992. Contributed by Robert O. Knuteson.

Objectives

The GB-HIS participated in the STORM-FEST project to assess the research and operational potential of a relatively low-cost passive infrared ground based sensor for continuous vertical profiling of temperature and moisture. The STORM-FEST experiment was the first field test of the real-time implementation of the algorithms for retrieval of temperature and moisture from calibrated infrared down welling radiance spectra. One of the objectives was to field test the hardware and software under pseudo-operational conditions. For this purpose the experiment plan proposed continuous 24 hour operations under all weather conditions. The high degree of success achieved is summarized under the Operations section.

Operations

The GB-HIS operations were conducted at the central boundary layer site just outside Seneca, KS. The GB-HIS instrument resided in a canvas shelter to protect it from wind and rain. The ground support equipment was contained in an adjoining vehicle which also provided office space. The GB-HIS is a vertically viewing instrument, as such it provided vertical profiles at approximately 12 minute intervals. The instrument was operated from about 0:30 UT until 24:00 UT each day. The down periods are due to rain/snow falling into the GB-HIS shelter which caused the on-site operator to cover the instrument and terminate data collection. The following table summarizes the data collected during the STORM-FEST experiment by the GB-HIS. Note that all 44 days from Feb. 1, 1992 to March 15, 1992 are represented.

STORM-FEST DATA SUMMARY

Day #	Date	Calibrated radiance	# Recs. radiance	Time (UT)	Oper	Cond.
1	1 Feb 92	920201f1	115	0055-2347	ROK	Clear
2	2 Feb 92	920202f1	117	0023-2347	ROK	PCldy
3	3 Feb 92	920203f1	112	0113-2348	ROK	Ovcst
4	4 Feb 92	920204f1	3	2337-2357	ROK	Clear
5	5 Feb 92	920205f1	114	0028-2354	ROK	PCldy
6	6 Feb 92	920206f1	113	0027-2346	ROK	PCldy
7	7 Feb 92	920207f1	112	0114-2350	ROK	PCldy
8	8 Feb 92	920208f1	114	0028-2343	ROK	PCldy
9	9 Feb 92	920209f1	103	0021-2054	PVD	Ovcst
10	10 Feb 92	920210f1	116	0017-2332	PVD	Brkn
11	11 Feb 92	920211f1	113	0045-2352	PVD	PCldy
12	12 Feb 92	920212f1	18	0037-0335	PVD	Ovcst
13	13 Feb 92	920213f1	114	0008-2338	PVD	Brkn
14	14 Feb 92	920214f1	27	0029-0506	PVD	Ovcst

15	15 Feb 92	920215f1	52	1436-2347	PVD	Ovcst
16	16 Feb 92	920216f1	112	0035-2336	PVD	PCldy
17	17 Feb 92	920217f1	33	0018-0327 1940-2121	PVD	Ovcst
18	18 Feb 92	920218f1	26	1921-2345	PVD	Ovcst
19	19 Feb 92	920219f1	108	0121-2333	PVD	Ovcst
20	20 Feb 92	920220f1	113	0032-2339	PVD	Clear
21	21 Feb 92	920221f1	109	0030-2247	PVD	PCldy
22	22 Feb 92	920222f1	112	0046-2342	PVD	PCldy
23	23 Feb 92	920223f1	110	0033-1909 2122-2350	AJS	PCldy
24	24 Feb 92	920224f1	98	0053-0517 0653-2343	AJS	Ovcst
25	25 Feb 92	920225f1	112	0026-2334	AJS	PCldy
26	26 Feb 92	920226f1	113	0038-2343	AJS	PCldy
27	27 Feb 92	920227f1	115		AJS	PCldy*
28	28 Feb 92	920228f1	83		AJS	Clear*
29	29 Feb 92	920229f1	111	0102-2350	ROK	Clear
30	1 Mar 92	920301f1	113	0038-2348	ROK	Clear
31	2 Mar 92	920302f1	114	0034-2346	ROK	PCldy
32	3 Mar 92	920303f1	114	0026-2346	ROK	PCldy
33	4 Mar 92	920304f1	33	0017-0559	ROK	Ovcst
34	5 Mar 92	920305f1	27	1915-2359	ROK	Ovcst
35	6 Mar 92	920306f1	59	0033-0135 1450-2357	ROK	PCldy
36	7 Mar 92	920307f1	114	0025-2355	ROK	PCldy
37	8 Mar 92	920308f1	114	0033-2359	ROK	PCldy
38	9 Mar 92	920309f1	47	1524-2345	ROK	Ovcst
39	10 Mar 92	920310f1	114	0015-2355	ROK	PCldy
40	11 Mar 92	920311f1	114	0026-2359	ROK	PCldy
41	12 Mar 92	920312f1	113	0048-2357	ROK	PCldy
42	13 Mar 92	920313f1	114	0030-2358	ROK	PCldy
43	14 Mar 92	920314f1	113	0037-2351	ROK	PCldy
44	15 Mar 92	920315f1	114	0020-2359	ROK	Clear

Results

The GB-HIS was successful in operating in an automated and continuous fashion for the six week duration of the experiment. The real-time calibration of the radiance data worked very reliably throughout this period. During the STORM-FEST experiment the retrieval of temperature and moisture vertical profiles worked very well for cloud-free conditions or conditions with high to mid-level cloud. The real-time retrieval of temperature and moisture was complicated by the presence of low clouds. The presence of low level cloud especially caused problems in retrieval below the cloud base. The retrieval algorithm is currently under revision to improve the performance under low cloud conditions.

The relatively high temporal resolution of the GB-HIS provides a unique perspective for measurement of the development of the planetary boundary layer. An example of a time section of these high resolution data is shown in Fig. 1. Of interest is the development and breakdown of the thermal inversion through the course of the early morning hours to late afternoon; and the influx of moisture between 700 MB and 800 MB at 20 UT. Having an instantaneous vertical profile every 12 minutes allows color images to be made which reveal detailed atmospheric structure, such as the development of the nocturnal temperature inversion or the passage of warm or cold fronts. The GB-HIS operation during STORM-FEST is highly encouraging for the development of an automated infrared ground based vertical sounder as a stand alone instrument or as a complement to other meteorological instrumentation.

List of Figures

Fig. 1. Time section of temperature (top) and mixing ratio (bottom) in degrees K and g/kg respectively for Seneca, KS. on 1 Mar 1992.

GB-HIS TIME SECTIONS FROM SENECA (KS) 01-MAR-92

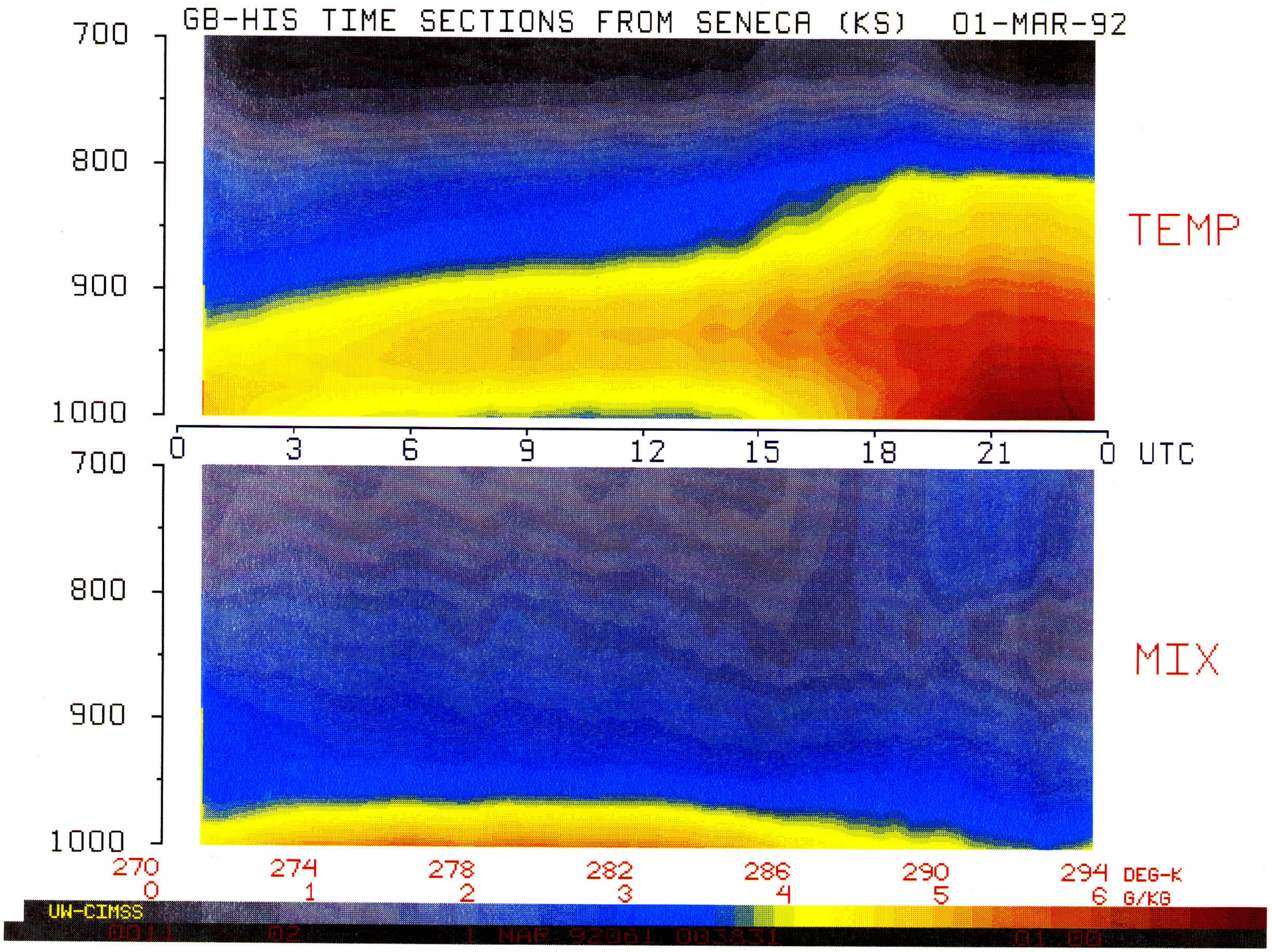

J. A preliminary examination of VAS radiance noise statistics using the high spin budgets for STORM-FEST. Contributed by Timothy J. Schmit.

STORM-FEST provides a unique (and unprecedented) opportunity to investigate the VAS channel noise changes as a function of both number of spins per band as well as time of day. The following discusses both the VAS noise values computed for various spin budgets for one time period, as well as the noise statistics from the high spin budget meso-B dwell sound radiances every three hours for one day. The GOES-7 VAS noise is calculated by noting the variation in the (ideally) uniform space look data. The computation of VAS channel noise values can not only reveal the relative merits of increased spins for various channels, but can also serve as a check of data quality.

Spin Budget

Values were calculated for all channels for dwell sound radiances of three different spin budgets: Nominal, Meso-A and Meso-B. These have total spin budgets of 17, 49 and 165, respectively. The sample size for each set is approximately 450. The data are valid February 20 (92051) between 20 and 22 UT. In Table 1 the spin budgets and detector sizes (large or small--14 or 7 km) are listed for the twelve bands in columns two, three, and four (in this case the initials N, A, and B represent the Nominal, Meso-A and Meso-B type dwell sounds.). Columns five, six, and seven define the average noise as determined by the variance of four lines of "space look" data. All radiance units are mW/(ster-m^2-cm^{-1}).

Table 1. VAS Space look noise data for three spin budgets.

	[-- SPINS-DETECTOR --]			[---------------- RMS NOISE		--------------]	SS
Band	N	A	B	NOMINAL	MESO-A	MESO-B	MESO-B
1	0	5-L	20-L	-	1.65	1.04	4.65
2	1-L	3-L	9-L	2.11	1.24	0.64	1.92
3	2-S	5-S	21-S	1.21	0.86	0.50	2.29
4	2-S	4-S	10-S	0.67	0.57	0.42	1.33
5	2-S	5-S	16-S	0.73	0.52	0.37	1.48
6	2-L	4-L	9-L	0.019	0.015	0.009	0.027
7	2-S	5-S	20-S	0.61	0.49	0.31	1.39
8	1-S	1-S	1-S	0.12	0.10	0.13	-
9	2-L	9-S	31-S	0.31	0.37	0.17	0.95
10	1-L	4-S	14-S	0.08	0.10	0.07	0.26
11	1-L	4-L	13-L	0.04	0.02	0.01	0.036
12	1-L	1-L	1-L	0.007	0.006	0.006	-

The last column (SS) is the single sample noise derived from Meso-B data. This is the average noise (column 7) multiplied by the square root of the number of spins (column 4). This is included for easier comparisons to other methods or design specifications.

Diurnal Variation

Noise statistics were computed every three hours from the meso-B dwell sound radiances. This was done to discern a diurnal component, if any, to the VAS calibration. If the line-by-line calibration is properly working, there should be no diurnal signature. Table 2 shows the noise statistics for VAS channels 1-12. While there is some variability, no discernible trend is seen. Figure 1 shows a chart of channels 1 through 5. Channel 1 is by far the noisiest. Note the oscillation from each time period to the next in channel 3. This is due to the higher spin budget (21 versus 15 spins) at the odd numbered time periods (10 versus 8 minute dwell sound). Figure 2 shows VAS channels 7-10. Channel 7 is still more than twice as noisy as channel 8, even after 7 has been averaged over 15 or 20 spins. The relative higher noise of water vapor channel 9 (compared to 10) is also very apparent. This agrees with visual inspection of the water vapor images. The remaining short-wave channels (6, 11 and 12) also show no diurnal trend (Fig. 3).

Table 2. VAS diurnal noise statistics for February 26 and 27, 1992. All units are: mW/(ster-m^2-cm^{-1}).

Day	Time	Period	Ch-1	Ch-2	Ch-3	Ch-4	Ch-5	Ch-6	Ch-7	Ch-8	Ch-9	Ch-10	Ch-11	Ch-12
92057	14.8	1	1.29	0.66	0.44	0.43	0.35	0.0096	0.30	0.120	0.21	0.070	0.0092	0.0071
92057	17.8	2	1.15	0.71	0.55	0.47	0.35	0.0120	0.29	0.120	0.22	0.075	0.0100	0.0074
92057	20.8	3	0.92	0.66	0.47	0.35	0.33	0.0100	0.26	0.120	0.20	0.069	0.0098	0.0068
92057	23.8	4	1.15	0.74	0.52	0.40	0.43	0.0120	0.30	0.110	0.24	0.079	0.0095	0.0068
92058	2.8	5	1.15	0.64	0.44	0.44	0.33	0.0098	0.28	0.100	0.20	0.063	0.0095	0.0068
92058	5.8	6	1.25	0.75	0.62	0.41	0.41	0.0120	0.33	0.110	0.25	0.082	0.0115	0.0079
92058	8.8	7	1.01	0.64	0.46	0.43	0.36	0.0070	0.26	0.110	0.23	0.062	0.0092	0.0057
92058	11.8	8	1.16	0.74	0.55	0.47	0.41	0.0110	0.33	0.140	0.21	0.071	0.0110	0.0066
92058	14.8	9	1.18	0.70	0.48	0.44	0.32	0.0090	0.28	0.150	0.20	0.075	0.0097	0.0058
92058	17.8	10	1.30	0.69	0.50	0.44	0.39	0.0093	0.27	0.098	0.21	0.072	0.0100	0.0058

Figure 1. Trend of VAS Noise values for channels 1-5.

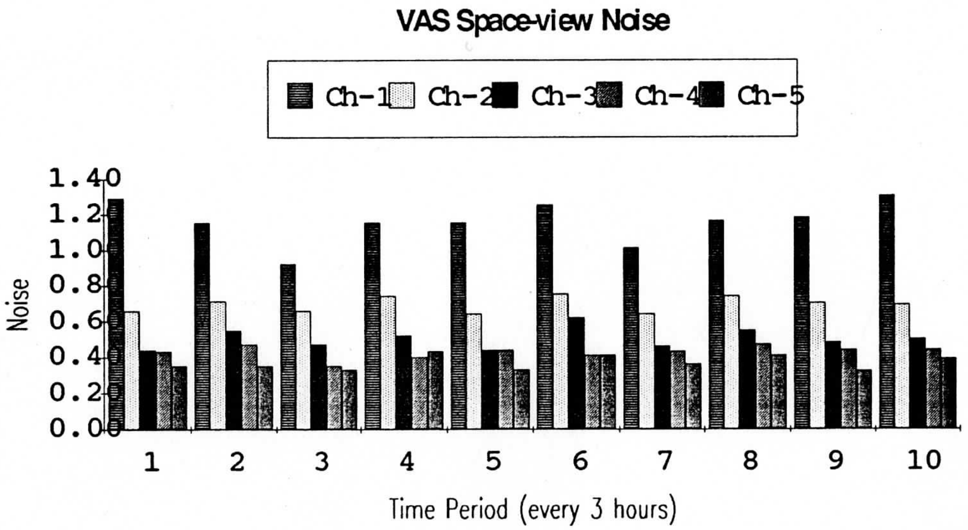

Figure 2. Trend of VAS Noise values for channels 7-10.

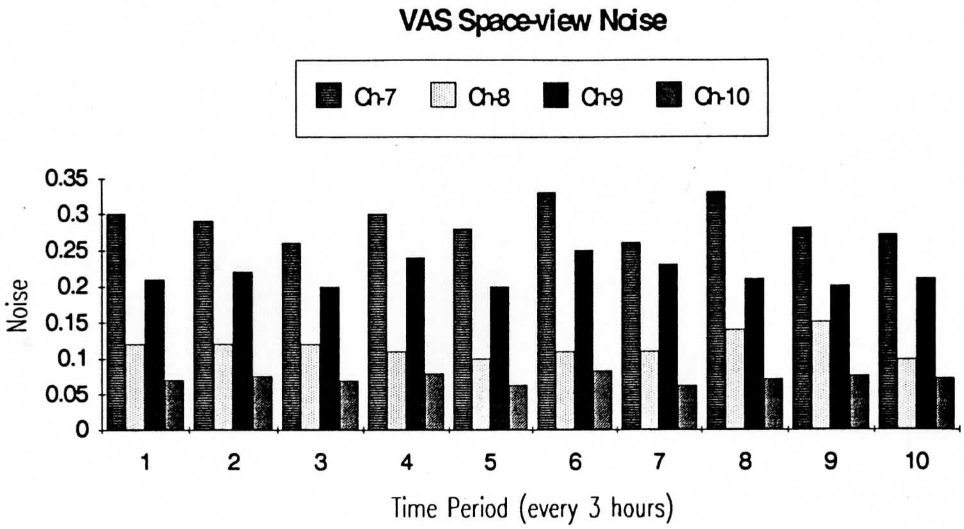

Figure 3. Trend of VAS Noise values for channels 6, 11 and 12.

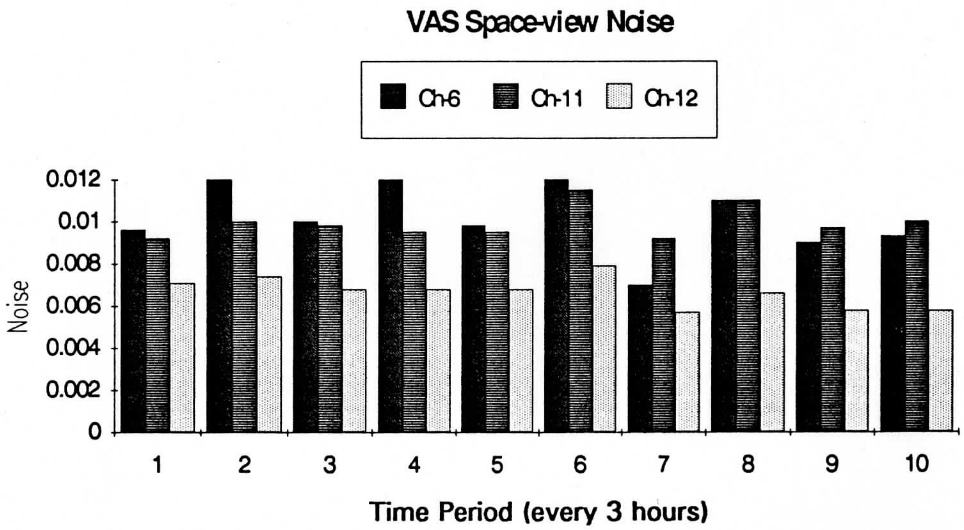

K. Theory of effective resolution of satellite data. Contributed by R. James Purser.

A new theory for the effective resolution of satellite data has been developed in collaboration with Dr. H. L. Huang (CIMSS), and applied to comparisons among the infrared passive sounding systems of HIS, HIRS/2 and GOES.

The theory relies on some notable algebraic properties of the matrices involved in statistical (or physical-statistical) retrievals. Such a retrieval takes the linearized form:

$$\begin{aligned}\vec{A} &= \vec{B} + \mathbf{C}\bullet\mathbf{K}^{T}\bullet\left(\mathbf{K}\bullet\mathbf{C}\bullet\mathbf{K}^{T}+\mathbf{E}\right)^{-1}\bullet\left(\vec{O}-\mathbf{K}\bullet\vec{B}\right)\\ &\equiv \vec{B} + \left(\mathbf{C}^{-1}+\mathbf{K}^{T}\bullet\mathbf{E}^{-1}\bullet\mathbf{K}\right)^{-1}\bullet\mathbf{K}^{T}\bullet\mathbf{E}^{-1}\bullet\left(\vec{O}-\mathbf{K}\bullet\vec{B}\right)\end{aligned} \qquad (1)$$

where vectors, A, B, O, and matrices, **C**, **E**, **K**, are defined as follows:

- A≡ the retrieval or "analysis"
- B≡ the background profile
- O≡ the set of observations (a brightness temperature for each channel)
- **C≡** $<B'B'^T>$, the covariance of background error (assumed unbiased)
- **E≡** $<O'O'^T>$, the covariance of observation error (assumed unbiased)
- **K≡** the generalized interpolation operator between the profile and measurement domains in the case of a retrieval, the nth row of **K** corresponds to the discretized "weighting function" for the nth channel of the instrument.

The same algebraic formalism of (1) applies equally to more general statistical data assimilation, where the technique is referred to as "optimum-interpolation".

The crucial fact on which the new theory is based, is the following: a change δT in the "true" profile T, observational errors and the background remaining constant, causes a change in the retrieval according to the formula:

$$\partial\vec{A} = \mathbf{R}\bullet\partial\vec{T}$$

where

$$\begin{aligned}\mathbf{R} &= \mathbf{C}\bullet\mathbf{K}^{T}\bullet\left(\mathbf{K}\bullet\mathbf{C}\bullet\mathbf{K}^{T}+\mathbf{E}\right)^{-1}\bullet\mathbf{K}\\ &= \left(\mathbf{C}^{-1}+\mathbf{K}^{T}\bullet\mathbf{E}^{-1}\bullet\mathbf{K}\right)^{-1}\bullet\mathbf{K}^{T}\bullet\mathbf{E}^{-1}\mathbf{K}\end{aligned} \qquad (2)$$

is a "resolution matrix" whose diagonal elements R_{ii} sum to a positive dimensionless quantity called the "degrees of freedom for signal" (Wahba, 1985). This may be consistently interpreted as quantifying the effectively independent pieces of information being contributed by the measurements to the retrieval. Since each element R_{ii} corresponds to a particular level of the profile, one may interpret

$$\rho_i = \frac{R_{ii}}{\partial z_i} \tag{3}$$

where δz_i is the layer thickness at level i, as a measure of the "density" of such independent data affecting this level.

In practice, it has been found desirable to smooth ρ_i in a quantity-conserving way in order to obtain a diagnostic which is less erratically distributed in the vertical. (Such smoothing is absolutely necessary in applications of this technique to point in-situ data, otherwise the density distribution obtained is confined to impulsive concentrations only at the data locations themselves.)

The detailed justification for this proposed measure of effective data density has been set out in an article (Purser and Huang, 1992) presently under review for possible publication in the Journal of Applied Meteorology. This study also contains a detailed evaluation of the alternative approaches to estimating effective data density (and hence, resolution) based upon the Backus-Gilbert (1968, 1970) spread functions, which are shown to be seriously misleading in applications to instruments (such as the HIS) that possess inherently high spectral resolution. The article also describes a modification of the scalar density that can be made in the case of retrievals in more than one dimension where the resolving characteristics of the instrument may be very different in different orientations (limb sounders provide an especially pertinent example). In the modified form, we obtain a tensor instead of a scalar, and we are thereby enabled to quantify the different resolution characteristics of the data in all the different orientations. The scalar and tensor densities, marked $\rho^{(a)}$ and $\rho^{(t)}$ respectively, are shown for vertical soundings with the HIRS/2 and HIS instruments in Figures 1a and 1b. In the case of both instruments, these two diagnostics are seen to be reasonably consistent except near the retrieval domain boundaries. The expected superiority of the HIS instrument is strikingly evident in comparing the corresponding magnitudes at each level.

A further generalization of the technique creates a density which, instead of integrating to the degrees of freedom for signal, integrates to the "information" in the entropic sense defined by Shannon (1949). A paper is presently under preparation describing this particular development in the context of comparisons among simulated HIS, HIRS/2 and GOES instruments.

Finally, it is possible to carry out an analogous theory of effective data resolution, both in degrees of freedom for signal, and in entropic information, but now projected into the optical spectrum domain. It is found that the "degrees of freedom" and "entropy" densities are consistent with each other in qualitative terms. Figures 2a and 2b display these computed densities in the three bands of the simulated HIS instrument.

List of Figures

Fig. 1a. Scalar and tensor densities, marked ($\rho^{(a)}$) and ($\rho^{(t)}$) respectively, for vertical soundings with the HIRS/2 instrument.

Fig. 1b. Same as Fig. 1a except for the HIS instrument.

Fig. 2a. Density of the degrees of freedom for the three bands of the HIS instrument. The horizontal axes are wave number (m^{-1}) and the vertical axes are density per unit wave number.

Fig. 2b. Same as Fig. 2a except the vertical axes are defined as entropy densities.

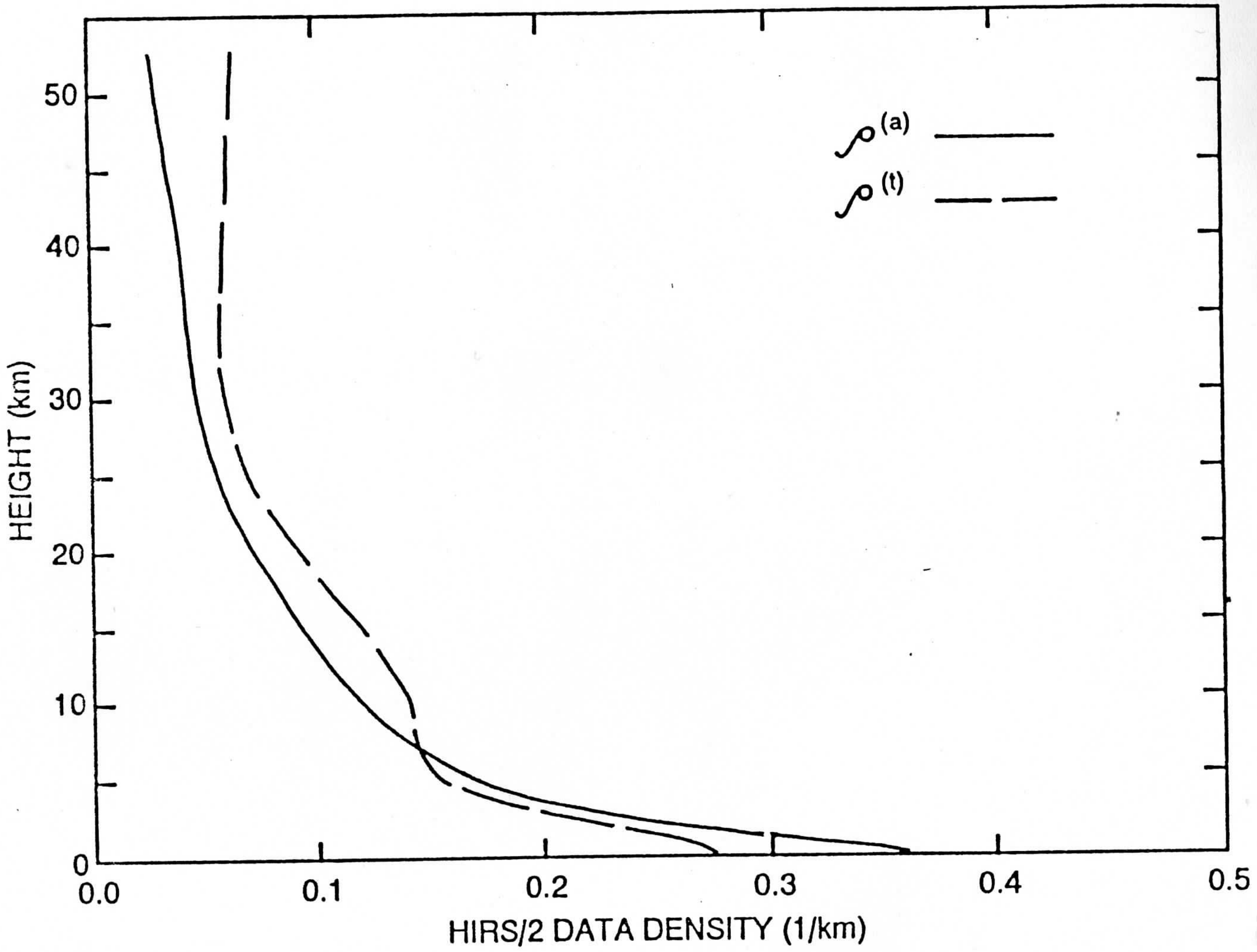

$\rho^{(a)}$
$\rho^{(t)}$
HEIGHT (km)
0
10
20
30
40
50
0.0
0.1
0.2
0.3
0.4
0.5
HIRS/2 DATA DENSITY (1/km)

Figure 1a

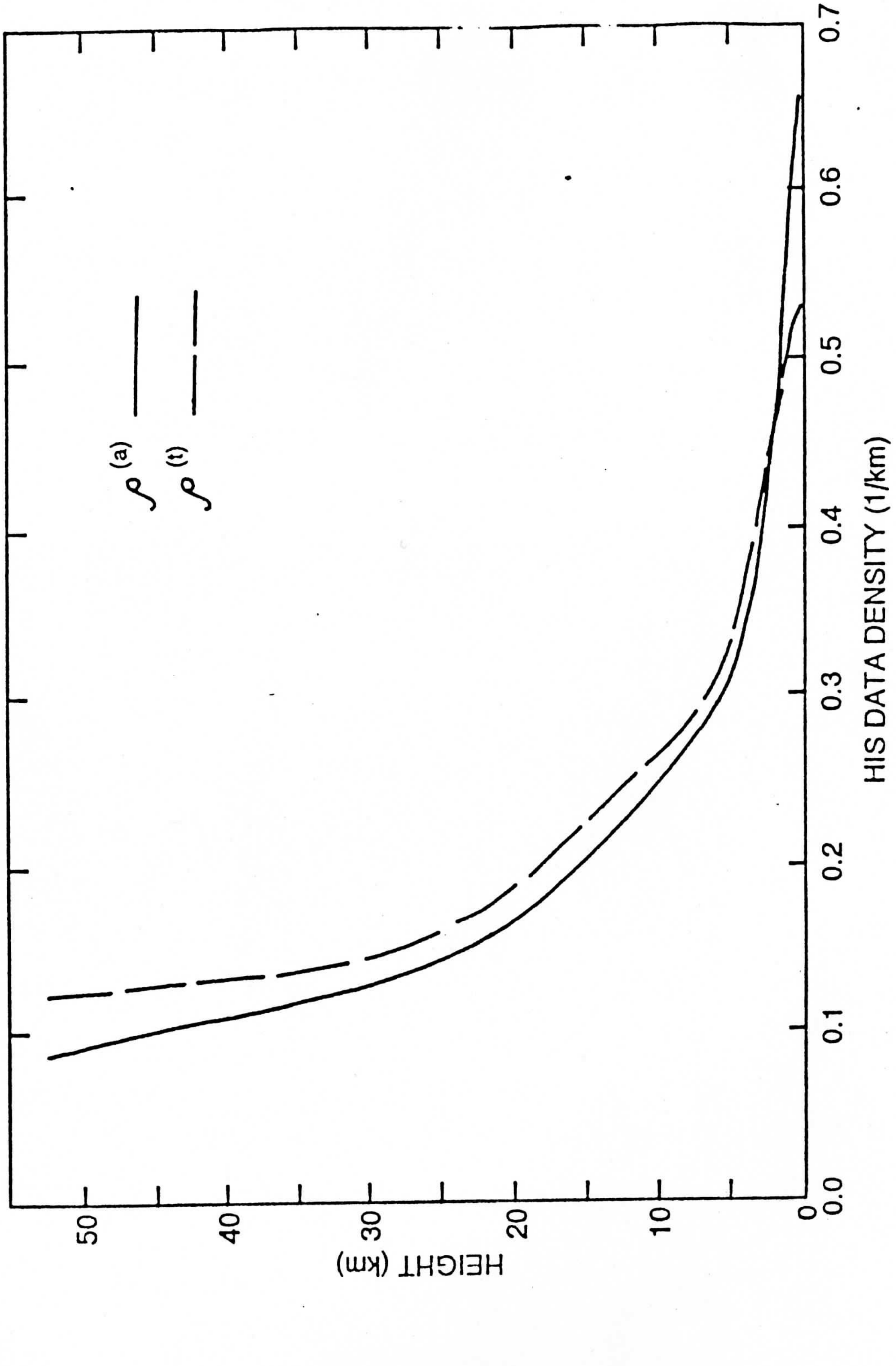
HEIGHT (km)
0
10
20
30
40
50
HIS DATA DENSITY (1/km)
0.0
0.1
0.2
0.3
0.4
0.5
0.6
0.7
$\rho^{(a)}$
$\rho^{(t)}$

Figure 1b

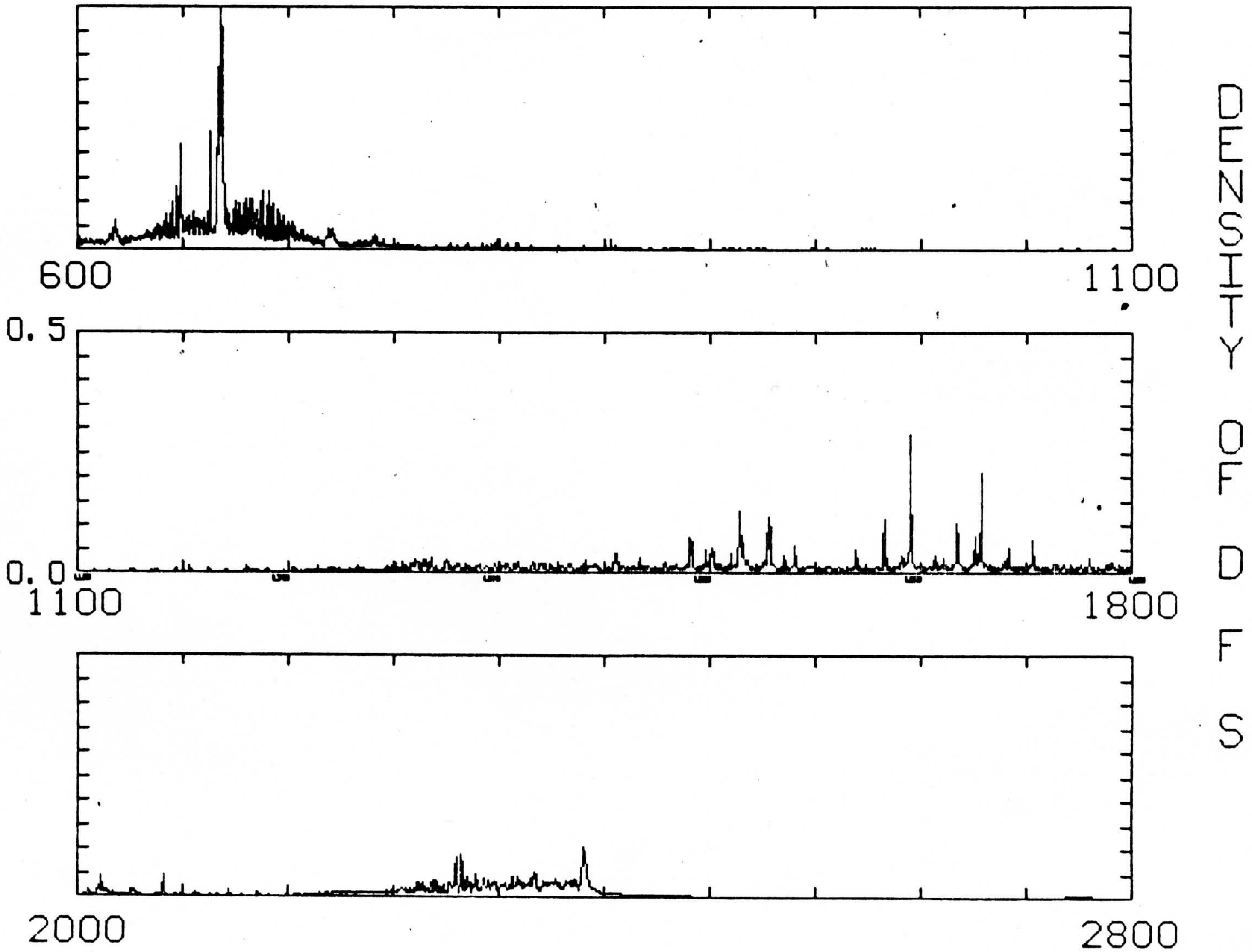

Figure 2b

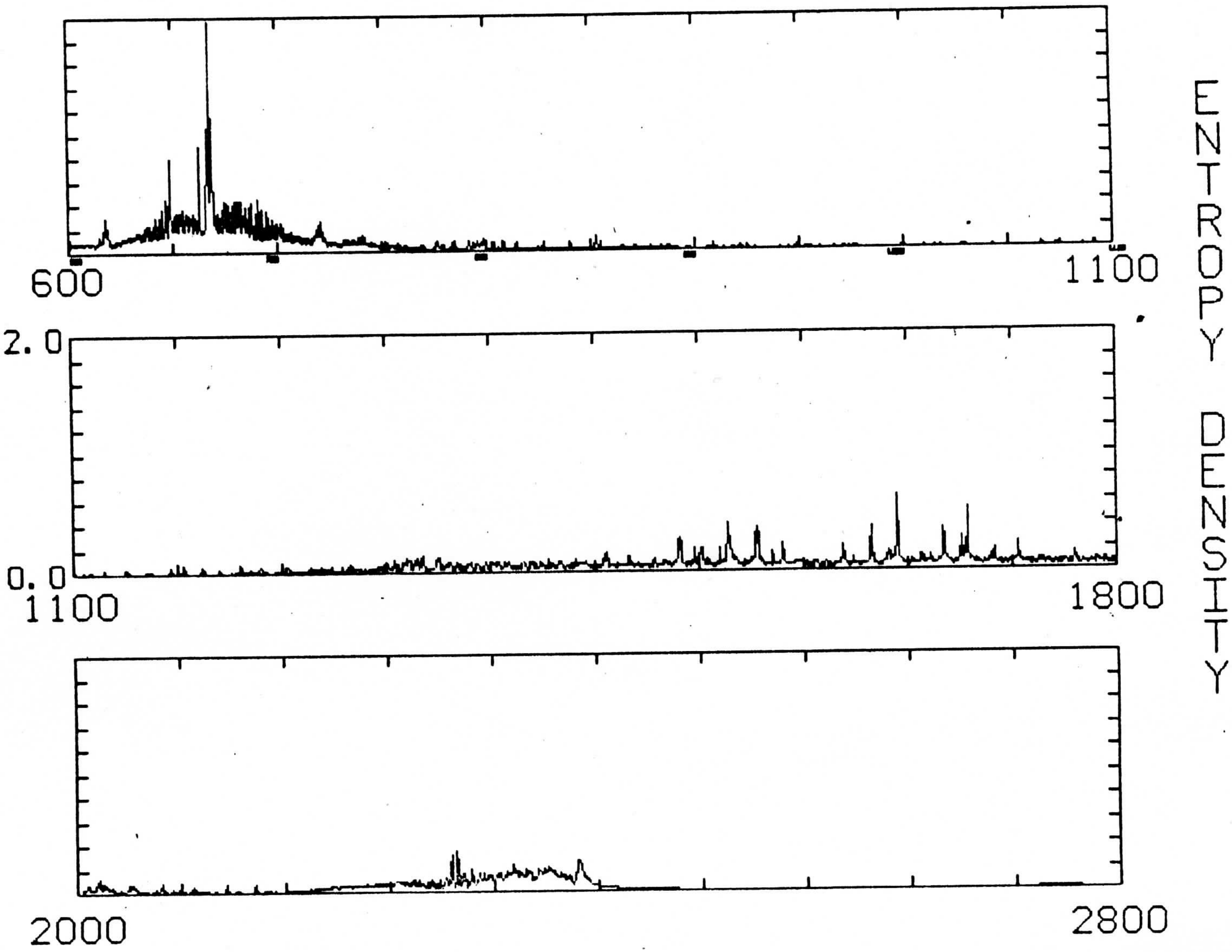

Figure 2b

L. Applications and extension of the recursive filter technique to global scales. Contributed by R. James Purser.

A method of empirical analysis by recursive filtering is currently used routinely in the processing of McIDAS satellite products. The technique originated at the British Meteorological Office (BMO) with the two dimensional scheme of Purser and McQuigg (1982), but has been developed in collaboration with Hayden (CIMSS) (Hayden and Purser, 1986) into a more elaborate three dimensional scheme at CIMSS. About half of a paper that is intended to be the standard reference on the method is being written up. The method is broadly similar to the classical "successive correction" methods of Bergthorssen and Doos (1955) and Cressman (1959), each correction to the analysis being generated by smoothing the current analysis-minus-observation residuals. In the case of our scheme, the corrections are generated by a particularly efficient technique involving the application of recursive numerical smoothers. The scheme incorporates an automatic feedback between the perceived observation density (which is notoriously variable in the case of satellite data) and the spatial scale of the smoother locally. It also has an iterative form of quality control built into it, which replaces the usual "accept/reject" criterion by a continuous weighting on the measurements, updated and refined at successive corrections according to the discrepancy between the observation in question and the interim analysis at this stage.

Following research begun at the BMO, an extension of the method, originally developed for limited area Cartesian grids, is under way to allow operation with a global latitude and longitude grid. Special procedures must be adopted in the vicinity of both coordinate poles and these must then be blended consistently with the regular recursive filters adopted everywhere else. The aim is to effect a reasonably isotropic smoothing at all points. Figure 1 illustrates results of applying the basic "spherical recursive filters" successively to an initial distribution consisting of two point-concentrations located near the boundaries of the two polar regions treated by the special procedures. The map projection is a transverse Mercator which introduces minimal distortion along its central meridian. We see that, provided at least two or three applications of the filter are made to generate each smoothed output, a reasonably isotropic and smooth dispersion is produced, suggesting that a successful generalization of the method to the sphere can be expected.

List of Figures

Fig. 1. An illustration of applying spherical recursive filters successively to an initial distribution consisting of two point concentrations near the boundaries of the two polar regions.

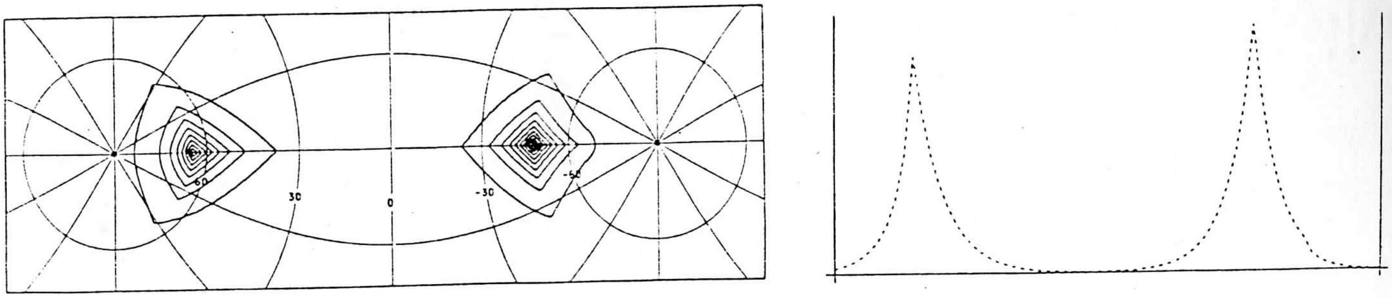

A FOURIER RECURSIVE FILTER APPLIED TO A SPHERICAL GRID
WITH 1 COMPLETE PASSES OF THE FILTER
FILTERING APPLIED TO ONE OR MORE DELTA FUNCTIONS

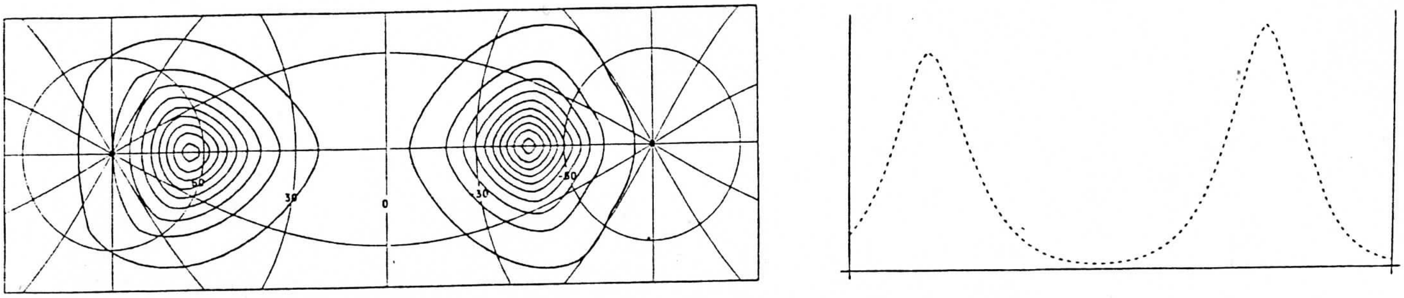

A FOURIER RECURSIVE FILTER APPLIED TO A SPHERICAL GRID
WITH 2 COMPLETE PASSES OF THE FILTER
FILTERING APPLIED TO ONE OR MORE DELTA FUNCTIONS

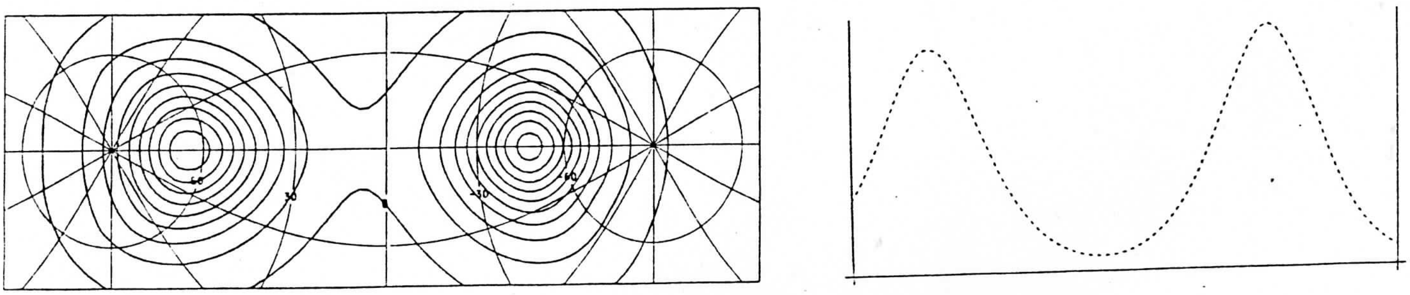

A FOURIER RECURSIVE FILTER APPLIED TO A SPHERICAL GRID
WITH 3 COMPLETE PASSES OF THE FILTER
FILTERING APPLIED TO ONE OR MORE DELTA FUNCTIONS

Figure 1

III. PERSONNEL AND EQUIPMENT

Personnel

	LABOR (%)	COMPUTER (%)
SSEC		
Anthony J. Schreiner	20	35
Christopher S. Velden	30	40
Robert T. Merrill	20	20
Timothy J. Schmit	10	5
Barry T. Rowe	10	10
R. James Purser	35	5
Steven J. Nieman	35	50
Robert O. Knuteson	10	0
Kathy I. Strabala	10	10
Xiaohua Wu	100	100
NESDIS		
Christopher M. Hayden		20
Gary S. Wade		60
Robert M. Aune		80
Leroy D. Herman		80
Geary M. Callan		50
Robert M. Rabin		30
Visiting Scientist		
Toshiro Inoue	0	50

The numbers underneath the column "LABOR" represents the percentage of their labor time which was charged to this project. The percentages below the column headed by "COMPUTER" indicate the amount of computer time which the scientists charged to this contract. Both percentages are based on one year being equivalent to 100%. NESDIS employees' labor is provided from funds outside of this contract.

Equipment

1-Satellite Modem:

1-IBM 3480 controller:

1-IBM 3480 tape unit:

2-Team black & white hard copy video device units:

1-IBM RISC 6000 computer system:

Of the above items the first four were acquired as money set aside for the continued development and expansion of the McIDAS system as a prototype for VDUC improvements and the development of operational NESDIS processing systems. The IBM RISC 6000 was acquired to support the four dimensional data assimilation development.

IV. SUMMARY

The support from this contract has been important in providing the programmers, research scientists, and support staff the opportunity to perform a wide variety of research within the CIMSS organization. Many of the areas of research which were discussed in Section III are ongoing topics.

Additionally, this contract has also substantially assisted in the upgrading of the McIDAS facility. As computer networking continues in the future, the improvements resulting from specially directed money derived from this contract will remain important.

V. REFERENCES

Aune, R. M., L. W. Uccellini, R. A. Petersen, and J. J. Tuccillo, 1987: A VAS numerical model impact study using the Gal-Chen variational approach. *Mon. Wea. Rev.*, 115, pp. 1009-1035.

Backus, G., and F. Gilbert, 1970: Uniqueness in the inversion of inaccurate gross earth data. Phil. Trans. Roy. Soc. London., A266, 123-192.

Backus, G., and F. Gilbert, 1968: The resolving power of gross earth data. *Gephys. J. Roy. Astro. Soc.*, **16**, 169-205.

Bergthorssen, P., and B. Doos, 1955: Numerical weather map analysis. *Tellus*, **7**, 329-340.

Bourke, W. and J. McGregor, 1983: A nonlinear vertical mode initialization scheme for a limited area prediction model. *Mon. Wea. Rev.*, 111, pp. 2285-2287

Carlson, T. N. and F. H. Ludlum, 1968: Conditions for the occurrence of severe local storms. *Tellus*, **20**, 203-226.

Cram, J. M. and M. L. Kaplan, 1985: Variational assimilation of VAS data into a mesoscale model: Assimilation method and sensitivity experiments. *Mon. Wea. Rev.*, 113, pp. 467-484.

Cressman, G.P., 1959: An operational analysis scheme. *Mon. Wea. Rev.*, **87**, 367-374.

Gal-Chen, T., 1983: Initialization of mesoscale models: The possible impact of remotely sensed data. *Mesoscale Meteorology: Theories, Observations and Models*, D. K. Lilly and T. Gal-Chen, Eds., Reidel, pp. 157-171.

Gal-Chen, T., B. D. Schmidt, and L. W. Uccellini, 1986: Simulation experiments for testing the assimilation of geostationary satellite temperature retrievals into a numerical prediction model. *Mon. Wea. Rev.*, 114, pp. 1213-1230.

Hayden, C. M., W. L. Smith, and H. M. Woolf, 1981: Determination of moisture from NOAA polar orbiting satellite sounding radiances. *J. Appl. Meteor.*, **20**, 450-466.

Hayden, C. M. and R. J. Purser, 1986: Application of a recursive filter objective analysis in the processing of VAS data. (Preprint) A.M.S. Second conference on satellite meteorology/remote sensing and applications, Williamsburg, Virginia.

Hayden, C. M., 1988: GOES-VAS simultaneous temperature-moisture retrieval algorithm. *J. Appl. Meteor.*, **27**, 705-733.

Hayden, C. M., and R. J. Purser, 1988: Three-dimensional recursive filter objective analysis of meteorological fields. *Preprint Volume Eighth Conference on Numerical Weather Prediction*, Baltimore, MD, February 22-26, 185-190.

Hayden, C. M. and R. T. Merrill, 1988: Recent NESDIS research in wind estimation from geostationary satellite images. Proceedings of the ECMWF Workshop on Data Assimilation and the Use of Satellite Data, Reading, UK, September 5-9, 273-293.

Hayden, C. M. and A. J. Schreiner, 1989: Moisture retrievals from GOES VAS. *Preprints, 4th Conf on Sat Meteor and Oceano, San Diego*, AMS

Hayden, C. M., and C. S. Velden, 1991: Quality control and assimilation experiments with satellite derived wind estimates. *Preprints, Ninth Conference on Numerical Weather Prediction*, Denver, CO, October 14-18, AMS, 19-23.

Herman, L. D., 1989: Validation of cloud motion vectors from AVHRR images. *Twelfth Conference on Weather Analysis and Forecasting,* AMS, October 2-6, Monterey, CA.

Herman, L. D., 1991: Semi-Automated Measurement of Cloud Motions at High Latitudes from Polar Orbiting Satellites. *Seventh Symposium on Meteorological Observations and Instrumentation*, AMS, January 14-18, New Orleans, LA.

Hibbard, W., and D. Santek, 1990: The VIS-5D for easy interactive visualization. *Visualization '90*, San Francisco, IEEE, pp. 28-35.

Hubert, L. F., and L. F. Whitney, Jr., 1971: Wind estimation from geostationary-satellite pictures.

Inoue, T., 1987: A cloud type classification with NOAA-7 split window measurements. *H, Geophys. Res.*, **92**, 3991-4000.

Inoue, T., 1989: Features of clouds over the tropical Pacific during northern hemispheric winter derived from split window measurements. *J. Meteor. Soc. Japan*, **67**, 621-637.

Leese, J. A., C. S. Novak, and B. B. Clark, 1971: An automated technique for obtaining cloud motion from geosynchronous satellite data using cross correlation. *Jour Appl. Meteor*, **10**, 118-132.

Leslie, L. M., G. A. Mills, L. W. Logan, D. J. Gauntlett, G. A. Kelly, M. J. Manton, J. L. McGregor and J. M. Sardie, 1985: A high-resolution primitive equations model for operations and research. *Aust. Meteor. Mag*., 33, pp. 11-35.

Leslie, L. M., and Purser, R. J., 1992: A comparative study of the performance of various vertical discretization schemes. *Meteor. Atmos. Phys.* (submitted).

Lewis, J. M. and T. H. Grayson, 1972: The adjustment of surface wind and pressure by Sasaki's variational matching method. *J. Appl. Meteor*., 11, pp. 586-597.

Lewis, J. M. and C. Crisp, 1989: Climatology of return flow in the Gulf of Mexico. *Preprints, 12th Conf. on Weather Analysis and Forecasting, 2-6 October, Monterey, CA*, 490-493.

Lewis, J. M., C. M. Hayden, R. T Merrill and J. M. Schneider, 1989: GUFMEX: A study of return flow in the Gulf of Mexico. *Bull. Amer. Met. Soc*., 68, 24-29.

Menzel, W. P., W. L. Smith, and T. R. Stewart, 1983: Improved cloud motion wind vector and altitude assignment using VAS. *J. Climate Appl. Meteor.*, **22**, 377-384.

Merrill, R. T., 1989: Advances in automated production of wind estimates from geostationary satellite imagery. *Fourth Conference on Satellite Meteorology and Oceanography,* AMS, May 15-19, San Diego, CA.

Merrill, R. T., W P. Menzel, W. Baker, J. Lynch, and E. Legg, 1991. A report on the recent demonstration of N)AA's upgraded capability to derive cloud motion satellite winds. *Bull. Amer. Meteor. Soc.*, **72,** 372-376.

Merrill, R. T. 1992: Synoptic analysis of the GUFMEX return flow event of 10-12 March 1988. *J. Appl. Meteor.*, 31, (August).

Mostek, A., L. W. Uccellini, R. A. Petersen, and D. Chesters, 1986: Assessment of VAS soundings in the analysis of a preconvective environment. Mon. Wea. Rev., 114, pp. 62-87.

O'lenic, E. A., 1986: The effect of VISSR Atmospheric Sounder (VAS) data on some LFM analyses and forecasts. *Mon. Wea. Rev.*, **114**, 1832-1846.

Purser, R. J., and R. McQuigg, 1982: A successive correction analysis scheme using recursive numerical filters. British Meteorological Office, MettOt11 Technical Note No 154.

Purser, R. J., and Leslie, L. M., 1991: A comparative study of the performance of various vertical discretization schemes, (Preprint) A.M.S. Ninth Conference on Numerical Weather Prediction. Denver, Colorado.

Purser, R. J., 1992: Contact transformations and Hamiltonian dynamics in generalized semi-geostrophic theories *J. Atmos. Sci.* (to appear).

Purser, R. J., and Huang, H.-L., 1992: Estimating effective data density in a satellite retrieval or an objective analysis. *J. Appl. Meteor.* (submitted)

Schmetz, J. and M. Nuret, 1987: Automatic tracking of high-level clouds in METEOSAT infrared images with a radiance windowing technique. *ESA Journal*, **11**, 275-286

Schreiner, A. J., C. M. Hayden, and C. A. Paris, 1992: A study of satellite-derived moisture with emphasis on the Gulf of Mexico. *J. Appl. Meteor.,* Accepted for publishing.

Seaman, R. S., R. L. Falconer, and J. Brown, 1977: Application of a variational blending technique to numerical analysis in the Australian region. Aust. Meteor. Mag., 25, pp. 3-23.

Shannon, C., 1949: A mathematical theory of communications. Proc. I.C.E., 37, 10-21.

Shenk, Wm. E., and Earl R. Kreins, 1969; A comparison between observed wind and cloud motions derived from NIMBUS II HRIR measurements. NASA TM X-622-69-285, July, 1-43.

Smith, E., and D. Phillips, 1972: Measurements from Satellite Platforms, Annual Satellite Report No. NAS5-11542, 1971-72, SSEC, University of Wisconsin, 1-53.

Smith, W. L., H. M. Woolf, and A. J. Schreiner, 1985: Simultaneous retrieval of surface atmospheric parameters: A physical and analytically direct approach. *Advances in Remote Sensing*, Deepak, 221-232.

Stewart, T. R., C. M. Hayden, and W. L. Smith, 1985: A note on water-vapor wind tracking using VAS data on McIDAS. *Bull. Amer. Meteor. Soc.*, **66,** 1111-1115.

Turner, J., and D. E. Warren, 1989: Cloud track winds in the polar regions from sequences of AVHRR images. *Int. J. Remote Sensing*, **10**, 695-703.

Wahba, G., 1985: Design criteria and eigensequence plots for satellite-computed tomography. *J. Atmos. Ocean Tech.*, **2**, 125-132.

Weiss, S. J., 1990: The impact of low-level moisture and air mass stability on severe storm forecasting during return flow episodes. *Sixteenth Conf. Severe Local Storms*, Kananaskis Park, Alberta, 90-95.